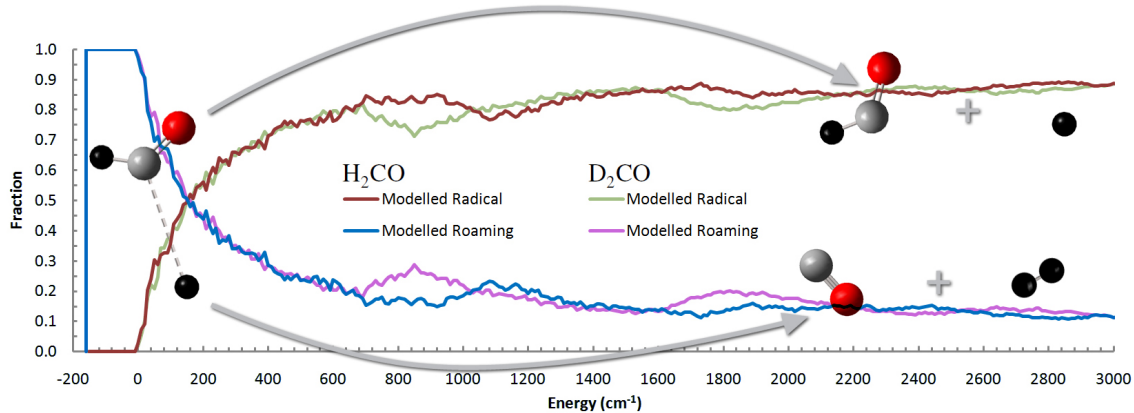


# Non-Transition State Dynamics And Multiple Mechanism Reactions In The Photodissociation Of Small Aldehydes

DUNCAN ANDREWS

SID: 305203517



Supervisor: Dr Meredith Jordan

This thesis is submitted in partial fulfillment of  
the requirements for the degree of  
Bachelor of Science (Honours)

School of Chemistry  
The University of Sydney  
Australia

7 November 2010

## **Abstract**

There are three general classes of unimolecular dissociation reactions: the first class requires surmounting an energy barrier, via a “tight” transition state (TS), producing molecular products; the second class, radical dissociation, are barrierless; the third class, termed “roaming”, starts as frustrated radical dissociation, however intermolecular abstraction produces molecular products. The tight TS and radical dissociation mechanisms are well known and are modelled well by variations of Transition State Theory (TST). However roaming is a novel mechanism that cannot be modelled using TST. A simple statistical model, based on Phase Space Theory, is developed for roaming reactions and the roaming flux in H<sub>2</sub>CO and CH<sub>3</sub>CHO is predicted (see figure). For CH<sub>3</sub>CHO there are multiple dissociation and isotope exchange pathways available at photochemical energies. These are investigated using deuterated isotopologues.

## **Acknowledgements and Statement of Contribution of the Student**

Firstly, I would like to thank my supervisors, Dr Meredith Jordan and ,Professor Scott Kable without whose presence I would have . . . including proof reading thesis

Brianna R. Heazlewood for allowing me to work with her on the the experiments described within and for showing me many lab techniques and answering my many questions.

Dr Alan T. Maccarone including proof reading thesis and Dr Klaas Nauta for showing me many lab techniques and answering my many questions.

Dr Richard Payne and Mr Trent Conroy for synthesizing CH<sub>3</sub>CDO sample. Dr Ian Luck for running high resolution NMR scans of our CH<sub>3</sub>CDO sample.

Dr Stephen J. Klippenstein for providing accurate radical dissociation rates...

Marcel Kaegi and Jack Zylmans from the Chemistry workshop for fixing our leaking backing pump and also unjamming our sample tube.

Roaming Experimental Bounds (upper bound) (lower bound)

## CONTENTS

<b>Abstract</b>	<b>ii</b>
<b>Acknowledgements and Statement of Contribution of the Student</b>	<b>iii</b>
<b>List of Symbols</b>	<b>vii</b>
<b>List of Acronyms</b>	<b>xiii</b>
<b>List of Figures</b>	<b>xvii</b>
<b>List of Tables</b>	<b>xxiii</b>
<b>Chapter 1 Introduction</b>	<b>1</b>
1.1 Transition State Theory .....	1
1.2 Non-TST Reaction Mechanisms .....	2
1.3 Photodissociation Channels Of Small Aldehydes .....	3
1.4 Relevance Of Roaming In Small Aldehydes .....	6
1.5 Other Roaming Models .....	7
Quasiclassical Trajectory Calculations .....	7
Reduced Dimensional Trajectory Calculations .....	8
Statistical Treatments .....	8
1.6 Theoretical Aims .....	9
1.7 Experimental Aims .....	10
<b>Chapter 2 Phase Space Theory Roaming Model</b>	<b>11</b>
2.1 Overview .....	11
2.2 Phase Space Theory .....	13
2.3 Computer Code .....	14
2.4 Experimental Roaming Data .....	18

2.5	Formaldehyde Results .....	20
2.6	Predicting $\Delta E_{roam}$ .....	23
2.7	Acetaldehyde Results.....	25
2.8	The Roaming Probability Parameter $P_{roam}$ .....	27
2.9	Predictive Results For formaldehyde- $d_2$ .....	30
2.10	General Trends Observed.....	32
2.11	PST Model Summary .....	33
<b>Chapter 3 H/D Exchange Experiments</b>		<b>34</b>
3.1	Overview .....	34
3.2	Laser Induced Fluorescence Experiments.....	35
	The Vacuum Chamber.....	36
	Photolysis and Probe Laser Systems .....	36
	Fluorescence Detection.....	38
	Sample Preparation .....	38
3.3	Spectroscopic Techniques.....	39
	Laser Induced Fluorescence Excitation (LIF) Spectroscopy .....	39
	Photo-Fragment Excitation (PHOFEX) Spectroscopy.....	39
3.4	LIF Results.....	41
3.5	PHOFEX Results .....	43
3.6	Analysis And Modelling.....	45
	Rate Calculations .....	45
	Master Equation Analysis .....	51
	Comparing Experimental And Modelled Results .....	53
<b>Chapter 4 Conclusions And Future Work</b>		<b>54</b>
4.1	Conclusions .....	54
4.2	Future Work.....	56
<b>References</b>		<b>57</b>
<b>Appendix A Additional Comments</b>		<b>64</b>

<b>Appendix B Data Tables</b>	<b>65</b>
B.1 PST Roaming Model Input Data .....	65
B.2 Experimental Model Input Data .....	70
<b>Appendix C Additional Figures And Previously Recorded Spectra</b>	<b>78</b>
<b>Appendix D PST State Count Algorithm Description and Pseudocode</b>	<b>84</b>
D.1 Accommodating Generic Cases .....	84
<b>Appendix E Variational Transition State Theory Implementation</b>	<b>85</b>
E.1 Addressing Problems With The Original UNIMOL GEOM Program .....	85
<b>Appendix F Additional Considerations For Modelling Pyrolysis Experiments</b>	<b>89</b>
F.1 Morse Curve And $\Delta E_{roam}$ .....	89
F.2 Centrifugal Barriers .....	91
F.3 Collisions And Pressure Dependence .....	93
F.4 Rotational Switching .....	93
<b>Appendix G Experimental Evidence For Roaming</b>	<b>95</b>
G.1 Evidence for roaming in photolysis experiments .....	95
G.2 Evidence for roaming in pyrolysis experiments .....	100
<b>Appendix H Quasiclassical Trajectory Calculations Of The Bowman Group</b>	<b>102</b>

## List of Symbols

<b>Notation</b>	<b>Description</b>	<b>Page List</b>
$\vec{A}$	The most unequal principal rotational constant of an object approximated as a symmetric top	16, 17, 26, 81
$\vec{b}$	The fragment separation (the impact parameter)	14
$\vec{B}$	The arithmetic mean of the two similar rotational constants of an object approximated as a symmetric top	16, 17, 81
$\beta$	The Morse parameter, defines the curved shape of a Morse curve	83, 84
$C_6$	The spherically averaged sum of dipole-induced-dipole and dispersion contributions to $V_{eff}$	85
$d^{tot}$	The total degeneracy of a pair of quantum states	15
$\rho_R$	The density of states of the reactant	1, 46
$D_0$	The reactant dissociation energy	xvii, 11–13, 83, 84
$E_A$	The available energy	11–15, 27, 86
$E_{critical}$	The minimum energy required for reaction via the tight TS channel (1)	1, 46
$E_{excess}$	The excess energy that is distributed statistically in an impulsive unimolecular dissociation	xxii, 89
$E_{orb}$	The energy due to orbital angular momentum ( $\vec{L}$ )	x, 17, 85

<b>Notation</b>	<b>Description</b>	<b>Page List</b>
$E_{RC}$	Excess energy in the reaction coordinate	11
$E_{rem}$	The remaining available energy after the energy associated with the quantum numbers assigned in parent loops has been assigned	16, 17
$E(\vec{J}, K)$	Rotational energy	16
$E_{rvmax}$	The maximum allowable rovibrational energy for states that form radical products	xvii, 11, 12
$E_{tot}$	The total energy, excitation energy	xvii, xviii, 1, 2, 11, 12, 14, 18, 20–22, 25, 29, 30, 46, 85
$E_t$	The relative translational energy of product fragments	xvii, xxi, xxii, 11–13, 16, 17, 84–86, 89
$E_{tmin}$	The minimum translational energy required for a state to have escaped the attractive potential	xvii, xxi, 12, 27, 85, 86
$E'_{tmin}$	The minimum translational energy required for a state to have escaped the attractive potential at the arbitrary fragment separation $r'$	xvii, 12
$\Delta E_{roam}$	The energy difference between the radical threshold and the roaming threshold	xvii, xviii, xxiii, 12, 13, 15, 18–27, 29–33, 54, 56, 83, 84
$\Delta E_{TS}$	The reaction exoergicity released in an impulsive reaction	89, 90
$f_{rad}$	The radical product fraction	15, 18
$f_{roam}$	The roaming product fraction	vii, 15, 18, 19

<b>Notation</b>	<b>Description</b>	<b>Page List</b>
$f_{RR}$	The branching fraction between molecular products produced via the roaming channel (3) and radical products produced via the radical channel (2). This is the same as $f_{roam}$ .	19, 20
$f_{RTS}$	The branching fraction for molecular products produced via the roaming channel (3) and the tight TS channel (1)	18–20, 30
$I_{TS}$	Impulse	89
$\vec{J}$	The total angular momentum	2, 7, 16, 48, 49, 98
$\vec{J}_1$	The total angular momentum of the first fragment	xvii, 14, 15
$\vec{J}_2$	The total angular momentum of the second fragment	xvii, 14, 15
$\vec{J}_i$	The total angular momentum of fragment i	16, 17
$\vec{J}_{parent}$	The total reactant angular momentum	xvii, 13–15, 84
$\vec{J}_{CO}$	The total angular momentum of CO fragments	89–92, 94, 96
$K$	The angular momentum about the principal moment of inertia, for a symmetric top	15, 16
$K_1$	The angular momentum about the principal moment of inertia, for fragment 1	15
$K_2$	The angular momentum about the principal moment of inertia, for fragment 2	15
$k_B$	The Boltzmann constant	1
$K_i$	The angular momentum about the principal moment of inertia, for fragment i	16
$k_{rad}$	The rate coefficient for the radical channel (2)	19, 20, 28, 29, 47
$k_{roam}$	The rate coefficient for the roaming channel (3)	28, 29

<b>Notation</b>	<b>Description</b>	<b>Page List</b>
$k_{TS}$	The rate coefficient for the tight TS channel (1)	1, 19, 20, 28, 29, 46
$\vec{L}$	Orbital angular momentum, the angular momentum due to the fragments orbiting each other	vii, xvii, xxi, 14, 15, 17, 84– 86
$\vec{L}_{max}$	The maximum orbital angular momentum value that satisfies conservation of energy and angular momentum	15, 85, 86
$\mu$	The reduced mass of the fragments	14, 17, 85
$\mu_{RC}$	The reduced mass of the reaction coordinate	83
$\mu_{TS}$	The effective mass of the tight transition state	89, 90
$\omega_{RC}$	The reaction coordinate harmonic frequency	83
$P_{roam}$	The probability that frustrated states will roam, rather than re-forming reactants and forming radicals	xviii, 27–31, 33, 54, 56
$Q_R$	The partition function of the reactant	1
$Q_{TS}$	The partition function of the transition state	1
$r$	The distance between fragments	xvii, 11–14, 17, 24, 83, 85
$r_e$	The equilibrium reaction coordinate bond length	83, 84
$r'$	An arbitrary fragment separation used as an example in figures 2.1 and 2.2	vii, xvii, 12
$r_{roam}$	The minimum separation at which roaming may occur	xvii, xxi, 11, 12, 17, 23, 83– 86

<b>Notation</b>	<b>Description</b>	<b>Page List</b>
$r^*$	The fragment separation where $V_{eff}$ is maximum	xxi, 85, 86
$S_0$	The electronic ground state singlet surface	3, 18, 39, 43, 79, 92
$S_1$	The first singlet excited state	3, 39
$sp^2$	Hybrid orbitals resulting from mixing one s and two p atomic orbitals	92
$\omega_{rad}$	The sum of states forming radical products	xviii, 14, 15, 19, 21, 22, 29, 31
$\omega_{roam}$	The sum of states that are frustrated and may roam	xviii, 14, 15, 19, 21, 22, 29, 31
$\omega_{TS}$	The sum of states of the tight transition state	1, 19, 46
$\omega_{tot}$	The total sum of states	14, 15
$T$	Temperature	1
$T_1$	The lowest triplet state	39–41, 43, 53, 55
$h$	The Planck constant	1, 46, 85
$V$	The potential energy	xvii, 11–14, 83, 85
$\vec{v}$	The relative velocity of the fragments	14
$V_{eff}$	The effective potential energy, including $E_{orb}$	vii, ix, xxi, 85, 86
$v_{H_2}$	The vibrational level of $H_2$ fragments	91, 96
$v_1$	The vibrational quantum numbers for all possible vibrations of fragment 1	15

<b>Notation</b>	<b>Description</b>	<b>Page List</b>
$v_2$	The vibrational quantum numbers for all possible vibrations of fragment 2	15
$v_i$	The vibrational quantum numbers for all possible vibrations of fragment i	16

## List of Acronyms

<b>Notation</b>	<b>Description</b>	<b>Page List</b>
6-311+G(d,p)	A Pople triple zeta basis set with polarisation and diffuse functions	45
ARAS	Atomic Resonance Absorption Spectroscopy	4
aug-cc-pVDZ	Augmented with added diffuse functions, correlation-consistent, polarized, valence-only, Double-zeta	6
aug-cc-pVTZ	Augmented with added diffuse functions, correlation-consistent, polarized, valence-only, Triple-zeta	97
BBO	$\beta$ -BaB <sub>2</sub> O <sub>4</sub>	36
C++	An object-oriented extension to the <i>C</i> programming language, defined by Bjarne Stroustrup in 1985 [1]	47, 51, 64, 79
CASPT2	Complete Active Space Multi-Reference Second-Order Perturbation Theory	6
cc-pVDZ	correlation-consistent, polarized, valence-only, Double-zeta	97
cc-pVTZ	correlation-consistent, polarized, valence-only, Triple-zeta	97
CCSD(T)	Coupled-Cluster with Single, Double and Perturbative Triple Excitations	64, 97
DCM	[2-[2-[4-(dimethylamino)phenyl]ethenyl]-6-methyl-4H-pyran-4-ylidene]-propanedinitrile	36

<b>Notation</b>	<b>Description</b>	<b>Page List</b>
FTIR	Fourier Transform Infrared	93
HK	Houston and Kable	92, 96
JAMA/C++	A translation of the Java Matrix Library, developed by the Mathworks and NIST, into C++ [2]	64
KDP	Potassium Dihydrogen Phosphate	36
LIF	Laser Induced Fluorescence	4, 10, 35, 39–41, 43, 44, 55, 79, 89, 91, 92
LJ	Lennard Jones	23–25, 33
MEP	Minimum Energy Path	2, 4, 6, 52, 53
MP2	Second order Møller-Plesset perturbation theory	45
MR-CI	Multireference Configuration Interaction	97
Nd:YAG	Neodymium Doped Yttrium Aluminum Garnet	36
NMR	Nuclear Magnetic Resonance	38, 41
PES	Potential Energy Surface	xvii, xix, 2, 6–9, 12, 17, 23, 27, 33, 45, 49, 50, 83, 84, 86, 89, 96–98
PHOFEX	Photofragment Excitation Spectroscopy	10, 35, 39, 43, 44, 55, 91, 92
PMT	Photomultiplier Tube	36, 38

<b>Notation</b>	<b>Description</b>	<b>Page List</b>
PST	Phase Space Theory	xvii, 9–15, 17, 18, 22–24, 29, 30, 33, 54, 56, 81
QCT	Quasiclassical Trajectory	4, 7, 18, 33, 55, 89, 91, 93, 96, 98, 99
RDT	Reduced Dimensional Trajectory	xvii, xviii, 8, 9, 20, 25–27, 29, 32, 33, 54, 55
RMSE	Root Mean Square Error	20, 21, 25
SRS	Stanford Research Systems	37, 38
TNT	Template Numerical Toolkit, a collection of interfaces and reference implementations of numerical objects useful for scientific computing in C++ [3]	64
TS	Transition State	ii, vii, viii, 1, 4–6, 8, 9, 11, 18, 24, 27, 46, 48, 49, 70, 79, 83, 89–91, 93, 94, 96, 98
TSDS	Transition State Dividing Surface	1, 2, 4, 6, 7

<b>Notation</b>	<b>Description</b>	<b>Page List</b>
TST	Transition State Theory	ii, xx, 1, 2, 4, 6, 29, 45, 46, 48, 49, 52, 53, 55
VRC-TST	Variable Reaction Coordinate Transition State Theory	2, 48, 49, 53, 55, 56
VTST	Variational Transition State Theory	2, 4, 11, 45– 50, 52, 53, 55
ZPE	Zero Point Energy	7, 8, 11, 40, 45, 83, 98

## List of Figures

- 1.1 Frames of a sample CH<sub>3</sub>CHO roaming trajectory leading to CH<sub>4</sub> + CO. [4] 3
- 1.2 Schematic showing the tight transition state pathway (1) in green, the  $S_0$  two-body radical channel (2) in red, the roaming pathway (3) as the purple dashed line, the  $T_1$  two-body radical channel ?? in orange and the first singlet excited state ( $S_1$ ) in black. 5
- 2.1 Schematic PES showing the minimum translational energy required ( $E'_{tmin} = D_0 - V(r')$ ) for accessible rovibrational states at an arbitrary separation  $r = r'$  to lead to radical dissociation and the maximum allowed rovibrational energy ( $E_{rvmax} = E_{tot} - D_0$ ) for a state to form radicals. Inset, close up of the van der Waals region, showing the minimum translational energy required ( $E_{tmin} = D_0 - V(r_{roam}) = \Delta E_{roam}$ ) for accessible rovibrational states to lead to radical dissociation at  $r = r_{roam}$ , the minimum separation required for roaming. 12
- 2.2 The  $E_t$  distribution where  $E_A = E_{tot} - V(r_{roam}) = E_{tot} - D_0 + \Delta E_{roam}$ , the energy used for the PST count, corresponding to  $r = r_{roam}$ , the minimum separation at which roaming will occur. 13
- 2.3 The vector sum of the angular momentum of both fragments ( $\vec{J}_1$  and  $\vec{J}_2$ ) and their orbital angular momentum ( $\vec{L}$ ) must equal the total angular momentum of the reactant molecule ( $\vec{J}_{parent}$ ). 14
- 2.4 Experimental branching fractions for H<sub>2</sub>CO ( $E_{tot} = 30000 - 32500 \text{ cm}^{-1}$ ). Adapted from Figure 8 in Ref [5], solid points, with additional points from [6], hollow points. Table 2.1 lists the values plotted in this figure. 19
- 2.5 Figure 12 in Ref [7], branching of the roaming and radical channels of CH<sub>3</sub>CHO, as predicted by RDT calculations. 21

- 2.6 For H<sub>2</sub>CO, modelled radical and roaming branching fractions in the range ( $E_{tot} = 30000 - 33100 \text{ cm}^{-1}$ ) where  $\Delta E_{roam} = 161 \text{ cm}^{-1}$  (red and blue lines respectively). The literature radical and roaming branching fractions (red squares and blue diamonds respectively) and upper and lower bounds for the roaming threshold (dark blue and green dashed lines respectively) have been overlayed for comparison. 21
- 2.7 For H<sub>2</sub>CO,  $\omega_{roam}(E_{tot})$  and  $\omega_{rad}(E_{tot})$  in the range ( $E_{tot} = 30000 - 35400 \text{ cm}^{-1}$ ) where  $\Delta E_{roam} = 161 \text{ cm}^{-1}$ . Inset, close up of the range ( $E_{tot} = 30170 - 30810 \text{ cm}^{-1}$ ) with the energy scale relative to  $D_0$  (30327.6 cm<sup>-1</sup>). [6] 22
- 2.8 The data from figure 2.6 with the energies at which the HCO vibrational levels become accessible for roaming and radical states indicated by the blue and red combs respectively. 23
- 2.9 For CH<sub>3</sub>CHO, In blue, modelled radical and roaming fractions in the range ( $E_{tot} = 28800 - 32800 \text{ cm}^{-1}$ ). The two darker blue lines are where the single parameter  $\Delta E_{roam}$  has been varied to fit the experimental or RDT data. The two lighter blue lines are results where  $\Delta E_{roam}$  has been set to a physically reasonable value. The RDT data [7] is shown in orange and the experimental data is shown in red [4] and yellow [8]. The radical threshold is indicated as a green dotted line. 26
- 2.10 For CH<sub>3</sub>CHO, In blue, modelled radical and roaming fractions in the range ( $E_{tot} = 28800 - 32800 \text{ cm}^{-1}$ ) where  $\Delta E_{roam}$  is held constant at 255 cm<sup>-1</sup>. The light blue line is where the single parameter  $P_{roam}$  has been varied to fit the experimental data point and the dark blue line is where the single parameter  $P_{roam}$  has been varied to fit RDT data. The RDT data [7] is shown in orange and the experimental data is shown in red [4] and yellow [8]. The radical threshold is indicated as a green dotted line. 30
- 2.11 For D<sub>2</sub>CO, In red and dark blue, the radical and roaming fractions in the range ( $E_{tot} = 30800 - 33800 \text{ cm}^{-1}$ ) where  $\Delta E_{roam} = 161 \text{ cm}^{-1}$  and  $P_{roam} = 1$ . 31
- 2.12 Comparison of the modelled H<sub>2</sub>CO and D<sub>2</sub>CO branching fractions, from figures 2.6 and 2.11, with the energy relative to their respective radical dissociation thresholds. 31
- 3.1 Top-view schematic of the vacuum chamber, indicating the orientation of the baffle arms, gauges and detection apparatus. 37

- 3.2 A comparison of LIF spectra probing formyl fragments produced via photolysis of  $\text{CH}_3\text{CHO}$   $\text{CD}_3\text{CDO}$  and  $\text{CH}_3\text{CDO}$  parent molecules, where  $\text{CH}_3\text{CDO}$  has been pumped with an energy below the  $T_1$  radical threshold ( $30668.0 \text{ cm}^{-1}$ ). 40
- 3.3 LIF spectra of formyl fragments produced via photolysis of  $\text{CH}_3\text{CDO}$  parent molecules, with various pump laser energies and the probe laser scanned in the range ( $\lambda = 258.2 - 259.4 \text{ nm}$ ). The  $t_1$  threshold is  $\sim 31400 \text{ cm}^{-1}$ . 42
- 3.4 PHOFEX spectra of formyl fragments produced by photolysis of  $\text{CH}_3\text{CDO}$  parent molecules, with the pump laser scanned in the range ( $\lambda = 312.2 - 329.6 \text{ nm}$ ). In black, DCO probed at  $258.756 \text{ nm}$ , in red, HCO probed at  $258.320 \text{ nm}$ . 43
- 3.5 As a function of photolysis energy, % HCO from  $\text{CH}_3\text{CDO}$  photolysis calculated from integration of LIF spectra (red circles) and relative intensities of PHOFEX spectra (red line). 44
- 3.6 Two step isomerisation pathway between  $\text{CH}_3\text{CDO}$  and  $\text{CH}_2\text{DCHO}$ . Energies are ZPE corrected and based on the best available literature values for  $\text{CH}_3\text{CHO}$  as described in Appendix B. 46
- 3.7 A three step isomerisation pathway between  $\text{CH}_3\text{CDO}$  and  $\text{CH}_2\text{DCHO}$ . Energies are ZPE corrected and based on the best available literature values for  $\text{CH}_3\text{CHO}$  as described in Appendix B 47
- 3.8 A three step isomerisation pathway between  $\text{CH}_3\text{CDO}$  and  $\text{CH}_2\text{DCHO}$ . Energies are ZPE corrected and based on the best available literature values for  $\text{CH}_3\text{CHO}$  as described in Appendix B 48
- 3.9 Four step isomerisation pathway between  $\text{CH}_3\text{CDO}$  and  $\text{CH}_2\text{DCHO}$ . Energies are ZPE corrected and based on the best available literature values for  $\text{CH}_3\text{CHO}$  as described in Appendix B 49
- 3.10 Schematic of the critical points on the PES for  $\text{C}_2\text{H}_3\text{DO}$ . The reactant,  $\text{CH}_3\text{CDO}$ , can react to the left forming primary products (illustrated in blue), or isomerise to the right, through a “maze” of intermediate structures (illustrated in green), which can continue to final products where H and D have been exchanged (illustrated in red). The minimum energy isomerisation pathway is illustrated in dark green and the

product channels producing DCO and HCO are illustrated in dark blue and dark red respectively.	50
3.11 As a function of photolysis energy, % HCO from CH <sub>3</sub> CDO photolysis and % DCO from CD <sub>3</sub> CHO photolysis calculated from integration of LIF spectra (red circles for HCO and blue squares for DCO), relative intensities of PHOFEX spectra (red line for HCO and blue line for DCO) and TST prediction for % HCO from CH <sub>3</sub> CDO photolysis including only the well known isomerisation pathways (green line).	52
C.1 For formaldehyde, $\omega_{roam}(E_A)$ and $\omega_{rad}(E_A)$ in the range ( $E_{tot} = 29000 - 34000 \text{ cm}^{-1}$ ) where $\Delta E_{roam} = 178 \text{ cm}^{-1}$ and $P_{roam} = 1$ . Inset, close up of a range starting at $E_{tot} = 29100 \text{ cm}^{-1}$ with the energy scale relative to $D_0$ (29274.5 cm <sup>-1</sup> ).	78
C.2 For formaldehyde, In red and dark blue, the radical and roaming fractions in the range ( $E_{tot} = 29000 - 34000 \text{ cm}^{-1}$ ) where $\Delta E_{roam} = 178 \text{ cm}^{-1}$ and $P_{reform} = 0.15$ . In pink and light blue, the equivalent radical and roaming fractions where $P_{roam} = 1$ ( $P_{reform} = 0$ ).	78
C.3 For acetaldehyde, $\omega_{roam}(E_A)$ and $\omega_{rad}(E_A)$ in the range ( $E_{tot} = 29000 - 34000 \text{ cm}^{-1}$ ) where $\Delta E_{roam} = 178 \text{ cm}^{-1}$ and $P_{roam} = 1$ . Inset, close up of a range starting at $E_{tot} = 29100 \text{ cm}^{-1}$ with the energy scale relative to $D_0$ (29274.5 cm <sup>-1</sup> ).	79
C.4 For acetaldehyde, In red and dark blue, the radical and roaming fractions in the range ( $E_{tot} = 29000 - 34000 \text{ cm}^{-1}$ ) where $\Delta E_{roam} = 178 \text{ cm}^{-1}$ and $P_{reform} = 0.15$ . In pink and light blue, the equivalent radical and roaming fractions where $P_{roam} = 1$ ( $P_{reform} = 0$ ).	79
C.5 For propanal, $\omega_{roam}(E_A)$ and $\omega_{rad}(E_A)$ in the range ( $E_{tot} = 29000 - 34000 \text{ cm}^{-1}$ ) where $\Delta E_{roam} = 178 \text{ cm}^{-1}$ and $P_{roam} = 1$ . Inset, close up of a range starting at $E_{tot} = 29100 \text{ cm}^{-1}$ with the energy scale relative to $D_0$ (29274.5 cm <sup>-1</sup> ).	80
C.6 For propanal, In red and dark blue, the radical and roaming fractions in the range ( $E_{tot} = 29000 - 34000 \text{ cm}^{-1}$ ) where $\Delta E_{roam} = 178 \text{ cm}^{-1}$ and $P_{reform} = 0.15$ . In pink and light blue, the equivalent radical and roaming fractions where $P_{roam} = 1$ ( $P_{reform} = 0$ ).	80

- C.7 For butanal,  $\omega_{roam}(E_A)$  and  $\omega_{rad}(E_A)$  in the range ( $E_{tot} = 29000 - 34000 \text{ cm}^{-1}$ ) where  $\Delta E_{roam} = 178 \text{ cm}^{-1}$  and  $P_{roam} = 1$ . Inset, close up of a range starting at  $E_{tot} = 29100 \text{ cm}^{-1}$  with the energy scale relative to  $D_0$  ( $29274.5 \text{ cm}^{-1}$ ). 81
- C.8 For butanal, In red and dark blue, the radical and roaming fractions in the range ( $E_{tot} = 29000 - 34000 \text{ cm}^{-1}$ ) where  $\Delta E_{roam} = 178 \text{ cm}^{-1}$  and  $P_{reform} = 0.15$ . In pink and light blue, the equivalent radical and roaming fractions where  $P_{roam} = 1$  ( $P_{reform} = 0$ ). 81
- C.9 For  $(\text{CH}_3)_2\text{CO}$ ,  $\omega_{roam}(E_A)$  and  $\omega_{rad}(E_A)$  in the range ( $E_{tot} = 29000 - 34000 \text{ cm}^{-1}$ ) where  $\Delta E_{roam} = 178 \text{ cm}^{-1}$  and  $P_{roam} = 1$ . Inset, close up of a range starting at  $E_{tot} = 29100 \text{ cm}^{-1}$  with the energy scale relative to  $D_0$  ( $29274.5 \text{ cm}^{-1}$ ). 82
- C.10 For  $(\text{CH}_3)_2\text{CO}$ , In red and dark blue, the radical and roaming fractions in the range ( $E_{tot} = 29000 - 34000 \text{ cm}^{-1}$ ) where  $\Delta E_{roam} = 178 \text{ cm}^{-1}$  and  $P_{reform} = 0.15$ . In pink and light blue, the equivalent radical and roaming fractions where  $P_{roam} = 1$  ( $P_{reform} = 0$ ). 82
- C.11 Previously recorded LIF spectra of formyl fragments produced by photolysis of a  $\text{CD}_3\text{CHO}$  parent molecule, with various pump laser energies and the probe laser scanned in the range ( $\lambda = 258.2 - 259.4 \text{ nm}$ ). 83
- E.1 The methyl principal moments of inertia point along the  $x, y, z$  axes and the most unequal moment points along the reaction coordinate, which is on the  $z$  axis in this diagram. The formyl principal moments of inertia do not point along the  $x, y, z$  axes and the most unequal moment is closest to  $x$  axis which is perpendicular to the reaction coordinate. 86
- F.1 At high  $\vec{L}$ , a centrifugal barrier arises at  $V_{eff}(r^*)$ , where  $r^*$  is the bond length where the effective potential is maximum. Therefore states are only valid at  $r_{roam}$ , if  $E_t$  is large enough to account for this energy transfer. That is  $E_t \geq E_{tmin}$  where  $E_{tmin} = V_{eff}(r^*) - V_{eff}(r_{roam})$ . 92
- F.2 Potential energy diagrams illustrating the affect of  $J$  on the energy barrier to molecular products via a classic TS (left), and to radical dissociation (right). Note that

for the direct TS channel the energy of both reactants and the TS are raised at higher $J$ , while for dissociation to radical products the absence of an energy barrier results in higher $J$ reactants requiring less additional energy to dissociate. This effect can lead to rotational switching, where at low $J$ the classic TS channel (1) is favoured while at high $J$ the radical channel (2) is favoured.	93
G.1 Potential energy diagram for an impulsive reaction, where $E_{excess}$ is the energy that will be distributed statistically and $E_t$ is the energy that must become relative translational energy.	96
G.2 Experimental branching fractions for formaldehyde ( $E_{tot} = 30000 - 32500 \text{ cm}^{-1}$ ). Adapted from Figure 8 in Ref [5], with points added to reflect observations in [6]. Solid points from original figure, hollow points from [6].	99

## List of Tables

2.1	H <sub>2</sub> CO experimental branching fractions. [5, 6]	18
2.2	Lennard Jones Parameters.	24
2.3	$\Delta E_{roam}$ and LJ well depths for H <sub>2</sub> CO, CH <sub>3</sub> CHO and the Norrish I channels of propanal and <i>n</i> -butanal.	25
2.4	$\Delta E_{cross}$ and $\omega_{tot}(E_{cross})$ for H <sub>2</sub> CO, CH <sub>3</sub> CHO and the Norrish I channels of propanal and <i>n</i> -butanal where $\Delta E_{roam} = 178 \text{ cm}^{-1}$ .	32
B.1	Formaldehyde (H <sub>2</sub> CO) input values.	65
B.2	Formaldehyde- <i>d</i> 2 (D <sub>2</sub> CO) input values.	66
B.3	Acetaldehyde input values.	66
B.4	Propanal input values.	67
B.5	<i>n</i> -Butanal input values.	69
B.6	CH <sub>3</sub> CHO <i>S</i> <sub>0</sub> Stationary Point Energies.	70
B.7	CH <sub>3</sub> CDO <i>S</i> <sub>0</sub> Stationary Point Energies. (All ZPE corrections are MP2/6-311+G**) 71	71
B.8	CH <sub>3</sub> CDO <i>S</i> <sub>0</sub> Stationary Point Frequencies. (All calculations are MP2/6-311+G**) 72	72
B.9	CH <sub>3</sub> CDO rate coefficients near the the experimental photolysis energies.	76

## CHAPTER 1

### Introduction

---

## 1.1 Transition State Theory

Transition state theory (TST), a method for predicting reaction rates using quantum theory and statistical mechanics, is “recognised as one of the great achievements of theoretical chemistry”. [5] There are two key assumptions in TST. [9, 10] First we assume there exists a transition state dividing surface (TSDS) such that any trajectory originating as reactants that crosses this surface, irreversibly forms products. [9, 10] This assumption implies any TST rate is an upper bound of the true rate. The second assumption is the ergodic hypothesis, that all energetically accessible states of the system are equally probable. In practice, the ergodic hypothesis requires energy to be randomised amongst all internal degrees of freedom rapidly with respect to reaction time. [9, 10]

TST can accurately model unimolecular reactions that occur over an energy barrier via a “tight” (well defined) transition state (TS). [5, 9] The rate is obtained canonically as, [9, 10]

$$k_{TS}(T) = \frac{k_B T}{h} \frac{Q_{TS}}{Q_R} \exp\left(-\frac{E_{critical}}{k_B T}\right) \quad (1.1)$$

where  $Q_R$  and  $Q_{TS}$  are the partition functions of reactant and TS geometries respectively,  $h$  is Plank’s constant,  $k_B$  is Boltzmann’s constant and  $E_{critical}$  is the minimum energy required for reaction. [9] In other words,  $k_{TS}$  is proportional to the number of accessible states at the TS at temperature  $T$ . However, photodissociation experiments occur at a fixed excitation energy,  $E_{tot}$ . The microcanonical rate expression equivalent of equation 1.1 is, [9, 10]

$$k_{TS}(E_{tot}) = \frac{\omega_{TS}(E_{tot} - E_{critical})}{h\rho_R(E_{tot})} \quad (1.2)$$

where  $\omega_{TS}$  is the TS sum of states and  $\rho_R$  is the reactant density of states. [9]

Barrierless unimolecular dissociation to radical products, simple bond fission, can typically be modelled by Variational transition state theory (VTST). Recall that TST assumes all molecules that cross the TSDS will inevitably go on to form products. However, because barrierless dissociation occurs in flat potential energy surface (PES) regions, defining a TSDS where this no recrossing assumption holds is difficult. In VTST, the TSDS is obtained via variational minimisation of the TST predicted rate, giving an upper bound of the exact rate. This is traditionally achieved by varying a single parameter (the reaction coordinate), usually defined as a fixed separation between either the centres of mass of the two fragments or the atoms of the breaking bond. [11–13] It can be difficult to obtain quantitatively accurate VTST rates because the position along the reaction coordinate giving the minimum rate varies greatly with  $E_{tot}$  and/or total angular momentum ( $\vec{J}$ ). [13] The variational result can often be further reduced if the definition of the reaction coordinate is also varied, for example the variable reaction coordinate transition state theory (VRC-TST) approach, developed by Steven Klippenstein, has been shown to reduce the variational result by over a factor of two compared with the centres of mass definition for the reaction coordinate. [11–13]

## 1.2 Non-TST Reaction Mechanisms

There are other “types” of reaction mechanisms, with “unusual” dynamics, that are modelled poorly by TST and VTST. These are reactions that occur in multiconfigurational regions of configuration space with conical intersections or seams between potential energy surfaces (PESs) and/or PES regions with flat, or non saddle point topology. The most notable of these novel reaction mechanisms is termed “roaming”. [14]

Roaming occurs in the region of the unimolecular dissociation channel to radical products. However, rather than forming radicals, intramolecular abstraction yields molecular products, see figure 1.1. Roaming is considered an extreme example of a reaction occurring far from the minimum energy pathway (MEP). [5] Roaming reactions cannot be modelled using any variant of TST, because roaming violates both of the key assumptions of TST. Roaming reactions are

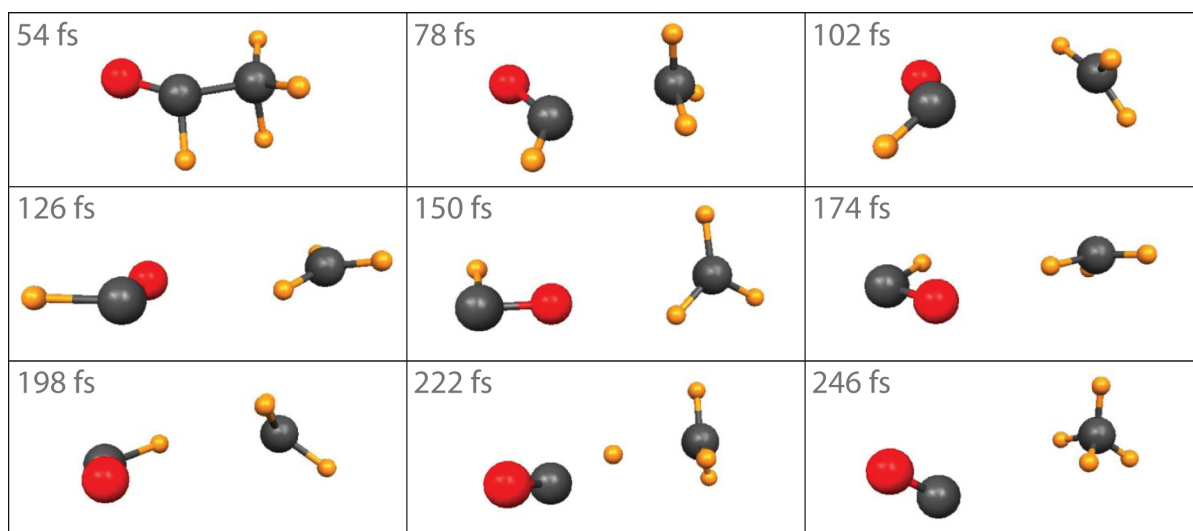


FIGURE 1.1: Frames of a sample  $\text{CH}_3\text{CHO}$  roaming trajectory leading to  $\text{CH}_4 + \text{CO}$ . [4]

not ergodic, because the reaction coordinate becomes too large for energy to be transferred between the two fragments. Furthermore, roaming occurs on a flat region of the potential energy surface (PES), the van der Waals region, where the probability for molecules recrossing the TSDS is far from negligible.

Roaming has been experimentally observed in the photodissociation of  $\text{H}_2\text{CO}$  (2004),  $\text{CH}_3\text{CHO}$  (2006) and acetone (2008). [15–17] At the 1st Conference on Roaming Dynamics and Multiple Mechanisms in Chemical Reactions (April 2010) [18] it was postulated that roaming also occurs in  $\text{CH}_3\text{NO}_2$ , saturated alkanes (propane, neo-pentane, iso-butane, dimethyl ether),  $\text{CH}_4$ ,  $\text{ROOH}$ ,  $\text{NO}_3$ ,  $\text{ROONO}$ , and the bimolecular reaction  $\text{CN} + \text{O}_2$ . It is likely a nearly universal phenomenon. [19–22] However, the majority of experimental roaming data is from  $\text{H}_2\text{CO}$  and  $\text{CH}_3\text{CHO}$  photodissociation.

### 1.3 Photodissociation Channels Of Small Aldehydes

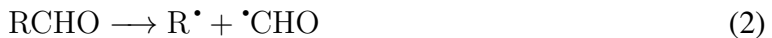
Photodissociation of formaldehyde ( $\text{H}_2\text{CO}$ ) and acetaldehyde ( $\text{CH}_3\text{CHO}$ ) can occur via multiple channels. [6, 16, 23] Initially photoexcitation is to the  $S_1$  singlet excited state. This is followed by internal conversion to a highly vibrationally excited state on the electronic ground

state,  $S_0$ , as illustrated in Figure 1.2. Three dissociation channels are also illustrated in Figure 1.2. Channel (1) leads to molecular products



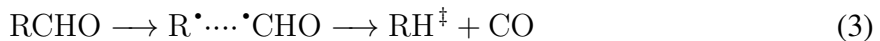
where R represents H or  $\text{CH}_3$ . This “conventional” route to these products is through a “tight” TS and hence can be modelled using TST expressions, where the TSDS contains the TS and is perpendicular to the path of steepest descent. [9] This minimum energy path MEP is illustrated in green in figure 1.2. The dynamics of channel (1) are consistent with an “impulsive” model, having high translational energy and low internal energy fragments. [24–26] This quantum signature is crucial in experimentally distinguishing between channel (1) and roaming products, and is explained in appendix G.

A second reaction channel for these molecules is a two-body radical dissociation via a “loose” transition state, [6, 16, 23]



Channel (2) is a barrierless reaction and this MEP is illustrated in red in figure 1.2. Such reactions can be modelled using VTST and product fragment energy is typically distributed statistically. [9]

In  $\text{H}_2\text{CO}$  and  $\text{CH}_3\text{CHO}$ , roaming (3) is an alternate pathway to molecular products that bypasses the tight TS MEP. [5, 8, 23] This path is illustrated as the purple dotted line in figure 1.2. Roaming can be described as



where the  $\text{R}^\bullet \dots \cdot\text{CHO}$  in equation (3) indicates that the fragments are interacting in the van der Waals region of configuration space. The double dagger indicates that the  $\text{RH}^\ddagger$  product in equation (3) is highly vibrationally excited. Roaming occurs at a “roaming threshold” energy below the radical dissociation energy. This mechanism still defies conventional theories of chemical kinetics, which are unable as yet to predict its the temperature and energy dependence of roaming reactions. [5]

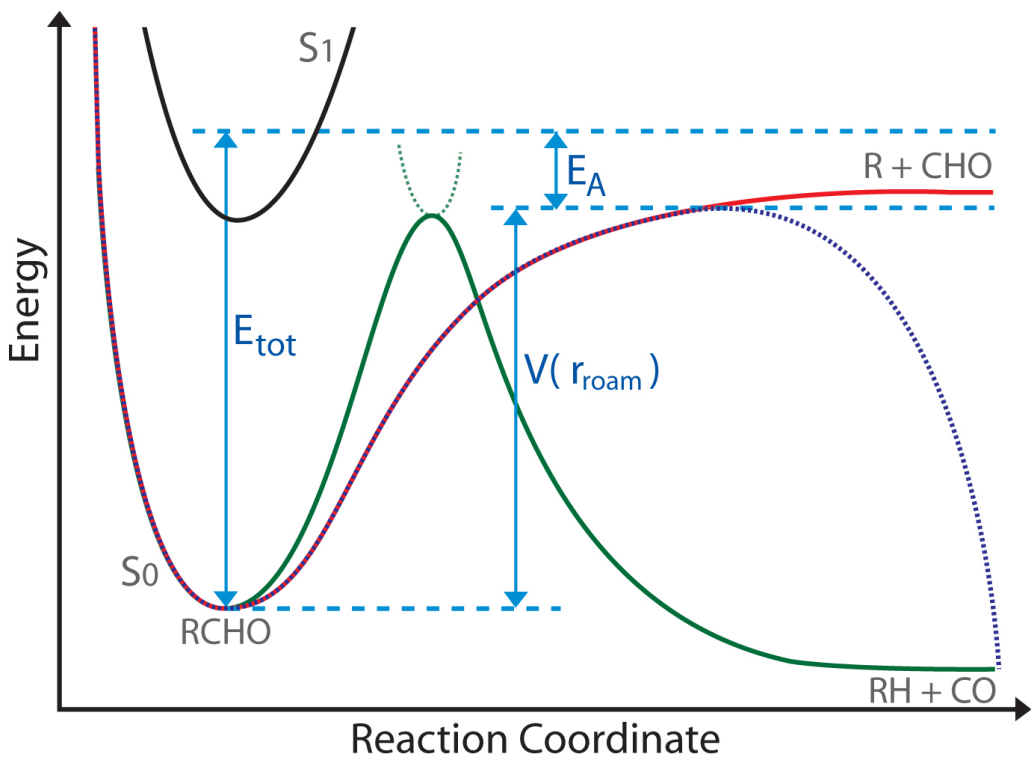


FIGURE 1.2: Schematic showing the tight transition state pathway (1) in green, the  $S_0$  two-body radical channel (2) in red, the roaming pathway (3) as the purple dashed line, the  $T_1$  two-body radical channel ?? in orange and the first singlet excited state ( $S_1$ ) in black.

The roaming channel, (3), starts similarly to dissociation to radical products, in that the bond that breaks in the radical channel becomes very long. [27] In a roaming mechanism, there is not enough energy in this bond for fission to occur and the fragments interact with each other at a distance governed only by long-range van der Waals attraction. During this interaction, one of these radical fragments encounters a hydrogen atom on the other fragment and intramolecular abstraction yields molecular products. This mechanism was confirmed for  $\text{H}_2\text{CO}$  photodissociation by the experimental imaging work of Suits *et al.* [14], for  $\text{CH}_3\text{CHO}$  photodissociation by the LIF experiments of Houston and Kable [8] and for both systems by the concurrent quasi-classical trajectory (QCT) calculations of the Bowman group. [28, 29] Michael *et al.* have also observed evidence for roaming in  $\text{CH}_3\text{CHO}$  combustion using the reflected shock tube technique with H(D)-atom ARAS detection. [30] The experimental evidence for roaming is reviewed in more detail in appendix G.

Based on this example [4], roaming is expected to be important in reactions where the energy thresholds for (1) and (2) are similar. Comparison of H<sub>2</sub>CO and CH<sub>3</sub>CHO suggests that as the critical energy of channel (1) increases with respect to the dissociation energy of channel (2), roaming becomes the dominant mechanism for molecular products because channel (2) is entropically favoured. [4] Figure 1.2 shows the channel (1) TS energy and the roaming threshold as almost isoenergetic, which is consistent with CH<sub>3</sub>CHO. [4] The TS energy for H<sub>2</sub>CO is considerably lower than the H<sub>2</sub>CO roaming threshold.

Harding *et al.* (2007) have identified roaming TS structures for both H<sub>2</sub>CO and CH<sub>3</sub>CHO using complete active space multi-reference second-order perturbation theory (CASPT2) calculations with the aug-cc-pVDZ basis set. [23] These TS are predicted to be 40 – 80 and  $\sim 350\text{ cm}^{-1}$  below the respective radical thresholds of H<sub>2</sub>CO and CH<sub>3</sub>CHO. Both *ab initio* roaming TS are located in the radical dissociation region of the PES. However, these TS are very low energy with respect to the rest of the PES (eg: imaginary frequency of 140 cm<sup>-1</sup> for H<sub>2</sub>CO) in this region and thus are not appropriate for standard TST calculations where the TSDS is orthogonal to the MEP. Such calculations using the H<sub>2</sub>CO roaming TS, predict a high pressure limit roaming rate (at 1000 K) orders of magnitude higher than is experimentally reasonable. [23]

## 1.4 Relevance Of Roaming In Small Aldehydes

The accuracy of reaction schemes for complex systems depends on our ability to model all relevant product channels and intermediates. Roaming reactions may be very important because molecular products are sinks in these schemes. That is, molecular products are unreactive or vastly less reactive than any radical intermediates formed. Without roaming, we may be underestimating the formation of molecular products, although we cannot assess the impact of roaming without reliable roaming rate coefficients.

Small aldehydes are involved in many important reaction schemes. For example, CH<sub>3</sub>CHO is an intermediate in oxygenated fuel combustion. [30, 31] Therefore, when modelling fuel oxidation, it is important to understand branching between the radical channel (2) and the roaming channel (3), and particularly, how this branching depends on temperature and pressure. [7, 30]

Aldehydes also have relevance to interstellar cloud chemistry. [30,32] H<sub>2</sub>CO is important in the atmospheric chemistry of ozone. H<sub>2</sub>CO is photochemically active in the troposphere, making it a source of OH and HO<sub>2</sub>. [33] H<sub>2</sub>CO is also involved in the formation of photochemical smogs, and is an oxidation product of many volatile organic compounds, including the most abundant hydrocarbon in the atmosphere, methane, a more potent greenhouse gas than CO<sub>2</sub>, [33]

## 1.5 Other Roaming Models

### Quasiclassical Trajectory Calculations

A number of groups have modelled roaming reactions in H<sub>2</sub>CO and CH<sub>3</sub>CHO. In particular, Bowman *et al.*'s (2004) QCT calculations were integral in identifying the roaming mechanism. [14] QCT calculations need a global PES, which itself requires very large numbers of *ab initio* calculations. Some PES regions require multiple determinants, while other regions can be modelled with faster and more accurate single determinant methods. [34] Joining regions calculated using different levels of theory and basis sets, requires scaling and smoothing in regions of overlap in the PES. [28] The use of high order polynomials to fit a functional form to the *ab initio* energy points can also introduce “wiggles” in the PES. Additionally, there may be significant fitting error between the *ab initio* values and the resultant functional form. [29]

Implementing such QCT calculations, however, is very difficult. Only a brief explanation is provided here, with a more detailed discussion provided in Appendix H. A number of approximations must be made when selecting initial quantum conditions for QCTs. [35] For example, Bowman *et al.* randomly distribute both available and zeropoint energy (ZPE) into harmonic normal modes, without considering the relative energies of each mode. [36] This initial distribution of energy governs the final trajectory and an inaccurate or unrealistic distribution may bias results. [9,35,37] Furthermore, this approach requires projection to the  $\vec{J}=0$  state. [36]

The uncertainty related to the treatment of ZPE is, perhaps, the biggest issue in QCT simulations. This is a general issue in comparing quantum and classical dynamics and, although a number of solutions have been proposed, there is no accepted way to account for ZPE in

classical simulations. [38–40] Bowman *et al.* put ZPE into each classical vibrational mode, but ZPE is a quantum property and does not occur in classical mechanics. In classical mechanics this ZPE can leak out, giving the molecule more energy in the reaction coordinate than should exist quantum mechanically for the given excitation energy. [40, 41] This can lead to unphysically large flux across the TSDS. This is particularly problematic for modelling CH<sub>3</sub>CHO dissociation, because when ZPE is included, the three-body radical dissociation channel RCHO → R<sup>•</sup> + H<sup>•</sup> + <sup>•</sup>CO is open, whereas it is closed if ZPE constraints are included. Because there are 3 fragments, this channel has enormous entropy and therefore high probability. These trajectories are discarded by Bowman *et al.*, as are any trajectories where the products have less energy than the ZPE. [42] This, again, introduces a potential source of bias in interpreting results.

## Reduced Dimensional Trajectory Calculations

The reduced dimensional trajectory (RDT) approach of Klippenstein *et al.* (2010), which involves the propagation of rigid-body trajectories on an analytic PES in the region of the roaming TS, reduces ambiguities related to ZPE conservation because the high energy internal vibrational modes are frozen. [7] RDT results are in reasonable agreement with the CH<sub>3</sub>CHO shock tube experiments of Michael *et al.* [30] The authors conclude that the roaming fraction of the total thermal dissociation (in the temperature range 1346 – 1888 K, at a few hundred Torr), is approximately 18%±10%. [7, 30] RDT theoretical branching ratios between channels (1) and (3) also agree well with the photodissociation results of Houston and Kable. [7, 8] However, the RDT approach still requires the generation of a molecule-specific PES and is therefore non-transferable.

## Statistical Treatments

Jürgen Troe's internally consistent statistical model, of both photolysis and combustion of S<sub>0</sub> H<sub>2</sub>CO, does not require large numbers of *ab initio* calculations. [43, 44] Troe models classical TS and roaming molecular products together, calculating an overall branching ratio between

molecular and radical products, without modelling a branching ratio between radical and roaming products. [43, 44] Here, we consider roaming as a form of frustrated radical dissociation and therefore explicitly model the branching ratio between radical and roaming products.

At the 1st Conference on Roaming Dynamics and Multiple Mechanisms in Chemical Reactions this year, Klippenstein *et al.* presented an unpublished statistical theory, based on Monte Carlo calculation of the relevant phase space integrals for the kinetics of roaming, that explicitly models the branching ratio between radical and roaming products. Their statistical analysis accurately reproduces the branching obtained from RDTs for low energies. However at higher energies (above 1 kcal·mol<sup>-1</sup>) increasingly large discrepancies arise, apparently due to a dynamical biasing towards continued decomposition of the incipient molecular fragments. [45] This method, however, also requires a detailed description of the PES in the region of the roaming TS and is, again, not easily transferable.

## 1.6 Theoretical Aims

This thesis aims to develop a model that can predict the fraction (branching ratio) of molecular dissociation products that arise via the roaming channel, (3), rather than the direct “transition state” channel, (1). Ideally we want to develop a simple, transferable model that captures the key physical properties of the process. The model should also be able to predict kinetic isotope effects.

We will start by analysing the energy dependence of the branching ratio, observed by Suits *et al.*, for the roaming and tight transition state molecular products of H<sub>2</sub>CO photodissociation. Experimental data is available over the energy range (29500 – 35400 cm<sup>-1</sup>). [6, 15, 27, 46] CH<sub>3</sub>CHO will then be analysed and compared to experimental results in the same way. Predictions will also be made for formaldehyde-*d*<sub>2</sub> (D<sub>2</sub>CO), propanal (C<sub>2</sub>H<sub>5</sub>CHO) and *n*-butanal (C<sub>3</sub>H<sub>7</sub>CHO).

Our goal is to develop a general statistical model for predicting roaming fractions by using phase space theory (PST) to calculate the number of states leading to frustrated radical dissociations. Such a model would allow roaming predictions without requiring the generation of computationally expensive and molecule specific global potential energy surfaces (PES).

## 1.7 Experimental Aims

The experimental work undertaken in this thesis continues laser induced fluorescence (LIF) and photo-fragment excitation (PHOFEX) experiments, using acetaldehyde-1-*d*<sub>1</sub> (CH<sub>3</sub>CDO) in addition to rerecording, in a wider spectral range, spectra of acetaldehyde-2,2,2-*d*<sub>3</sub> (CD<sub>3</sub>CHO). In previous experiments, CD<sub>3</sub>CHO LIF and PHOFEX spectra were recorded in order to characterise the radical dissociation channel (2) of CD<sub>3</sub>CHO, in preparation for ion imaging experiments seeking to analyse the kinetic isotope effect in CH<sub>3</sub>CHO roaming. However an unexpected facile H/D exchange was observed, producing far more DCO radical than expected.

The efficiency of this H/D exchange is unusual. At the beginning of the year we postulated that this isomerisation is the product of a roaming mechanism. An objective of this project was to examine this hypothesis, by using roaming rates obtained from our PST roaming model, and to explain the experimentally observed DCO and HCO populations.

## CHAPTER 2

### Phase Space Theory Roaming Model

---

## 2.1 Overview

In this work we consider roaming as a form of frustrated radical dissociation. [5, 6] That is we assume that the roaming channel (3) branches from the radical dissociation channel (2) late along the dissociation path, beyond the VTST TS. Once the bond between the roaming fragments becomes long enough, however, the system ceases to be ergodic; even when the system has enough energy to form radicals, energy can be trapped in other modes, preventing sufficient energy reaching the radical channel reaction coordinate. Hence the dissociation is frustrated.

The various energies discussed here are illustrated in figure 2.1. The available energy is defined as  $E_A = E_{tot} - V(r)$  where  $E_{tot}$  is the total excitation energy and  $V(r)$  is the ZPE corrected electronic potential energy at the chosen position along the reaction coordinate,  $r$ . Upon dissociation to radical products, excess reaction coordinate energy ( $E_{RC}$ ) becomes translational energy ( $E_t$ ) of the resultant fragments. Thus  $E_{RC} = V(r) + E_t$ . Thus the number of states that can form radical products in a phase space theory (PST) state count at distance  $r$  along the reaction coordinate will be the number of states satisfying the inequality

$$E_t \geq (D_0 - V(r)) \quad (2.1)$$

where  $D_0$  is the dissociation energy of the molecule, as illustrated in figure 2.1. Figure 2.2 illustrates the fraction of states satisfying this inequality at, say,  $r = r_{roam}$ , shaded blue. Here  $r_{roam}$  represents the minimum radical fragment separation for which roaming can occur. The maximum allowable rovibrational energy for states that form radical products is therefore

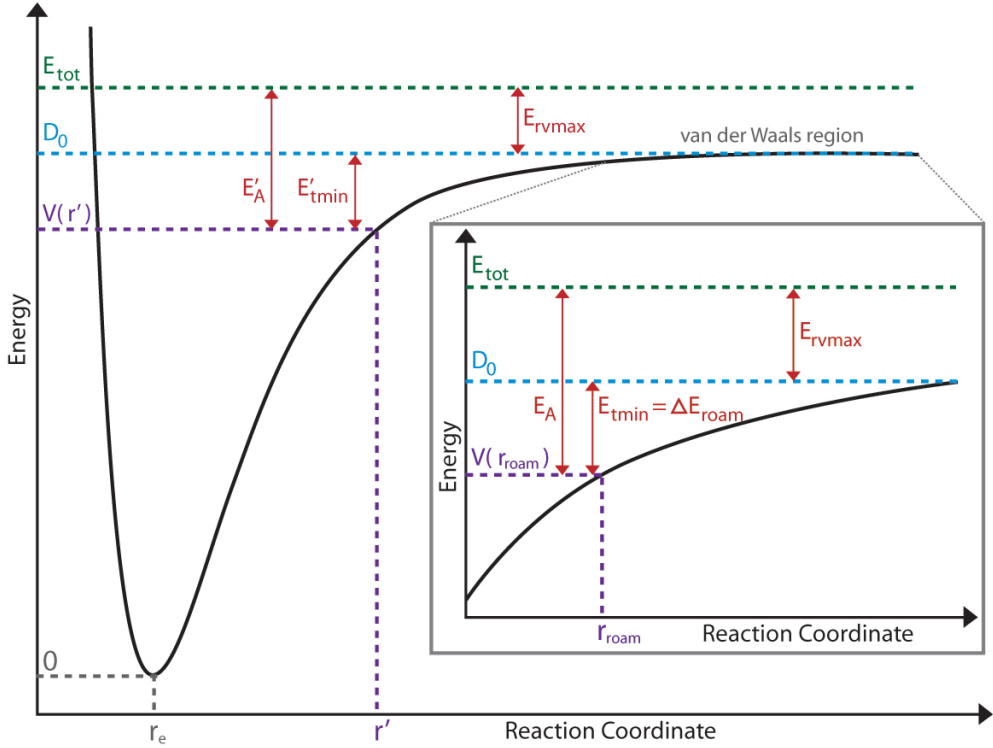


FIGURE 2.1: Schematic PES showing the minimum translational energy required ( $E'_{tmin} = D_0 - V(r')$ ) for accessible rovibrational states at an arbitrary separation  $r = r'$  to lead to radical dissociation and the maximum allowed rovibrational energy ( $E_{rvmax} = E_{tot} - D_0$ ) for a state to form radicals. Inset, close up of the van der Waals region, showing the minimum translational energy required ( $E_{tmin} = D_0 - V(r_{roam}) = \Delta E_{roam}$ ) for accessible rovibrational states to lead to radical dissociation at  $r = r_{roam}$ , the minimum separation required for roaming.

$E_{rvmax} = E_{tot} - D_0$ , as shown in the inset to figure 2.1. States with rovibrational energy exceeding  $E_{rvmax}$  cannot form radicals because we assume  $r_{roam}$  is large enough that ergodicity is lost. Thus there is no mechanism for rovibrational energy to be transferred to the reaction coordinate without first re-forming reactants.

Figure 2.2 plots the  $E_t$  distribution for all energetically available rovibrational states at  $r = r_{roam}$ . Figure 2.1 shows, indicatively, that  $r_{roam}$  is situated in the van der Waals region of the PES. The states forming radical products occupy the area under the curve satisfying inequality 2.1, shaded blue in figure 2.2. The states where roaming *may* occur occupy the area under the curve where

$$(D_0 - V(r) - \Delta E_{roam}) \leq E_t < (D_0 - V(r)) \quad (2.2)$$

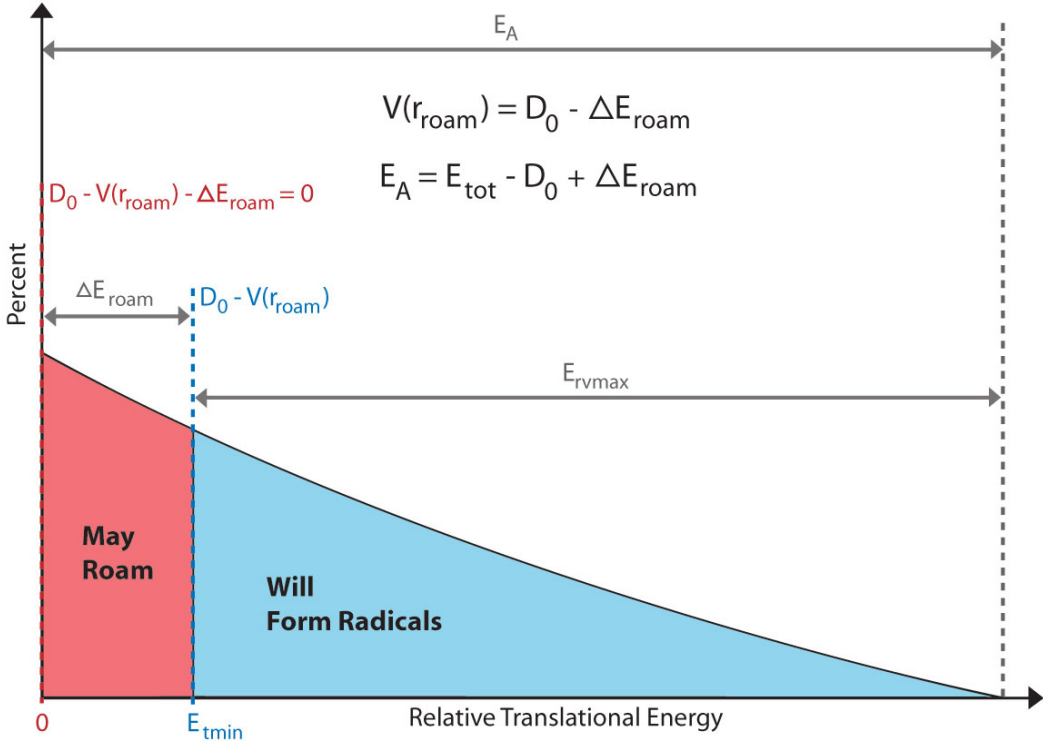


FIGURE 2.2: The  $E_t$  distribution where  $E_A = E_{tot} - V(r_{roam}) = E_{tot} - D_0 + \Delta E_{roam}$ , the energy used for the PST count, corresponding to  $r = r_{roam}$ , the minimum separation at which roaming will occur.

as indicated by the red shading in figure 2.2. The value of  $E_A$  used in our model is

$$E_A = E_{tot} - V(r_{roam}) = E_{tot} - D_0 + \Delta E_{roam} \quad (2.3)$$

which ensures all accessible states have sufficient  $E_t$  to either roam or form radicals, since  $(D_0 - V(r) - \Delta E_{roam})$  becomes 0, see figure 2.2.

## 2.2 Phase Space Theory

PST is a statistical method for calculating the sum of rovibrational states as a function of energy. PST calculates the phase space volume accessible at  $E_A$ , while conserving energy and angular momentum. [47–49] The iterative PST algorithm considers all permutations of vibrational and rotational quantum states of both fragments while applying two constraints: total energy and angular momentum must be conserved. Conservation of energy simply requires the overall

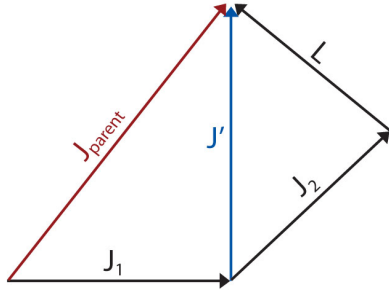


FIGURE 2.3: The vector sum of the angular momentum of both fragments ( $\vec{J}_1$  and  $\vec{J}_2$ ) and their orbital angular momentum ( $\vec{L}$ ) must equal the total angular momentum of the reactant molecule ( $\vec{J}_{parent}$ ).

rovibrational energy of both fragments is within  $E_A$ , with any excess energy being assigned to  $E_t$ . The total reactant angular momentum ( $\vec{J}_{parent}$ ) is conserved by adhering to two nested triangle inequalities, see figure 2.3. The outer inequality requires that

$$|\vec{J}_{parent}| \leq |\vec{J}_1| + |\vec{J}'| \quad (2.4)$$

where  $\vec{J}_1$  is the total angular momentum of the first fragment and  $\vec{J}'$  is the vector sum of the total angular momentum of the second fragment ( $\vec{J}_2$ ) and the orbital angular momentum ( $\vec{L}$ ) of the fragments, where  $\vec{L} = \mu \vec{v} \times \vec{b}$ , where  $\mu$  is the reduced mass of the fragments,  $\vec{v}$  the relative velocity of the fragments and  $\vec{b}$  the fragment separation (the impact parameter). [50] This corresponds to the triangle  $\vec{J}_{parent}\vec{J}_1\vec{J}'$  in figure 2.3 and ensures  $\vec{J}_{parent}$  is conserved. The inner inequality requires that  $\vec{L}$  is assigned to each quantum state such that, whatever  $\vec{J}_2$  is being considered in a given iteration, the vector sum of  $\vec{J}_2$  and  $\vec{L}$  satisfies the requirements of the outer triangle inequality.

$$|\vec{J}'| \leq |\vec{J}_2| + |\vec{L}| \quad (2.5)$$

## 2.3 Computer Code

A C++ computer program [51], was written to determine the PST total quantum sum of states ( $\omega_{tot}(E_{tot})$ ) for separating fragments at arbitrary positions along the reaction coordinate corresponding to reaction (2) as a function of  $E_{tot}$ . The sum of states that are frustrated ( $\omega_{roam}(E_{tot})$ ), that is, states where there is insufficient energy in the reaction coordinate for bond fission to

occur, and the sum of states that do have sufficient energy in the reaction coordinate to form radical products ( $\omega_{rad}(E_{tot})$ ) are also evaluated. Here,  $E_A$  is the energy difference between  $E_{tot}$  and  $V(r)$ . The radical product fraction is then given by

$$f_{rad} = \frac{\omega_{rad}(E_A)}{\omega_{tot}(E_A)} \quad (2.6)$$

The maximum roaming fraction is given by

$$f_{roam} = \frac{\omega_{roam}(E_A)}{\omega_{tot}(E_A)} \quad (2.7)$$

We fit the single parameter,  $\Delta E_{roam}$ , the energy difference between the radical and roaming thresholds, such that our  $f_{rad}$  and  $f_{roam}$  predictions agree with experimental H<sub>2</sub>CO  $f_{rad}$  and  $f_{roam}$  values. [27] This fit will be used as a guide to establishing a regime for predicting  $\Delta E_{roam}$  in generic cases.

Since we are modelling photodissociation experiments, where temperatures are low, we consider only  $\vec{J}_{parent} = 0$ . We intend to apply this model to combustion, requiring averaging over a large  $\vec{J}_{parent}$  range, requiring explicit treatment of collisions and centrifugal barriers.

All rigid rotor, harmonic oscillator quantum states satisfying the PST constraints described above are weighted by their total degeneracy ( $d^{tot}$ ) and included in  $\omega_{tot}$ . Since the H<sup>•</sup>, H<sup>•</sup>CO, CH<sub>3</sub><sup>•</sup> and CH<sub>3</sub><sup>•</sup>CO fragments are open shell doublets, the minimum degeneracy of any fragment quantum state is 2. All levels where the angular momentum about the principal moment of inertia ( $K$ ) is non zero, are doubly degenerate. [52]

Additionally, vibrational modes may have degeneracies greater than 1. Thus the total degeneracy is given by

$$d^{tot} = \prod_{i=1}^2 2d_i^{rot} d_i^{vib} \quad (2.8)$$

where  $d_i^{rot}$  and  $d_i^{vib}$  are the rotational and vibrational degeneracy of fragment  $i$  respectively. The translational degeneracy ( $d_i^{trans}$ ) is 1 because PST explicitly considers a 1 dimensional, *radial* translational density of states for the photofragments. The  $\vec{L}$  and  $m_L$  orbital quantum numbers account for the other 2 translational degrees of freedom implicitly. [49] The overall

PST algorithm is implemented as

$$\omega_{tot}(v_1, v_2, \vec{J}_1, \vec{J}_2; \vec{J}_{parent}, E_A) = \sum_{v_1=0}^{v_1^{max}(E_A)} \sum_{\vec{J}_1=0}^{\vec{J}_1^{max}(E_A, v_1)} \sum_{K_1=0}^{\vec{J}_1} \sum_{v_2=0}^{v_2^{max}(E_A, v_1, \vec{J}_1, K_1)} \\ \sum_{\vec{J}_2=0}^{\vec{J}_2^{max}(E_A, v_2, v_1, \vec{J}_1, K_1)} \sum_{K_2=0}^{\vec{J}_2} \sum_{\vec{J}'=\lvert \vec{J}_{parent}-\vec{J}_1 \rvert}^{\vec{J}_{parent}+\vec{J}_1} \sum_{\vec{L}=\lvert \vec{J}'-\vec{J}_2 \rvert}^{\vec{L} \leq \vec{J}'+\vec{J}_2} d^{tot} \quad (2.9)$$

where each sum represents a nested loop. Appendix D describes this algorithm in more detail.  $v_i$ ,  $\vec{J}_i$  and  $K_i$  are the quantum numbers for all possible vibrations, total angular momenta and angular momenta about the principal moment of inertia for fragment  $i$  respectively. The  $v_i$  loops are over all vibrational states of fragment  $i$ .  $v_i^{max}$  and  $\vec{J}_i^{max}$ , the maximum values for  $v_i$  and  $\vec{J}_i$ , are dependent on the remaining available energy after the energy associated with the quantum numbers assigned in their parent loops has been assigned ( $E_{rem}$ ). This is represented by a dependence on the previously assigned quantum numbers. This algorithm assigns equal probability to each pair of fragment quantum states, regardless of their  $E_t$ . It has been shown that doing so satisfies the requirements for detailed balance. [48, 49]

To calculate rotational energy levels, the principal rotational constants are required for both fragments. Our code can either calculate these, as the eigenvalues of the moment of inertia tensor, or accept experimental values as inputs. With the exception of single atom fragments, for which  $E(\vec{J}, K) = 0$ , all fragments are approximated as rigid rotor symmetric tops. In general, this is a good approximation in molecular systems. [53]

Rotational energy is therefore given by

$$E(\vec{J}, K) = \vec{B}\vec{J}(\vec{J}+1) + (\vec{A}-\vec{B})K^2 \quad (2.10)$$

where  $\vec{J}$  is the total angular momentum,  $\vec{A}$  is the most unequal principal rotational constant and  $\vec{B}$  is the arithmetic mean of the other two (similar) rotational constants. [53]

$\vec{J}_i^{max}$  for a given energy is dependent on whether a fragment is better approximated as a prolate top or an oblate top. For prolate tops ( $\vec{A} > \vec{B}$ ),

$$\vec{J}_i^{max}(E_{rem}) = \frac{-\vec{B} + \sqrt{\vec{B}^2 + 4\vec{B}E_{rem}}}{2\vec{B}} \quad (2.11)$$

while for oblate tops,

$$\vec{J}_i^{max}(E_{rem}) = \frac{-\vec{B} + \sqrt{\vec{B}^2 + 4\vec{A}E_{rem}}}{2\vec{A}} \quad (2.12)$$

The rotational energy associated with fragment orbital motion is

$$E_{orb} = \frac{\vec{L}^2}{2I} \quad (2.13)$$

where  $I = \mu r^2$  and  $\mu$  is the reduced mass of the separating fragments and  $r$  is the centre-of-mass separation. When PST is normally applied, the fragments are assumed to be “infinitely” separated. Thus, for  $r \rightarrow \infty$ ,  $E_{orb} \rightarrow 0$ , and there is no energy component to remove for non zero  $\vec{L}$ . However in our PST model the fragments are not infinitely separated. Calculating  $E_{orb}$  requires a value for  $r$ , which would require a PES. We are trying to avoid using a PES in our model because we want it to be easily transferable, so we make the assumption that  $E_{orb} = 0$ , slightly overestimating  $E_t$  for states with non zero  $\vec{L}$ , favouring radicals. However we expect this effect to be minor, as  $r_{roam}$  is quite large. [23]

Since we intend to model generic cases in the future, our code is designed to accommodate generic cases wherever possible. This involves accepting inputs for an arbitrary number of atomic coordinates and elemental information, accompanied by data defining which atoms belong to each fragment and which atoms are attached to either end of the breaking bond approximating the radical reaction coordinate. Accommodating generic cases also requires the input of an arbitrary number of vibrational energy levels and their degeneracies for each fragment. The vibrational levels can be input in two ways: As a full experimental set, including fundamentals, combination bands and overtones; or as experimental or *ab initio* harmonic frequencies, from which combination bands and overtones are automatically calculated using a harmonic oscillator approximation. For all calculations presented in this thesis, vibrational levels are input

TABLE 2.1: H<sub>2</sub>CO experimental branching fractions. [5, 6]

Energy (cm <sup>-1</sup> )	$\frac{Rad}{Rad+TS+Roam}$	$\frac{TS}{Rad+TS+Roam}$	$\frac{Roam}{Rad+TS+Roam}$	$f_{rad}$	$f_{roam}$	Ref
30120	0.00	1.00	0.00	-	-	[6]
30241	0.00	0.82	0.18	0.000	1.000	[6]
31150	0.54	0.31	0.15	0.783	0.217	[5]
31750	0.72	0.18	0.10	0.878	0.122	[5]
32000	0.75	0.15	0.10	0.882	0.118	[6]
32150	0.75	0.15	0.10	0.882	0.118	[5]

as experimental fundamentals, where available, or as harmonic normal mode frequencies. All input data is tabulated in Appendix B.

## 2.4 Experimental Roaming Data

Roaming is not limited to energies near the radical-radical threshold. In H<sub>2</sub>CO photodissociation, roaming has been observed from below the threshold for radical dissociation on  $S_0$ , (30328 cm<sup>-1</sup>) (2), up to the threshold for three-body radical dissociation, RCHO → R<sup>•</sup> + H<sup>•</sup> + CO (35217 cm<sup>-1</sup>). [5] This covers a range of about 5000 cm<sup>-1</sup>, or 60 kJ·mol<sup>-1</sup> in excitation energy.

Experimentally, the threshold for roaming in H<sub>2</sub>CO is known to lie between 30123 and 30241 cm<sup>-1</sup>, which is between 87 and 205 cm<sup>-1</sup> below the radical threshold. [6] In our nomenclature, therefore,  $87 < \Delta E_{roam} < 205$  cm<sup>-1</sup> for H<sub>2</sub>CO. Experimental data in the range 30150 – 32000 cm<sup>-1</sup>, combined with QCT calculations, show that within this energy range the branching fraction for the tight transition state channel (1) decreases from 0.82 to 0.15, the radical (2) fraction increases from 0.0 to 0.75, and the roaming (3) fraction decreases from 0.18 to 0.10. [6, 27] This is illustrated in figure 2.4, which has been adapted from [5] with points added to reflect additional results published in [6]. Table 2.1 lists the values plotted in figure 2.4 as well as roaming to radical branching fractions, that is, excluding the tight TS channel. For H<sub>2</sub>CO, as we consider roaming as a frustrated radical channel, we fit our PST model to the roaming to radical branching fractions, columns 5 and 6 in table 2.1.

Experimetal studies of CH<sub>3</sub>CHO photodissociation dynamics provide only two experimental data points, both at 308 nm ( $\sim 32470$  cm<sup>-1</sup>), which report the roaming to tight TS branching

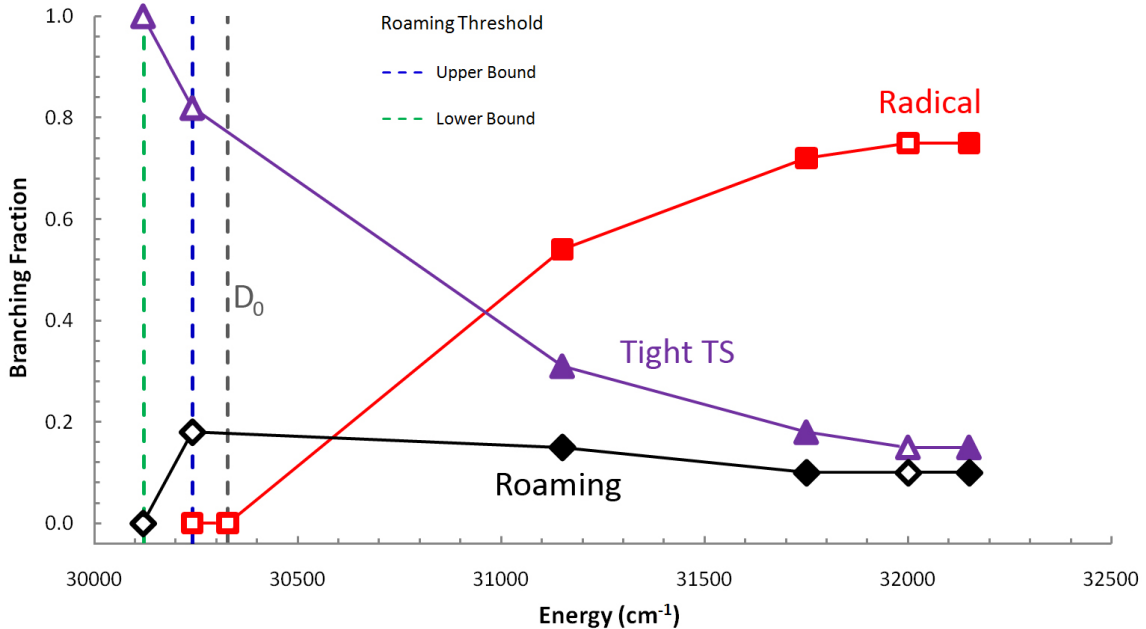


FIGURE 2.4: Experimental branching fractions for  $\text{H}_2\text{CO}$  ( $E_{tot} = 30000 - 32500 \text{ cm}^{-1}$ ). Adapted from Figure 8 in Ref [5], solid points, with additional points from [6], hollow points. Table 2.1 lists the values plotted in this figure.

fraction ( $f_{RTS}$ ) as 0 : 70 (under molecular beam conditions) and 0 : 84 (at room temperature). [4, 8] (note that the value reported in reference [8] was revised upwards to 0 : 70 from 0 : 15. [54])

The experiments, however, present roaming as a fraction of roaming to the total molecular products, that is they report

$$f_{RTS} = \frac{\omega_{roam}}{\omega_{roam} + \omega_{TS}} \quad (2.14)$$

where  $\omega_{roam}$  and  $\omega_{TS}$  represent the total number of molecular products formed via the roaming and tight TS channels respectively. In order to fit  $\Delta E_{roam}$  in the same way as for  $\text{H}_2\text{CO}$ , we must convert the literature fraction into a ratio of roaming and radical products:

$$f_{RR} = \frac{\omega_{roam}}{\omega_{roam} + \omega_{rad}} = f_{roam} \quad (2.15)$$

We can obtain  $f_{RR}$  from the experimental  $f_{RTS}$  by noting that

$$\frac{1}{f_{RTS}} = 1 + \frac{(1 - f_{RR}) k_{TS}}{f_{RR} k_{rad}} \quad (2.16)$$

where  $k_{rad}$  and  $k_{TS}$  are the rates for the radical (2) and tight TS (1) channels respectively. Conversely, these rates can be used to find the  $f_{RR}$  value required to match an experimental result, as

$$\frac{1}{f_{RR}} = 1 + \frac{(1 - f_{RTS})}{f_{RTS}} \frac{k_{rad}}{k_{TS}} \quad (2.17)$$

We have used rates provided by Klippenstein *et al.* [55] ( $k_{TS} = 1.11 \times 10^6 \text{ s}^{-1}$  and  $k_{rad} = 2.70 \times 10^8 \text{ s}^{-1}$ ) to obtain a range ( $f_{RR} = 9.50 \times 10^{-3} - 2.11 \times 10^{-2}$ ) based on the experimental observations in references [8] and [4] at  $32470 \text{ cm}^{-1}$ . For  $\text{CH}_3\text{CHO}$ , we fit to  $f_{RR} = 2.11 \times 10^{-2}$  which is obtained from the experimental observations of Osborn *et al.* ( $f_{RTS} = 0.84 \pm 0.1$ ). [4] The uncertainty in this value is large for the following reasons: the uncertainty in the experimental measurements is already  $\sim 10\%$ ; added to this is the uncertainty in the rates required to convert the experimental value into a ratio of roaming and radical products, 50 – 100% for  $k_{TS}$  and 100 – 150% for  $k_{rad}$ . We therefore consider the error in our experimental  $f_{RR}$  fit point to be about an order of magnitude and consider predictions of 0 – 10% roaming at  $32470 \text{ cm}^{-1}$  to be in good agreement with the experimental data.

Klippenstein *et al.*'s RDT calculations also report a ratio of roaming and radical products as a function of energy, [7] see figure 2.5. This provides an additional benchmark for the performance of our PST model when  $\Delta E_{roam}$  is set to the equivalent value ( $385 \text{ cm}^{-1}$ ) used in the RDT analysis. Alternatively the RDT branching fractions can be used to enable us to fit  $\Delta E_{roam}$ .

## 2.5 Formaldehyde Results

Figure 2.6 shows the energy dependence of the roaming and radical reaction in  $\text{H}_2\text{CO}$ , as calculated by our model. In this calculation, the energy was varied from  $E_{tot} = 30000 - 35400 \text{ cm}^{-1}$ , although the results have been truncated in the figure to overlap with the experimental region. A single parameter,  $\Delta E_{roam}$ , was varied in the simulation until the best fit with experiment was obtained, by minimising the root mean square error (RMSE), which provided  $\Delta E_{roam} = 161 \pm 2 \text{ cm}^{-1}$ . In this case the RMSE was  $0.026 \text{ cm}^{-1}$ . The experimental values are

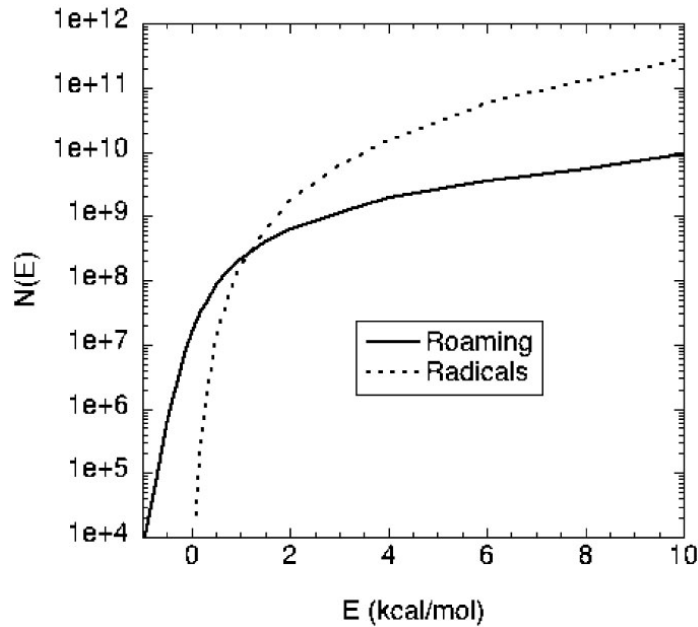


FIGURE 2.5: Figure 12 in Ref [7], branching of the roaming and radical channels of  $\text{CH}_3\text{CHO}$ , as predicted by RDT calculations.

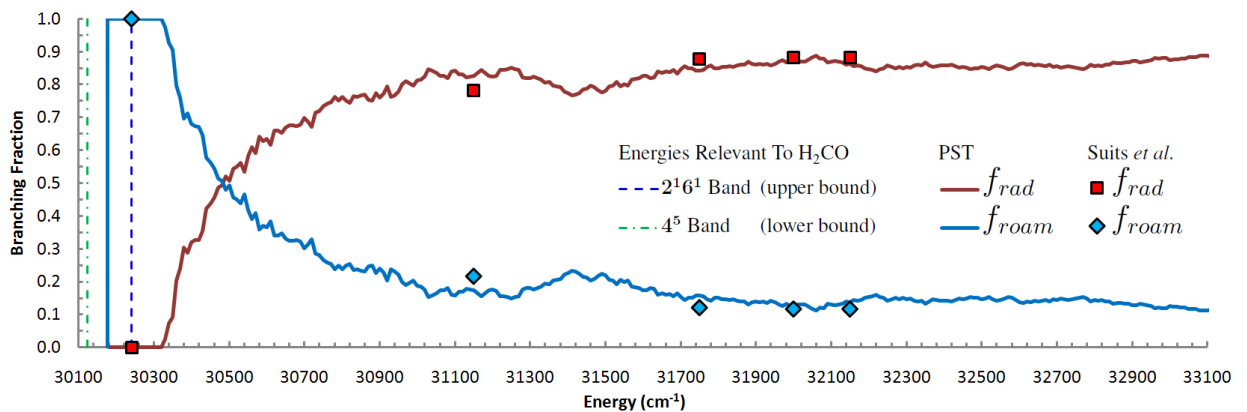


FIGURE 2.6: For  $\text{H}_2\text{CO}$ , modelled radical and roaming branching fractions in the range ( $E_{\text{tot}} = 30000 - 33100 \text{ cm}^{-1}$ ) where  $\Delta E_{\text{roam}} = 161 \text{ cm}^{-1}$  (red and blue lines respectively). The literature radical and roaming branching fractions (red squares and blue diamonds respectively) and upper and lower bounds for the roaming threshold (dark blue and green dashed lines respectively) have been overlaid for comparison.

accurate to at best 10%; the error in the model  $\Delta E_{\text{roam}}$  above represents the range of  $\Delta E_{\text{roam}}$  values having the same RMSE to two significant figures.

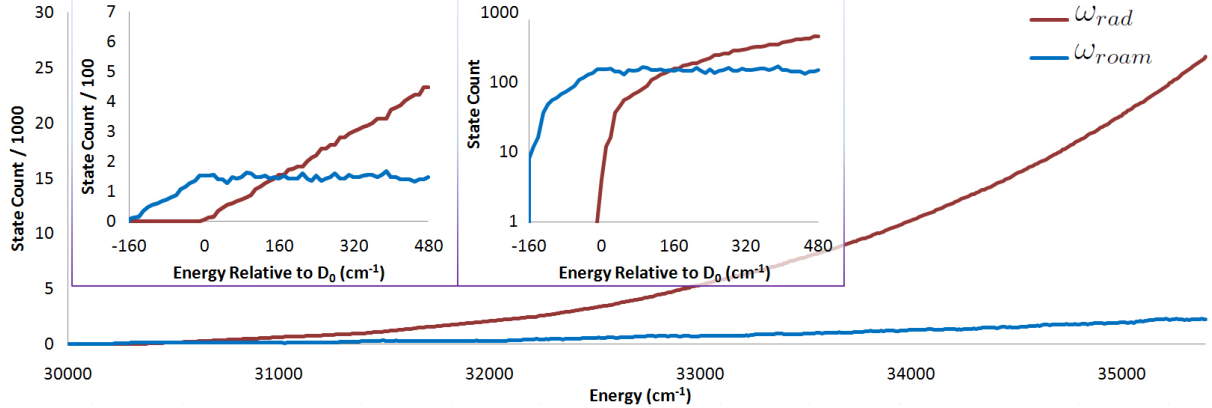


FIGURE 2.7: For  $\text{H}_2\text{CO}$ ,  $\omega_{roam}(E_{tot})$  and  $\omega_{rad}(E_{tot})$  in the range ( $E_{tot} = 30000 - 35400 \text{ cm}^{-1}$ ) where  $\Delta E_{roam} = 161 \text{ cm}^{-1}$ . Inset, close up of the range ( $E_{tot} = 30170 - 30810 \text{ cm}^{-1}$ ) with the energy scale relative to  $D_0$  ( $30327.6 \text{ cm}^{-1}$ ). [6]

The single parameter model provides a very good fit to the available experimental data. The RMSE in the roaming and radical fractions is  $0.026 \text{ cm}^{-1}$ , and the largest error is only  $0.039 \text{ cm}^{-1}$  (4% absolute), which is well within the experimental uncertainty. The value of  $E_{roam} = 161 \text{ cm}^{-1}$ , that was fit in the model, also lies comfortably within the experimental bound of  $87 - 205 \text{ cm}^{-1}$ , as indicated by the blue and green dashed lines in the figure. [6, 27]

Figure 2.7 shows  $\omega_{roam}$  and  $\omega_{rad}$  in the range ( $E_{tot} = 30000 - 35400$ ), clearly illustrating the radical channel dominating as energy increases, while the roaming channel flux increases relatively slowly. Figure 2.6 shows distinct structure, both on a high frequency scale ( $\sim 800 - 1000 \text{ cm}^{-1}$ ), and on a low frequency scale. The high frequency broad structure arises as different vibrational states of the HCO product become energetically available. The roaming fraction increases after each vibrational level opens, due to the increased density of states that results from this extra degree of freedom. The same vibrational level becomes available to radical states  $\Delta E_{roam} \text{ cm}^{-1}$  higher in energy. Thus the broad structure which is mirrored in the roaming and radical fractions reflects the HCO vibrational density of states. Figure 2.8 shows the same data, with the HCO vibrational energy levels indicated explicitly. The low frequency, fine structure, arises from the different rotational states of the HCO fragment becoming available. Because the rotational states are quantised, the HCO rotational density of states does not increase smoothly.

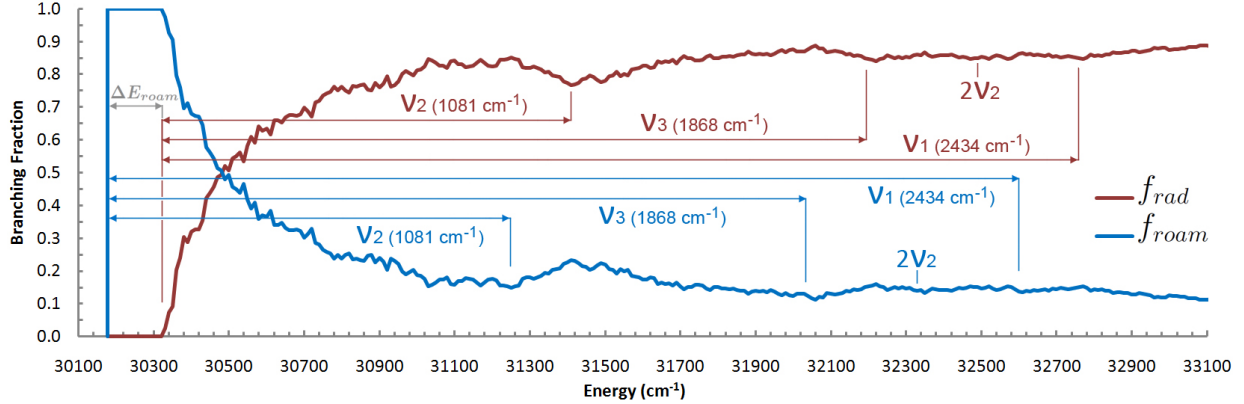


FIGURE 2.8: The data from figure 2.6 with the energies at which the HCO vibrational levels become accessible for roaming and radical states indicated by the blue and red combs respectively.

Overall, the PST-roaming model developed in this work reproduces all available experimental observables for H<sub>2</sub>CO; the roaming and radical branching ratio, and the energy threshold at which roaming starts ( $\Delta E_{roam}$ ).

## 2.6 Predicting $\Delta E_{roam}$

For our PST-roaming model to be predictive, we need a rationale for predicting  $\Delta E_{roam}$  in generic cases. Recall that figure 2.1 illustrates the relationship between the PES,  $\Delta E_{roam}$  and the roaming threshold bondlength ( $r_{roam}$ ). In principle we need an *ab initio* PES to derive an accurate value for  $\Delta E_{roam}$  and  $r_{roam}$ . However, if we can model the PES in a transferable way, we can make predictions for  $\Delta E_{roam}$  for systems where no *ab initio* PES is available.  $\Delta E_{roam}$  and  $r_{roam}$ , however, will depend on the van der Waals interactions between the dissociating fragments, which is not modelled by the schematic Morse potential shown in figure 2.1. A more accurate description of the van der Waals region of the PES is required to predict  $\Delta E_{roam}$ .

In an attempt to predict  $\Delta E_{roam}$ , we use the Lennard Jones (LJ) potential to approximate the attractive forces between fragments in the van der Waals region. The LJ parameters for H<sup>•</sup>, ·CH<sub>3</sub>, ·C<sub>2</sub>H<sub>5</sub> and ·C<sub>3</sub>H<sub>7</sub> are approximated as the H<sub>2</sub>, CH<sub>4</sub>, C<sub>2</sub>H<sub>6</sub> and C<sub>3</sub>H<sub>8</sub> LJ parameters respectively. The LJ parameters for H<sup>•</sup>CO are approximated using the LJ parameters for HCCH,

TABLE 2.2: Lennard Jones Parameters.

Species	$\sigma$ (Å)	$\frac{\epsilon}{k}$ (K)	Ref
H <sub>2</sub>	2.827	59.7	[57]
CH <sub>4</sub>	3.758	148.6	[57]
C <sub>2</sub> H <sub>6</sub>	4.443	215.7	[57]
C <sub>3</sub> H <sub>8</sub>	5.118	237.1	[57]
HCCH	4.033	231.8	[57]
H + HCO	3.43	117.6	this work
CH <sub>3</sub> + HCO	3.896	185.6	this work
C <sub>2</sub> H <sub>5</sub> + HCO	4.238	223.6	this work
C <sub>3</sub> H <sub>7</sub> + HCO	4.576	234.4	this work

as used previously by Timonen *et al.* [56] Table 2.2 lists the LJ parameters used to obtain LJ PESs for H<sub>2</sub>CO, CH<sub>3</sub>CHO, propanal and *n*-butanal.

The LJ potential is given by

$$V_{LJ}(r) = 4\epsilon_{AB} \left[ \left( \frac{\sigma_{AB}}{r} \right)^{12} - \left( \frac{\sigma_{AB}}{r} \right)^6 \right] \quad (2.18)$$

where  $r$  is the inter-particle distance and  $\epsilon_{AB}$  and  $\sigma_{AB}$  are the LJ parameters for the interaction between species  $A$  and  $B$ , affecting the well depth and the  $r$  where the inter-particle potential ( $V_{LJ}(r)$ ) is zero respectively. Combining LJ parameters to obtain an LJ potential between two different species requires taking the arithmetic mean of the  $\sigma$  values and the geometric mean of the  $\epsilon$  values of each species. [9] That is

$$\sigma_{AB} = \frac{\sigma_A + \sigma_B}{2} \quad (2.19)$$

and

$$\epsilon_{AB} = \sqrt{\epsilon_A \epsilon_B} \quad (2.20)$$

The resulting LJ well depths and minima are shown in table 2.2. Both the roaming transition states of Harding *et al.* and the LJ potential predict larger dispersion interactions between the methyl and formyl fragments of CH<sub>3</sub>CHO, compared with H<sub>2</sub>CO, suggesting  $\Delta E_{roam}$  for CH<sub>3</sub>CHO should be larger than for H<sub>2</sub>CO. [23] The CH<sub>3</sub>CHO *ab initio* roaming TS, however, is more stable than the LJ model would predict. Harding *et al.* predict the H<sub>2</sub>CO *ab initio* roaming TS to be 40 – 80 cm<sup>-1</sup> below the radical threshold, which is similar to the LJ prediction

TABLE 2.3:  $\Delta E_{roam}$  and LJ well depths for H<sub>2</sub>CO, CH<sub>3</sub>CHO and the Norrish I channels of propanal and *n*-butanal.

Species	$E_{LJ}$ (cm <sup>-1</sup> )	$\Delta E_{roam}$ (cm <sup>-1</sup> )	$r_{LJmin}$ (Å)
H <sub>2</sub> CO	81.3	161	3.9
CH <sub>3</sub> CHO	129	255	4.4
C <sub>2</sub> H <sub>5</sub> CHO	155	306	4.8
C <sub>3</sub> H <sub>7</sub> CHO	163	323	5.1

( $E_{LJ}$ ). However the CH<sub>3</sub>CHO *ab initio* roaming TS is  $\sim 350$  cm<sup>-1</sup> below the radical threshold, almost double  $E_{LJ}$ . Similarly, our PST single parameter fit to the H<sub>2</sub>CO experimental data points predicts  $\Delta E_{roam}$  is almost double  $E_{LJ}$ . We speculate, however, that  $\Delta E_{roam}$  is related to the magnitude of the van der Waals interaction and, in the first instance, linearly scale the LJ well depth using the values of  $\Delta E_{roam}$  for H<sub>2</sub>CO and the point (0, 0); when there are no van der Waals forces there will be no roaming. The resulting predictions of  $\Delta E_{roam}$  are shown in table 2.3.

## 2.7 Acetaldehyde Results

Figure 2.9 shows the energy dependence of the roaming fraction in CH<sub>3</sub>CHO, as calculated by our model using four different  $\Delta E_{roam}$  values (16, 122, 255 and 385 cm<sup>-1</sup>). In this calculation, the energy was varied from  $E_{tot} = 28800 - 32800$  cm<sup>-1</sup>. The first value,  $\Delta E_{roam} = 16$  cm<sup>-1</sup>, was obtained similarly to that for H<sub>2</sub>CO by varying  $\Delta E_{roam}$  until the best RMSE fit with the experimental data point (shown as a red diamond in figure 2.9) of Osborn *et al.* was obtained. In this case the RMSE was 0.0027 cm<sup>-1</sup>. The same technique was used to obtain a best fit to five points (shown as triangles in figure 2.9) taken from the RDT results of Klippenstein *et al.*, [7] providing the second value,  $\Delta E_{roam} = 122$  cm<sup>-1</sup> with a RMSE of 0.11 cm<sup>-1</sup>. Both of these values of  $\Delta E_{roam}$  are much lower than the fitted value for H<sub>2</sub>CO (161 cm<sup>-1</sup>), which is not physically what we expect based on either the roaming transition states of Harding *et al.* [23] or the LJ potential. The third value,  $\Delta E_{roam} = 255$  cm<sup>-1</sup>, is our LJ prediction, which yields a RMSE of 0.27 cm<sup>-1</sup> with respect to experiment and 0.25 cm<sup>-1</sup> with respect to the five RDT fit points. The fourth value (385 cm<sup>-1</sup>) is based on the RDT calculations. Klippenstien *et al.* use 385 cm<sup>-1</sup> (1.1 kcal·mol<sup>-1</sup>) as a critical energy for the roaming channel, basing this on

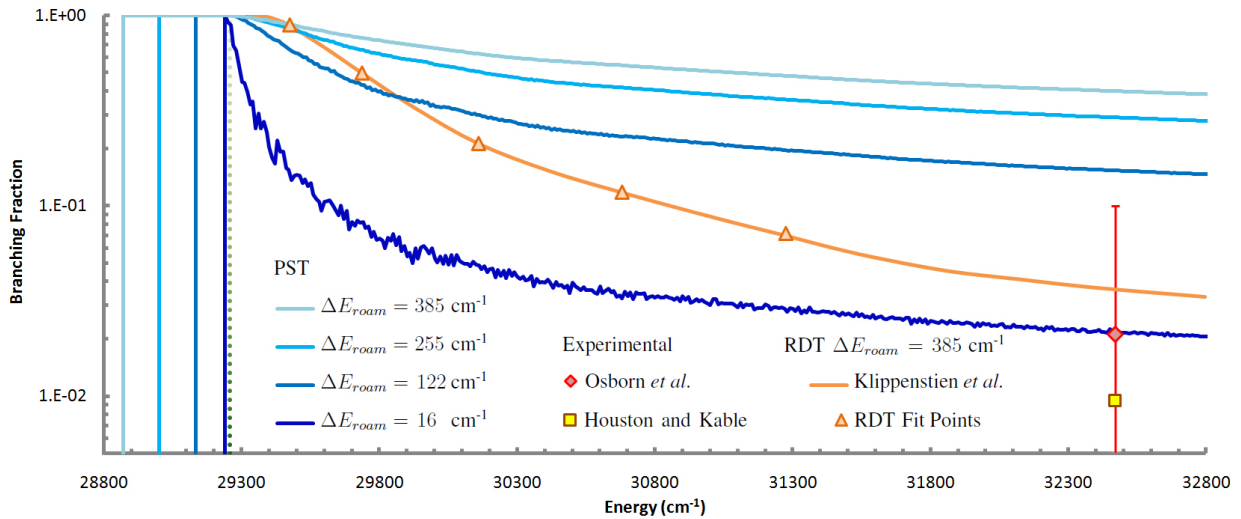


FIGURE 2.9: For  $\text{CH}_3\text{CHO}$ , In blue, modelled radical and roaming fractions in the range ( $E_{\text{tot}} = 28800 - 32800 \text{ cm}^{-1}$ ). The two darker blue lines are where the single parameter  $\Delta E_{\text{roam}}$  has been varied to fit the experimental or RDT data. The two lighter blue lines are results where  $\Delta E_{\text{roam}}$  has been set to a physically reasonable value. The RDT data [7] is shown in orange and the experimental data is shown in red [4] and yellow [8]. The radical threshold is indicated as a green dotted line.

the roaming TS of Harding *et al.* [7, 23] In this case the RMSEs are  $0.38 \text{ cm}^{-1}$  with respect to experiment and  $0.36 \text{ cm}^{-1}$  with respect to the five RDT fit points.

As expected the sum of states is significantly greater for  $\text{CH}_3\text{CHO}$  than for  $\text{H}_2\text{CO}$ .  $\text{CH}_3\text{CHO}$  has more degrees of freedom. Once the radical channel is open, the roaming fraction diminishes more slowly for  $\text{CH}_3\text{CHO}$  compared with  $\text{H}_2\text{CO}$ . More degrees of freedom means more ways to trap energy in modes other than the reaction coordinate, thus more frustrated dissociations. More degrees of freedom and smaller rotational constants also mean that structure reflecting the density of states, such as observed in figure 2.6 for  $\text{H}_2\text{CO}$ , is finer and not visible in figure 2.9, except for the  $\Delta E_{\text{roam}} = 16 \text{ cm}^{-1}$  result, where  $\Delta E_{\text{roam}}$  is smaller than the  $\vec{A}$  for  $\text{HCO}$  ( $24.329602 \text{ cm}^{-1}$ ). [58]

There is poor agreement between our PST model and RDT results for all four  $\Delta E_{\text{roam}}$  values; the errors in the fit are large. Compared with the RDT results: [7] with  $\Delta E_{\text{roam}} = 16$  the PST model predicts a much lower roaming fraction with a faster decay as energy increases; with  $\Delta E_{\text{roam}} = 385 \text{ cm}^{-1}$  the PST model predicts a much higher roaming fraction with a slower

decay as energy increases. A single parameter fit to the RDT data significantly improves the fit, however despite the improved fit to the RDT data with  $\Delta E_{roam} = 122 \text{ cm}^{-1}$ , at all but the lowest energies the PST model overestimates the roaming fraction and the decay in the roaming fraction with increasing energy is too slow. The discrepancy at low energies is attributed to the lower  $\Delta E_{roam}$  used in the PST model fit.

## 2.8 The Roaming Probability Parameter $P_{roam}$

When  $\Delta E_{roam} = 385 \text{ cm}^{-1}$  is used to model CH<sub>3</sub>CHO, our PST model always overestimates roaming compared to the RDT and experimental results. We expect an overestimation due to our assumption that all roaming states roam, with no reformation of reactants. Both Klippenstein *et al.* and Bowman *et al.* identify many potential roaming trajectories that return to reactants. [7,36] Therefore, an additional probability ( $P_{roam}$ ) that fragments satisfying inequality 2.2 will roam, rather than re-forming reactants should be included in our model. A low  $P_{roam}$  for CH<sub>3</sub>CHO should allow our model to match the experimental data point with a physically reasonable  $\Delta E_{roam}$  value and improve our agreement with the RDT prediction. In H<sub>2</sub>CO, the roaming fragment (H<sup>•</sup>) has no rotational or vibrational degrees of freedom, so we expect  $P_{roam}$  should be high. However, just as the larger number of degrees of freedom provide more ways for CH<sub>3</sub>CHO radical dissociation to be frustrated, compared with H<sub>2</sub>CO, so too do extra degrees of freedom in the roaming <sup>•</sup>CH<sub>3</sub> fragment provide more ways for roaming states to undergo processes other than roaming. The obvious alternative to roaming, reforming reactants, may not be the only process explored by the frustrated radical dissociations we describe here as roaming states. Moreover, a more complete treatment should additionally consider all the reaction pathways described in more detail in chapter 3. We expect, however, that the inclusion of the additional isomerism and dissociation channels, as discussed in chapter 3, would have a minuscule affect on the result.

When reactants are re-formed, ergodicity is restored, allowing energy to be randomised amongst all internal degrees of freedom. Therefore some re-formed reactants will follow the tight TS channel (1) to molecular products, and, when  $E_A \geq E_{tmin}$ , re-formed reactants may also form

radical products rather than roaming. Thus  $P_{roam} < 1$ . Our single parameter ( $\Delta E_{roam}$ ) fits implicitly assume  $P_{roam} = 1$ . It is tempting to speculate that a physical rationale that considers more than just the energy in the reaction coordinate can be elucidated for establishing which states will roam. However in this flat PES region there are many large amplitude modes that do not behave in an easily predictable way. Thus attempting to develop such a rationale is beyond the scope of this project. However, we expect some degree of energy dependence in  $P_{roam}$  would be revealed if this were achieved.

Here we model  $P_{roam}$  using a Master equation that describes the time evolution of the concentrations of roaming states ( $R^{\cdot\dots\cdot}CHO$ ), reactants (RCHO), molecular products formed via channel (1) (RH + CO), molecular products formed via roaming ( $RH^{\ddagger} + CO$ ) and radical products ( $R^{\cdot} + H^{\cdot}CO$ ). the Master equation is a gain-loss equation for the probability of each state, given by

$$\frac{dP_i}{dt} = \sum_j T_{ij}P_j \quad (2.21)$$

where  $i$  and  $j$  both index, respectively, the five states listed above, the vector  $\vec{P}$  contains the concentrations of those states and the matrix  $\underline{T}$  contains rates for the reactions  $i \rightarrow j$ . That is

$$\vec{P} = \begin{pmatrix} [R^{\cdot\dots\cdot}CHO] \\ [RCHO] \\ [RH + CO] \\ [RH^{\ddagger} + CO] \\ [R^{\cdot} + H^{\cdot}CO] \end{pmatrix} \quad (2.22)$$

where at  $t = 0$   $[R^{\cdot\dots\cdot}CHO] = 100\%$  and all other concentrations are 0 and  $\underline{T}$  is given by

$$\begin{array}{ccccc} & R^{\cdot\dots\cdot}CHO & RCHO & RH + CO & RH^{\ddagger} + CO & R^{\cdot} + H^{\cdot}CO \\ \begin{matrix} R^{\cdot\dots\cdot}CHO \\ RCHO \\ RH + CO \\ RH^{\ddagger} + CO \\ R^{\cdot} + H^{\cdot}CO \end{matrix} & \left( \begin{array}{ccccc} 0 & k_{-RS} & 0 & k_{roam} & 0 \\ k_{RS} & 0 & k_{TS} & 0 & k_{rad} \\ 0 & 0 & 0 & 0 & 0 \\ 0 & 0 & 0 & 0 & 0 \\ 0 & 0 & 0 & 0 & 0 \end{array} \right) & & & & (2.23) \end{array}$$

where  $k_{RS}$  is the rate for  $\text{RCHO} \rightarrow \text{R}^\bullet \cdots \cdot\text{CHO}$ , where  $\text{R}^\bullet \cdots \cdot\text{CHO}$  is the van der Waals roaming state intermediate,  $k_{-RS}$  is the rate for  $\text{R}^\bullet \cdots \cdot\text{CHO} \rightarrow \text{RCHO}$ ,  $k_{roam}$  is the rate for  $\text{R}^\bullet \cdots \cdot\text{CHO} \rightarrow \text{RH}^\ddagger + \text{CO}$  and  $k_{TS}$  and  $k_{rad}$  are rates for channels (1) and (2) respectively.

Accurate variable reaction coordinate TST values for  $k_{TS}$  and  $k_{rad}$  are obtained from Klippenstien *et al.* [55]  $k_{RS}$  is approximated by scaling  $\omega_{roam}$  and  $\omega_{rad}$  by a common factor such that  $\omega_{rad}$  matches  $k_{rad}$ . To ensure our Master equation exhibits detailed balance, we assert

$$k_{RS} = k_{-RS} + k_{roam} \quad (2.24)$$

Thus  $k_{-RS}$  and  $k_{roam}$  can be obtained from  $P_{roam}$  as

$$k_{roam} = P_{roam} \times k_{RS} \quad (2.25)$$

and

$$k_{-RS} = (1 - P_{roam}) \times k_{RS} \quad (2.26)$$

The converged values for  $[\text{RH} + \text{CO}]$ ,  $[\text{RH}^\ddagger + \text{CO}]$  and  $[\text{R}^\bullet + \text{H}^\bullet\text{CO}]$  are then used to obtain corrected values for  $\omega_{roam}$  and  $\omega_{rad}$  as

$$\omega_{roam} = \frac{[\text{RH}^\ddagger + \text{CO}]}{[\text{RH}^\ddagger + \text{CO}] + [\text{RH} + \text{CO}] + [\text{R}^\bullet + \text{H}^\bullet\text{CO}]} \times \omega_{roam} \quad (2.27)$$

and

$$\omega_{rad} = \frac{[\text{R}^\bullet + \text{H}^\bullet\text{CO}]}{[\text{RH}^\ddagger + \text{CO}] + [\text{RH} + \text{CO}] + [\text{R}^\bullet + \text{H}^\bullet\text{CO}]} \times \omega_{roam} + \omega_{rad} \quad (2.28)$$

Figure 2.10 shows two single parameter fits where  $\Delta E_{roam}$  is held constant at  $255 \text{ cm}^{-1}$  and  $P_{roam}$  is varied, as a constant with respect to  $E_{tot}$ , to find the best fit to either: the experimental  $\text{CH}_3\text{CHO}$  roaming data point of Osborn *et al.*, yielding  $P_{roam} = 5.3\%$ ; or the five RDT points shown in 2.9, yielding  $P_{roam} = 26\%$ . Our model can match the experimental value exactly with  $P_{roam} = 5.3\%$ . However, while the agreement with the RDT results is dramatically improved compared to our results when  $\Delta E_{roam} = 255 \text{ cm}^{-1}$  and  $P_{roam} = 100\%$ , our modelled roaming fraction still decays much faster than the RDT prediction when we fit the experimental data point. When we fit  $P_{roam}$  to the RDT results the agreement is predictably further improved, however, as with the  $\Delta E_{roam}$  fit to the RDT results, our PST model underestimates roaming

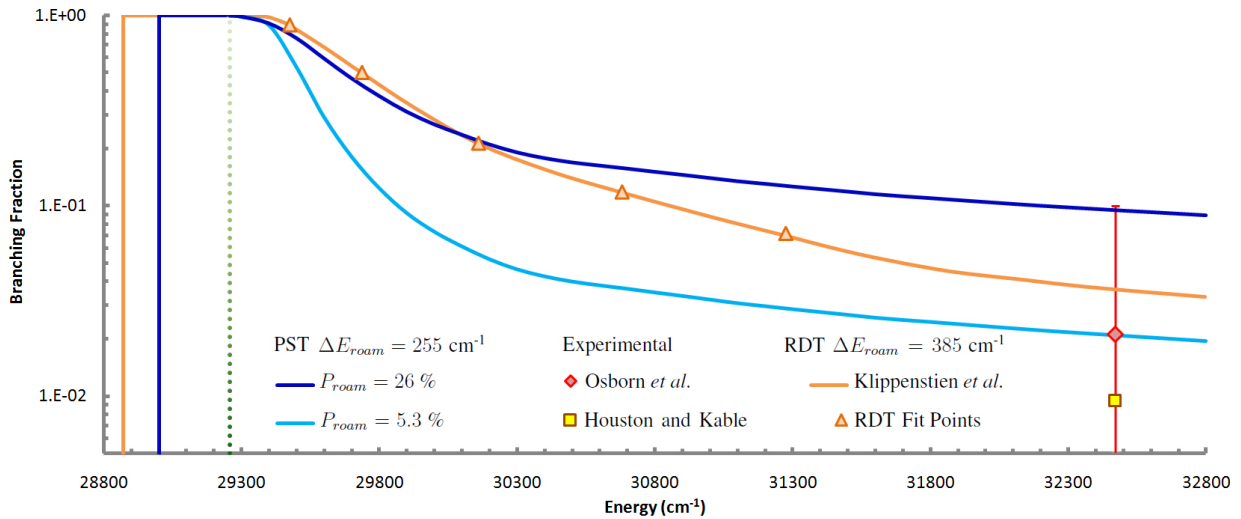


FIGURE 2.10: For CH<sub>3</sub>CHO, In blue, modelled radical and roaming fractions in the range ( $E_{tot} = 28800 - 32800 \text{ cm}^{-1}$ ) where  $\Delta E_{roam}$  is held constant at 255  $\text{cm}^{-1}$ . The light blue line is where the single parameter  $P_{roam}$  has been varied to fit the experimental data point and the dark blue line is where the single parameter  $P_{roam}$  has been varied to fit RDT data. The RDT data [7] is shown in orange and the experimental data is shown in red [4] and yellow [8]. The radical threshold is indicated as a green dotted line.

at low energies and overestimates roaming at higher energies. However with  $P_{roam} = 26\%$  our PST model predicts 9.5% roaming at the experimental energy ( $32470 \text{ cm}^{-1}$ ), which just fits within the 10% estimated uncertainty in the experimental data point.

## 2.9 Predictive Results For formaldehyde-*d*<sub>2</sub>

Figure 2.11 show predictions for formaldehyde-*d*<sub>2</sub>, assuming  $\Delta E_{roam}$  and  $P_{roam}$  have the same values as formaldehyde-*h*<sub>2</sub> (161  $\text{cm}^{-1}$  and 100%). If this assumption is correct, any deviations between the H<sub>2</sub>CO and D<sub>2</sub>CO predictions can be ascribed to the kinetic isotope effect. Figure 2.12 compares the H<sub>2</sub>CO and D<sub>2</sub>CO PST model results. The only significant difference between the H<sub>2</sub>CO and D<sub>2</sub>CO predictions is that at 31860 and 32840  $\text{cm}^{-1}$ , where the 2<sub>1</sub> and 3<sub>1</sub> vibrational levels, respectively, become accessible to roaming states in D<sub>2</sub>CO, the roaming fraction is higher for D<sub>2</sub>CO compared with H<sub>2</sub>CO. At slightly higher energies (31840 and 32820  $\text{cm}^{-1}$ ) these H<sub>2</sub>CO vibrational energies become available to H<sub>2</sub>CO roaming states and the reverse is true, however the difference is much smaller. Overall, our model predicts a very

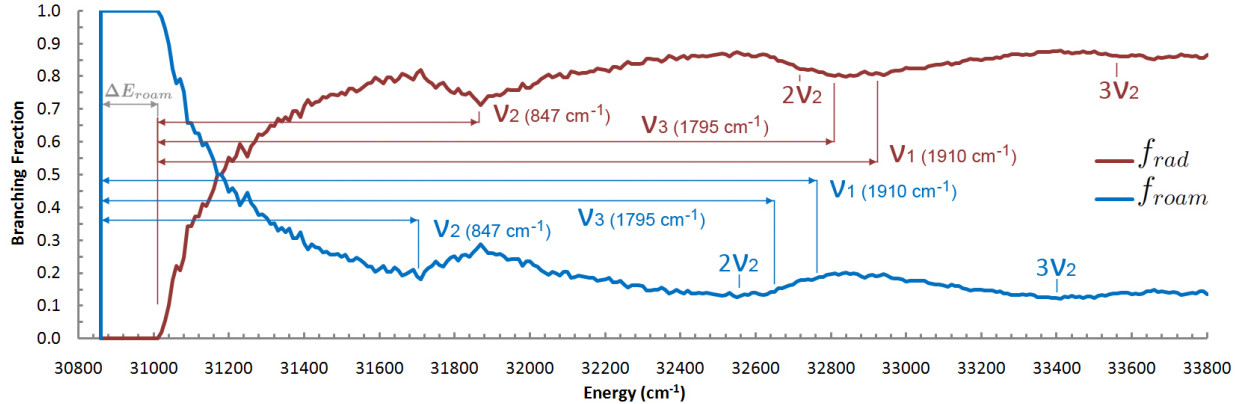


FIGURE 2.11: For D<sub>2</sub>CO, In red and dark blue, the radical and roaming fractions in the range ( $E_{tot} = 30800 - 33800 \text{ cm}^{-1}$ ) where  $\Delta E_{roam} = 161 \text{ cm}^{-1}$  and  $P_{roam} = 1$ .

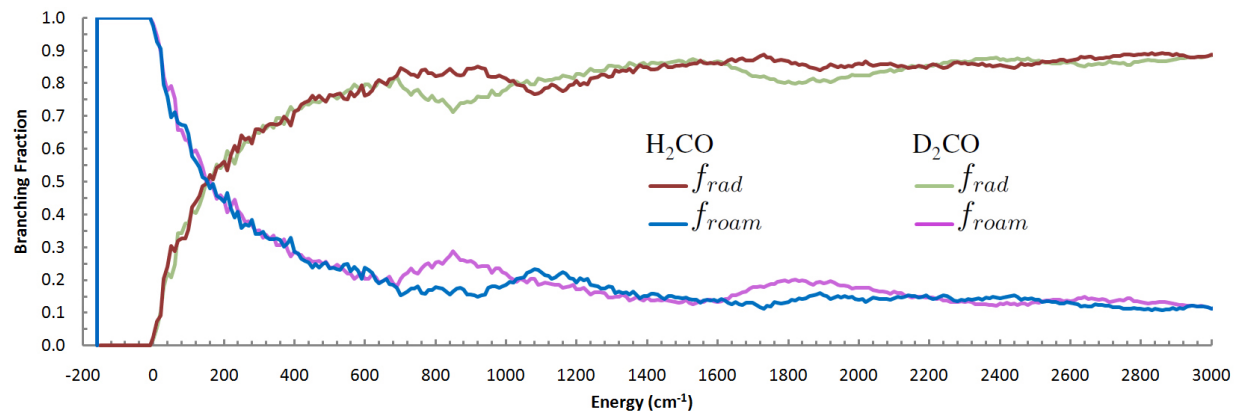


FIGURE 2.12: Comparison of the modelled H<sub>2</sub>CO and D<sub>2</sub>CO branching fractions, from figures 2.6 and 2.11, with the energy relative to their respective radical dissociation thresholds.

similar roaming fraction, suggesting that the kinetic isotope effect has little affect on roaming. However the threshold energies for channels (1) and (2) will be affected by the kinetic isotope effect and are likely to be shifted by different amounts. Because the density of states is much higher for channels (3) and (2) than for channel (1), this result implies that there may be an observable difference in  $f_{RTS}$  due to the kinetic isotope effect. However imaging experiments have observed  $\sim 15\%$ roaming for D<sub>2</sub>CO which is similar to the 18%observed in H<sub>2</sub>CO at a comparable energy, although background interference limited the range of rotational levels that could be experimentally probed for D<sub>2</sub>CO. [59]

TABLE 2.4:  $\Delta E_{cross}$  and  $\omega_{tot}(E_{cross})$  for  $\text{H}_2\text{CO}$ ,  $\text{CH}_3\text{CHO}$  and the Norrish I channels of propanal and *n*-butanal where  $\Delta E_{roam} = 178 \text{ cm}^{-1}$ .

Species	$E_{RT} (\text{cm}^{-1})$	$E_{cross} (\text{cm}^{-1})$	$\Delta E_{cross} (\text{cm}^{-1})$	$\omega_{tot}(E_{cross})$
$\text{H}_2\text{CO}$	30320	30500	180	$5.56 \times 10^2$
$\text{CH}_3\text{CHO}$	29320	29850	530	$4.93 \times 10^5$
$\text{C}_2\text{H}_5\text{CHO}$	29320	30130	810	$4.43 \times 10^7$
$\text{C}_3\text{H}_7\text{CHO}$	28650	29840	1190	$2.72 \times 10^9$

## 2.10 General Trends Observed

In order to observe the affects of increasing molecule size, without the complications imposed by changing  $\Delta E_{roam}$ , simulations for  $\text{H}_2\text{CO}$ ,  $\text{CH}_3\text{CHO}$ , propanal and *n*-butanal were run with a fixed  $\Delta E_{roam} = 178 \text{ cm}^{-1}$ , which was obtained in an early  $\text{H}_2\text{CO}$  fit where both  $\Delta E_{roam}$  and  $P_{roam}$  were varied, but, for this purpose should be considered arbitrary. There are several dissociation channels for propanal and *n*-butanal and we restrict our analysis to the Norrish I channels, which are analogous to channel (2). The same trends observed for the increased degrees of freedom of  $\text{CH}_3\text{CHO}$  (relative to  $\text{H}_2\text{CO}$ ), are observed for propanal (relative to  $\text{CH}_3\text{CHO}$ ) and for *n*-butanal (relative to propanal). That is, the roaming fraction dies off more slowly and the sum of states is larger still, as the molecule size increases. We define a metric ( $\Delta E_{cross}$ ) to describe the energy difference between the radical channel threshold ( $E_{RT}$ ) and the energy where  $f_{rad}$  and  $f_{roam}$ , and thus  $\omega_{roam}$  and  $\omega_{rad}$ , are equal. We find that  $\Delta E_{cross}$  is directly proportional to molecule size, see table 2.4. It is clear that as the parent molecule size increases there are even more degrees of freedom in the roaming fragments. Therefore, there are even more ways that roaming states can undergo processes other than roaming and we speculate that  $P_{roam}$  will be even smaller for larger systems than it is for  $\text{CH}_3\text{CHO}$ .

The *general* trends observed using our PST model are consistent with DC slice images and PHOFEX spectra obtained for  $\text{H}_2\text{CO}$  in the range ( $30000 - 35400 \text{ cm}^{-1}$ ) and the RDT calculations of Klippenstien *et al.* for  $\text{CH}_3\text{CHO}$ . [6, 7] Figures 2.7 shows the radical channel dominating as energy increases, while the roaming channel flux increases relatively slowly. This compares well with figure 2.4. Figures 2.6 and 2.11 plot radical and roaming branching fractions, and in both cases, show that the roaming channel opens before the radical channel and

persists at high energies, (compare with figure 2.4). The insets to figure 2.7 show the roaming channel opening below the radical threshold, and compare with figure 2.5, which shows a similar trend is predicted for CH<sub>3</sub>CHO by the RDT calculations of Klippenstien *et al.* [7]

## 2.11 PST Model Summary

The model presented here is intended to provide a rough estimate of roaming fractions that is simple to implement and transferable. As such, it should be noted that the accuracy of its predictions are limited by certain factors. For example PST assumes that the roaming fragments are free rotors, however, in the van der Waals region the roaming fragments are hindered rotors. Furthermore we do not account for the energy consumed by orbital angular momentum in the van der Waals region. This model is not intended to compete with other treatments that rely heavily on *ab initio* calculations and are likely to provide more accurate predictions. This model is designed to provide a quick estimate without the vast computational expense required by the previous QCT and RDT treatments. [7, 36, 42]

We are yet to establish a physical rationale for predicting  $P_{roam}$ , however we can predict  $\Delta E_{roam}$  using LJ potentials. If we can establish a rationale for predicting  $P_{roam}$ , our model can become predictive. We have shown that our model can match all experimental roaming data for H<sub>2</sub>CO by varying the single parameter  $\Delta E_{roam}$ , while obtaining a  $\Delta E_{roam}$  value that agrees with the experimental roaming threshold within its uncertainty. We have shown that using a  $\Delta E_{roam}$  predicted using the LJ potential, our model can match the CH<sub>3</sub>CHO experimental data, and the RDT predictions of Klippenstein *et al.*, by varying the single parameter  $P_{roam}$ . This is the first statistical model for roaming that does not require a PES, making it easily transferable. Our results suggest that the basic premise of our model, that roaming results from frustrated radical dissociation, is plausible.

## CHAPTER 3

### H/D Exchange Experiments

---

#### 3.1 Overview

Our initial experimental aims were to characterise the radical dissociation channels of deuterated acetaldehyde isotopologues, in preparation for experiments designed to observe the kinetic isotope effect on roaming. However, some unusual results in our spectra caused the direction of our research to shift, to verify and explain our observations. The initial observations were obtained for acetaldehyde- $2,2,2-d_3$  ( $CD_3CHO$ ), by Heazlewood *et al.* [60] In this honours year, we have expanded on the initial  $CD_3CHO$  work and performed new experiments on acetaldehyde- $1-d_1$  ( $CH_3CDO$ ). In the interest of clarity, only the  $CH_3CDO$  results will be presented in this thesis.

Isotopic labelling of chemical compounds is one of the most powerful techniques for the elucidation of molecular structure and chemical reactivity. Stable isotope marking, especially  $^{13}C/^{12}C$  and D/H ( $D = ^2H$ ), is a versatile analytical tool across many realms of science. Since the discovery of “a hydrogen isotope of mass 2” [61], the ability to distinguish between H and D has led to a wide diversity of important discoveries, spanning the astronomical scale where H/D abundance is an important parameter of the astrophysical environment [62, 63]; the global scale, where paleoclimate and temperature can be reconstructed [64]; the biological scale where H/D abundance elucidates bacterial pathways [65]; and the molecular scale, where chemical mechanisms can be determined by specific H/D labelling. [66, 67]

Uncontrolled scrambling of isotopes complicates the interpretation of isotope-labelled experiments. In the condensed phase, isotope exchange is interpreted as a bimolecular process with

exchange mediated by solute-solvent processes. In the gas phase, H/D exchange has long been known in mass spectrometry, where, at energies far exceeding the CH or OH binding energy, charged intermediates undergo facile hydrogen scrambling before fragmenting into daughter ions. [68, 69]

Experiments on the photodissociation of isolated molecules provide the cleanest probe of reaction dynamics because of the very fine control of reaction energy and sensitive detection of the product state distributions. As the photon energy approaches the threshold for one or more reaction pathways the delicate interplay between the different processes can be revealed and new, unsuspected mechanisms discovered. For example, experiments on the near-threshold photodissociation of formaldehyde [14] and acetaldehyde [8], coupled with extensive theoretical simulations, revealed the presence of roaming.

There have been few photodissociation experiments that have probed H/D exchange. Previous experiments were typically conducted at 193 and 157 nm, which correspond to a photon energy of 51800 and 63700 cm<sup>-1</sup> respectively. [70–76] This is far in excess of the threshold for H/D exchange, for example, the C–H bond dissociation energy in acetaldehyde is 30715 cm<sup>-1</sup> [77] and the C–C bond dissociation energy is 29258 cm<sup>-1</sup>. [8] In this work we reduce the photon energy near, and then below, threshold (30340 – 32000 cm<sup>-1</sup>) for C–H and C–D bond cleavage, and probe the reaction dynamics of the lowest energy pathways in the photodissociation of CH<sub>3</sub>CDO. The expected photochemical products of this reaction, based on an extensive literature investigation of CH<sub>3</sub>CHO photolysis, were identified as •CH<sub>3</sub> + D•CO, CH<sub>3</sub>D + CO and perhaps a small yield of CH<sub>3</sub>•CO + •D. [16, 30, 38, 78] Remarkably, our experiments show that 10–20% of the radical products have undergone H/D-exchange, yielding •CH<sub>2</sub>D + H•CO.

## 3.2 Laser Induced Fluorescence Experiments

Formyl photofragments from the CH<sub>3</sub>CDO acetaldehyde isotopologue were probed spectroscopically, using laser-induced fluorescence excitation (LIF) and photo-fragment excitation (PHOFEX) spectroscopy. Following supersonic expansion into a vacuum chamber, acetaldehyde parent molecules were excited by a photolysis laser in the cold central region of the

expansion, an environment essentially free of collisions. Radical formyl photofragments were subsequently probed by a second laser. Formyl fragment fluorescence spectra were recorded. The ratio of HCO and DCO fluorescence was analysed, providing information about the reaction dynamics and decay mechanisms of excited acetaldehyde. Specifically, the overall rate of isotope exchange that occurs in excited acetaldehyde preceding dissociation.

## The Vacuum Chamber

The cylindrical vacuum chamber employed in these experiments has been described previously. [79] Figure 3.1 shows a top-view schematic of this chamber. Attached to the eight circular ports around the chamber were: cylindrical baffled arms (400 mm in length) through which laser photons entered the chamber; a vacuum gauge (423 I-MAG cold cathode ionisation vacuum sensor, MKS instruments) to monitor chamber pressure; a monochromator (Spex Minimate 0.25 m) and photomultiplier tube (PMT) (EMI 9816-QB) to detect fluorescence; a vent valve; and viewing windows.

Acetaldehyde parent molecules, seeded in helium gas, were supersonically expanded into the vacuum chamber through a pulsed nozzle (General Valve Series 9, 0.8 mm orifice, driven by a Parker Instrumentation Iota One pulse driver). The nozzle was attached to an  $x, y, z$  translation stage on the top flange of the chamber. The chamber was evacuated by a diffusion pump (Varian VHS-6) backed by a rotary pump (Alcatel 2033). Operating pressures (with the nozzle pulsing) were typically in the range  $10^{-5}$  to  $10^{-4}$  mbar.

## Photolysis and Probe Laser Systems

Both experiments utilised two complementary dye laser systems as tunable, narrow bandwidth radiation sources. Both systems comprised a pump laser that excited the dye in a tunable dye laser. The photolysis laser was a frequency-doubled Nd:YAG (Quantel Brilliant B) pumped, frequency-doubled dye laser (Quantel TDL-90 with an intracavity beam expander, DCM dye in methanol, KDP crystal). Each frequency-doubled photolysis laser pulse provided  $\sim 2 - 4$  mJ of horizontally polarised photons, with a spectral line width of approximately  $0.08\text{ cm}^{-1}$ .

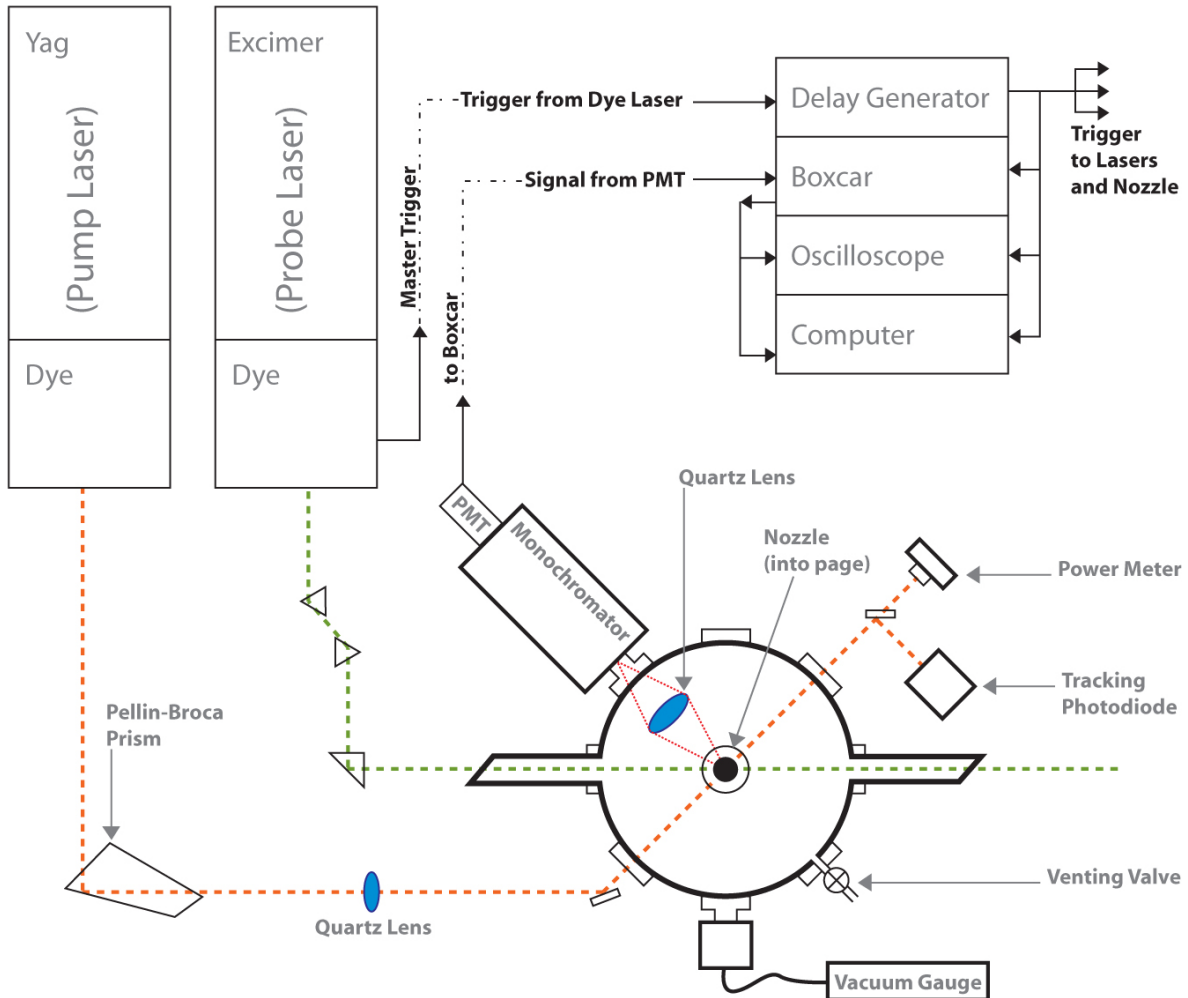


FIGURE 3.1: Top-view schematic of the vacuum chamber, indicating the orientation of the baffle arms, gauges and detection apparatus.

The probe laser was a XeCl excimer (Lambda Physik Lextra 200) pumped, frequency-doubled dye laser (Lambda Physik LPD 3000E, Coumarin 503 dye in methanol, BBO(I) crystal). Each probe laser pulse provided 0.1 – 1 mJ of horizontally polarised photons, with a spectral line width of approximately  $0.1 \text{ cm}^{-1}$ . A Coherent Wavemaster wavemeter was used for wavelength calibration. Laser power was monitored with a laser power meter (Coherent FieldMaxII-Top) and sensor (Coherent J25LP-1A).

The lasers were directed into the vacuum chamber via a series of  $90^\circ$  quartz turning prisms and dichroic filters. Any fundamental laser output in the frequency doubled output was removed

from the probe pulses using two  $60^\circ$  quartz prisms, from the pump pulses using a quartz Pellin-Broca prism and in both cases using dichroic filters. The photolysis and probe lasers intersected the molecular beam at a range of distances downstream from the nozzle orifice, depending on the experimental information desired. A digital delay/pulse generator (SRS DG535) triggered and controlled the delay between the probe laser, photolysis laser, nozzle, oscilloscope (Tektronix TDS 220), boxcar integrator (SRS SR 250) and personal computer (Pentium 4, 1.8 Ghz, 512 mb ram). All experiments ran at a repetition rate of 10 Hz.

## Fluorescence Detection

Each laser entered the chamber at  $45^\circ$  relative to each other, both intersecting the molecular beam at right angles in the centre of the vacuum chamber, where excited molecules fluoresced isotropically. A portion of this fluorescence was imaged onto the slits (5 mm) of a monochromator by a quartz lens. The monochromator selectively allows formyl fluorescence (290 – 300 nm, with a full width half maximum bandpass of  $\sim 15 - 20$  nm) to reach the PMT, excluding other wavelengths. These wavelengths provide an optimal compromise between maximising fluorescence signal detection and minimising noise arising from scattered laser photons and fluorescence from other species.

Fluorescence through the monochromator was imaged onto the PMT cathode. The fluorescence decay trace was observed using an oscilloscope connected to the PMT. The gated boxcar averager integrated the decay profile within the selected gate, typically 100 – 300 ns for each laser pulse. The signal, averaged over several laser shots, was transmitted to the PC via an analogue to digital (A/D) converter (SRS SR-245). Spectra were recorded as a function of laser wavelength using the SRS SR-272 V 1.5 software package.

## Sample Preparation

The acetaldehyde-*1-d*, sample ( $\text{CH}_3\text{CDO}$ , 98%) was synthesised in-house, in liquid form, using a method adapted from reference [80], by Mr Trent Conroy. [81] The  $\text{CH}_3\text{CDO}$  sample purity was confirmed using NMR spectroscopy. [82] Several millilitres of  $\text{CH}_3\text{CDO}$  were placed in a

stainless steel bubbler at a range of temperatures (typically  $\sim 15$  °C), achieved by immersing the bubbler in a salt-ice bath. Helium carrier gas (2 – 3 bar) was passed over the sample in the bubbler. The resultant gas mixture (typically  $\sim 10\%$  CH<sub>3</sub>CDO in helium) was injected into the vacuum chamber via the pulsed nozzle.

### 3.3 Spectroscopic Techniques

#### Laser Induced Fluorescence Excitation (LIF) Spectroscopy

Photons from the photolysis laser, fixed on selected acetaldehyde vibronic transitions in the spectral range 30500 – 32000 cm<sup>-1</sup>, promoted CH<sub>3</sub>CDO to  $S_1$  via an  $\pi^* \leftarrow n$  transition. [83] These energies are above the threshold for the  $S_0$  two-body radical dissociation channel (2). Most of these energies are below the  $T_1$  two-body radical dissociation (CH<sub>3</sub>CHO<sub>(T<sub>1</sub>)</sub> → ·CH<sub>3</sub> + H·CO) threshold ( $\sim 31400$  cm<sup>-1</sup>). [84] Consequently, internal conversion to highly vibrationally excited levels of  $S_0$ , and, at sufficiently high photolysis energies, intersystem crossing to  $T_1$ , lead to radical dissociation producing formyl fragments. The probe laser was scanned over the range 38550 – 38730 cm<sup>-1</sup>, probing the region of the  $\tilde{B} \leftarrow \tilde{X}$  transition of HCO and DCO, producing fluorescence which was monitored. [58]

#### Photo-Fragment Excitation (PHOFEX) Spectroscopy

PHOFEX is a form of action spectroscopy that is analogous to fluorescence excitation spectroscopy. A PHOFEX spectrum is essentially the same as LIF in approach, except that the production of photofragments is monitored as a function of photolysis wavelength, rather than fluorescence photons as a function of probe wavelength. PHOFEX spectra therefore identify which of the vibronic transitions of the parent molecule (CH<sub>3</sub>CDO) lead to the particular HCO or DCO rovibronic states being monitored. In this experiment the probe laser was fixed on a particular rovibronic transition of HCO (38711.7 cm<sup>-1</sup>) or DCO (38646.4 cm<sup>-1</sup>) and the fluorescence intensity was monitored while the photolysis laser was scanned in the spectral range 30340 – 32000 cm<sup>-1</sup>. Because the probe is fixed on a single spectral line, PHOFEX signal

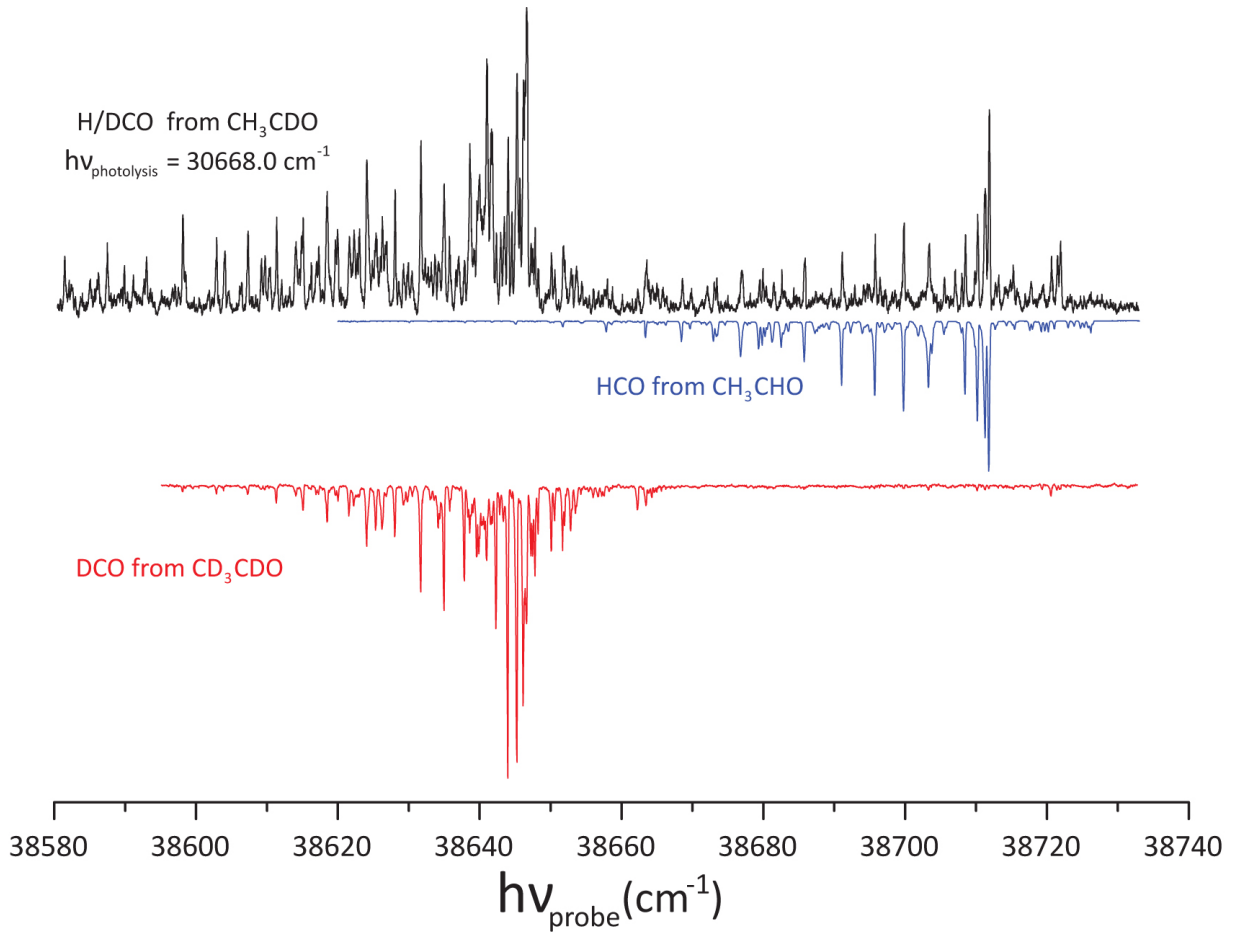


FIGURE 3.2: A comparison of LIF spectra probing formyl fragments produced via photolysis of  $\text{CH}_3\text{CHO}$ ,  $\text{CD}_3\text{CDO}$  and  $\text{CH}_3\text{CDO}$  parent molecules, where  $\text{CH}_3\text{CDO}$  has been pumped with an energy below the  $T_1$  radical threshold ( $30668.0 \text{ cm}^{-1}$ ).

intensity is dependant, not only on factors including the formyl fragment quantum yield and detection efficiency, but also, the relative population of the rovibronic states being monitored. We aim to compare HCO and DCO production as a function of photolysis energy, so we select probe wavelengths corresponding to the bandhead of the  $\tilde{B} \leftarrow \tilde{X}$  transition of HCO and DCO, [58] in order to maximise the probability that a significant number of the formyl fragments produced are in states that will be excited by the probe laser.

### 3.4 LIF Results

Figure 3.2 compares a laser induced fluorescence (LIF) spectrum of formyl fragments produced via photolysis of CH<sub>3</sub>CDO parent molecules, to analogous HCO and DCO LIF spectra from CH<sub>3</sub>CHO and CD<sub>3</sub>CDO parent molecules respectively. It is clear that the structure at energies below  $\sim 38670\text{ cm}^{-1}$  is DCO fluorescence and the structure at higher energies is HCO fluorescence. This CH<sub>3</sub>CDO LIF spectrum was recorded with a photolysis energy of 30668.0 cm<sup>-1</sup>, which is below the  $T_1$  radical threshold. The CH<sub>3</sub>CDO  $T_1$  radical threshold is expected to deviate only slightly from the CH<sub>3</sub>CHO  $T_1$  radical threshold ( $\sim 31400\text{ cm}^{-1}$  [84]) due to the change in ZPE. Once open, the  $T_1$  radical channel is a new competing channel that has increasing efficiency as photolysis energy rises and rapidly outcompetes the ground state pathways. [16] Indeed, at the photolysis energies used, radical dissociation is the only possible reaction on  $T_1$ , all other isomerisation and dissociation channels are closed. Therefore, we do not expect to see HCO formed at energies above the  $T_1$  threshold.

Figure 3.3 shows LIF spectra of formyl from CH<sub>3</sub>CDO parent molecules, at eleven distinct photolysis energies, both above and below the  $T_1$  radical dissociation threshold. These measurements compliment analogous CD<sub>3</sub>CHO LIF spectra that we recorded previously, see figure C.11 in appendix C. [60] There are two obvious differences between CH<sub>3</sub>CDO LIF spectra at energies above and below the  $T_1$  threshold; i) there is significantly more HCO fluorescence at the lower photolysis energies, and ii) the HCO perpendicular bands, observed above 31713 cm<sup>-1</sup>, are unusually intense in the lower energy LIF spectra. This unusual intensity suggests an anisotropic distribution of molecular orientation, although it is unclear why this occurs. A clear trend towards increased HCO fluorescence intensity at lower photolysis energies is observed and the absence of significant HCO production at energies above the  $T_1$  radical threshold confirms our NMR results for sample purity.

Since the integrated spectral line strengths of DCO and HCO are equivalent [?, 85], the branching ratio of formyl produced via H/D exchange isomerisation preceding photodissociation can be obtained as

$$f_{HCO} = \frac{A_{HCO}}{A_{HCO} + A_{DCO}} \quad (3.1)$$

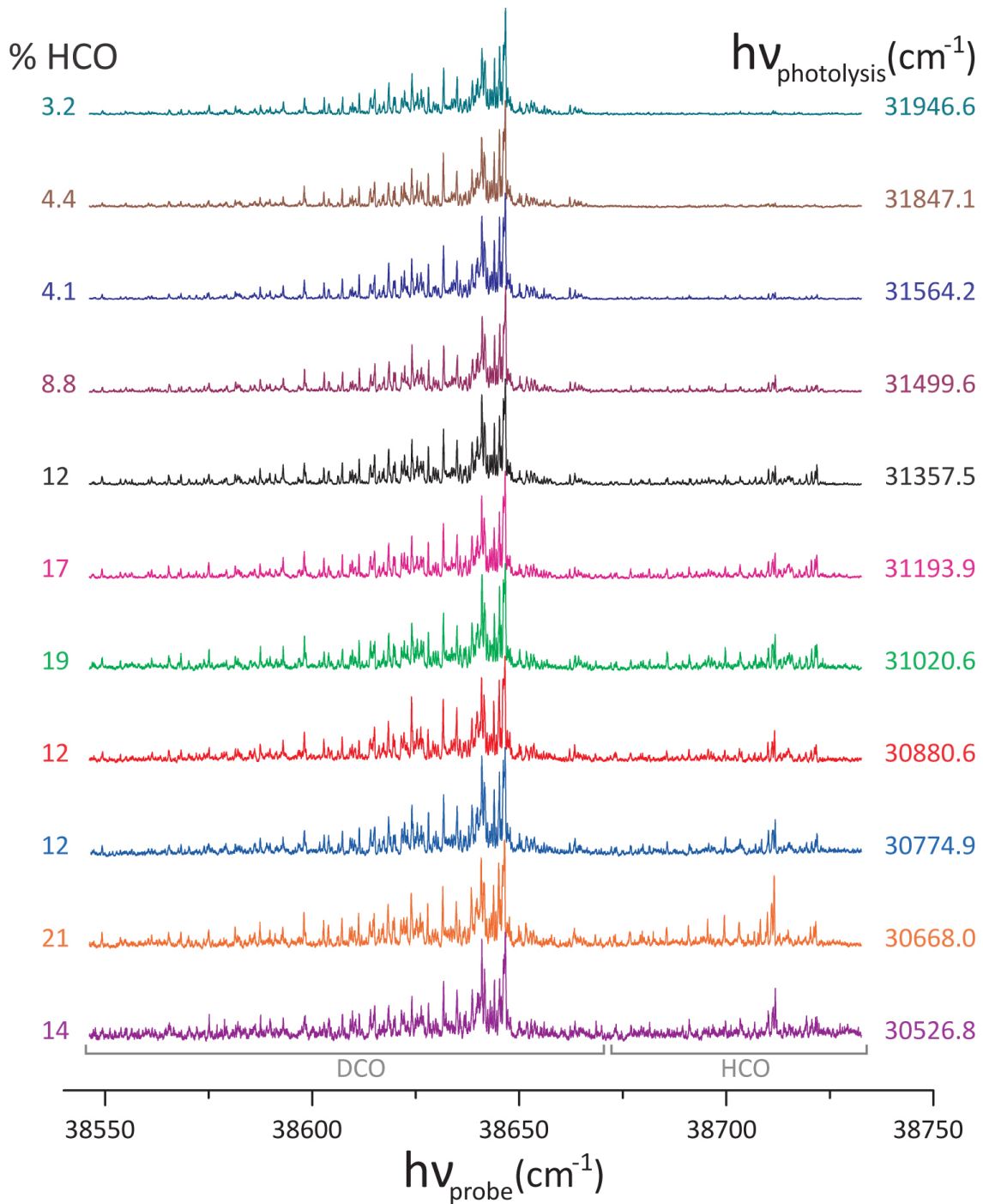


FIGURE 3.3: LIF spectra of formyl fragments produced via photolysis of  $\text{CH}_3\text{CDO}$  parent molecules, with various pump laser energies and the probe laser scanned in the range ( $\lambda = 258.2 - 259.4 \text{ nm}$ ). The t1 threshold is  $\sim 31400 \text{ cm}^{-1}$ .

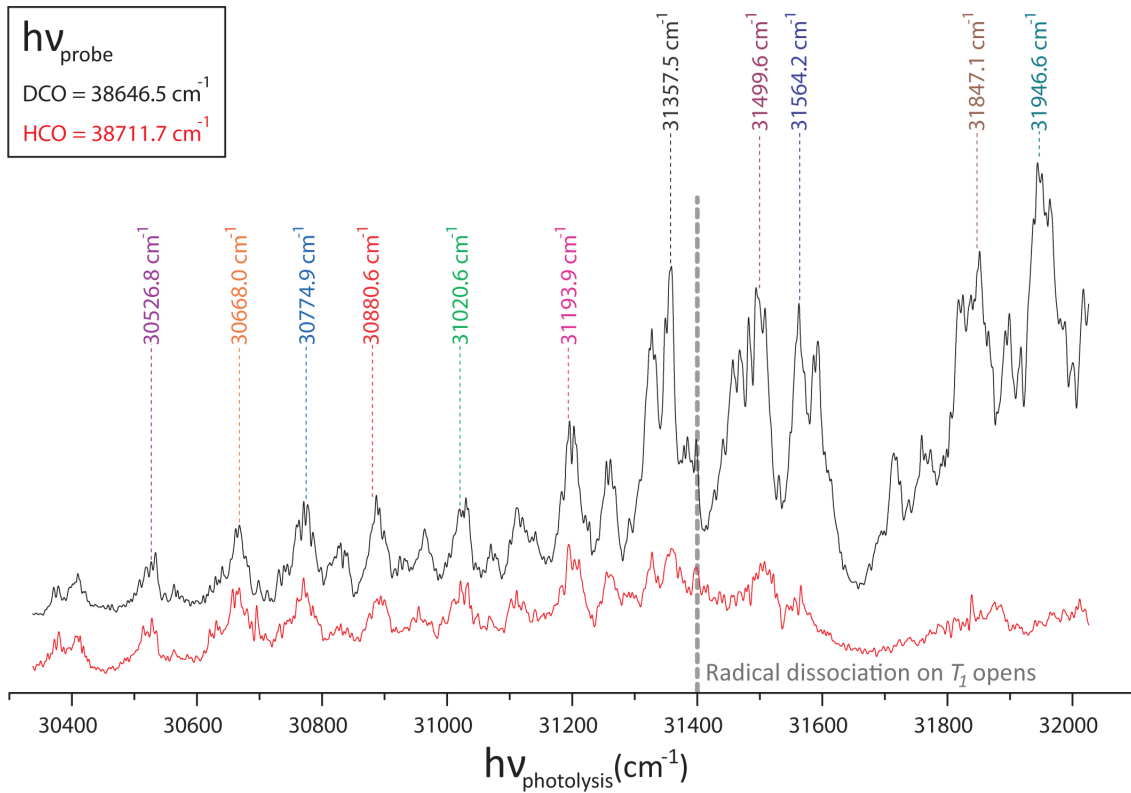


FIGURE 3.4: PHOFEX spectra of formyl fragments produced by photolysis of  $\text{CH}_3\text{CDO}$  parent molecules, with the pump laser scanned in the range ( $\lambda = 312.2 - 329.6 \text{ nm}$ ). In black, DCO probed at  $258.756 \text{ nm}$ , in red, HCO probed at  $258.320 \text{ nm}$ .

where  $A_{HCO}$  is the integrated area above  $\sim 38670 \text{ cm}^{-1}$ , corresponding to HCO fluorescence, and  $A_{DCO}$  is the integrated area at energies below  $\sim 38670 \text{ cm}^{-1}$  corresponding to DCO fluorescence. The results of this integration are displayed on the left hand side of figure 3.3.

## 3.5 PHOFEX Results

Figure 3.4 shows photofragment excitation (PHOFEX) spectra for  $\text{CH}_3\text{CDO}$  parent molecules, monitoring both DCO and HCO fragments. These spectra have been displaced vertically for clarity and the coloured energy labels in this figure correspond to the pump energies used to obtain the LIF spectra in figure 3.3. The structure in these spectra corresponds to vibronic energy levels in the  $\pi^* \leftarrow n$  system of  $\text{CH}_3\text{CDO}$ . [?, 83] It is clear in figure 3.4 that above the  $T_1$  threshold significantly more DCO is produced from the  $\text{CH}_3\text{CDO}$  parent molecule, while

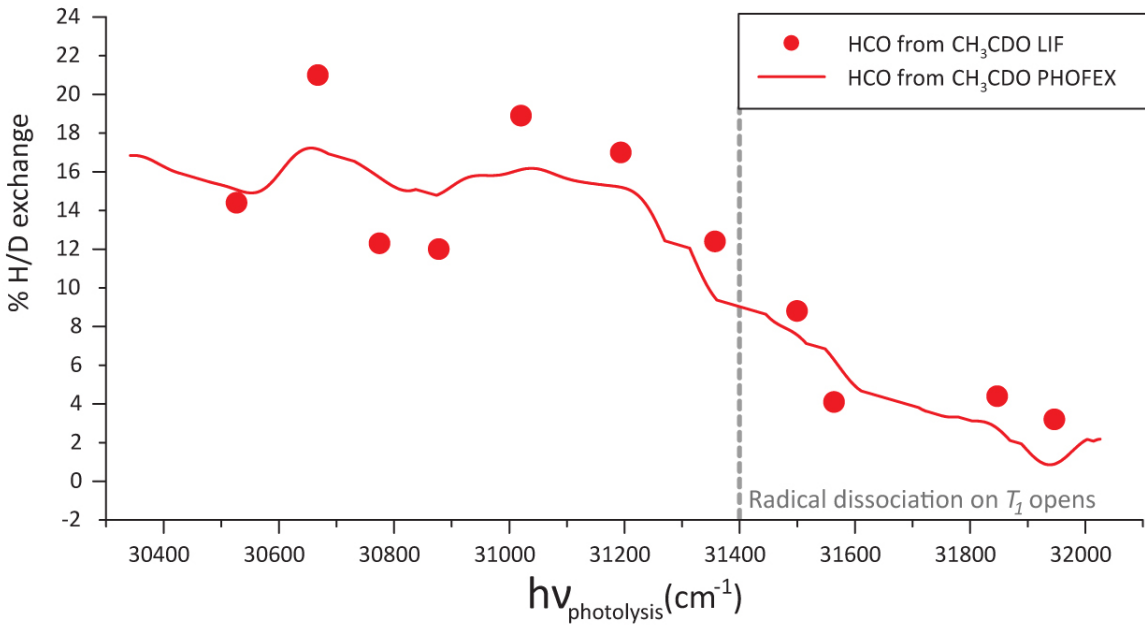


FIGURE 3.5: As a function of photolysis energy, % HCO from  $\text{CH}_3\text{CDO}$  photolysis calculated from integration of LIF spectra (red circles) and relative intensities of PHOFEX spectra (red line).

HCO production is significantly reduced. This is consistent with the LIF results in figure 3.3; isotope exchange leading to HCO production occurs on the  $S_0$  surface. It should be noted that in both PHOFEX spectra in figure 3.4 there is a systematic drop in signal strength in the spectral range  $31600 - 31800 \text{ cm}^{-1}$ , which is the result of an anomalous drop in pump laser doubling efficiency, and hence power, over this range.

The relative intensities of the PHOFEX spectra in figure 3.4 can be analysed to give qualitative trends for  $f_{\text{HCO}}$  and  $f_{\text{DCO}}$  as a function of photolysis energy. Quantitative values for  $f_{\text{HCO}}$  and  $f_{\text{DCO}}$  cannot be obtained because the absolute DCO and HCO fluorescence intensities plotted in figure 3.4 are arbitrary. The line strengths of the specific rovibrational states corresponding to the DCO and HCO spectral lines probed in these PHOFEX spectra are not equal because DCO and HCO have different rotational constants. Moreover, at any given photolysis energy, it is unlikely that these rovibrational states are equally populated. Therefore, the  $f_{\text{HCO}}$  and  $f_{\text{DCO}}$  trends obtained from the PHOFEX spectra must be scaled so they match the quantitative  $f_{\text{HCO}}$  and  $f_{\text{DCO}}$  values obtained from the integrated spectral intensities in the LIF spectra.

Figure 3.5 shows the relative intensities of PHOFEX spectra qualitatively fit to our LIF integration results. It should be noted that noise between the assigned PHOFEX peaks has been removed manually and the remaining data smoothed. There is good qualitative agreement between the LIF and PHOFEX results.

## 3.6 Analysis And Modelling

There are four known conventional pathways between  $\text{CH}_3\text{CDO}$  and  $\text{CH}_2\text{DCHO}$  that are available at these experimental energies. [86, 87] These are illustrated in figures 3.6, 3.7, 3.8 and 3.9. Figure 3.6 shows a two step ring closing and opening pathway via a cyclic ethylene oxide intermediate. Figures 3.7 and 3.8 show two three step pathways, both involving keto-enol tautomerisation between acetaldehyde and vinyl alcohol, a 1,2-hydrogen shift between vinyl alcohol and hydroxyethylidene, and a high energy rate determining transition state linking hydroxyethylidene and acetaldehyde directly. Figure 3.9 shows a four step process which also begins with keto-enol tautomerisation between acetaldehyde and vinyl alcohol and a 1,2-hydrogen shift between vinyl alcohol and hydroxyethylidene, but bypasses the high energy transition state by revisiting another vinyl alcohol isotopologue. There is an additional process for H/D exchange involving the  $\cdot\text{CH}_2\text{CH}_2\text{O}\cdot$  diradical, with possible intersystem crossing to the triplet diradical. [86] This diradical is difficult to observe experimentally due to its very short lifetime and this region of the PES is difficult to characterise theoretically because of its multi-configurational nature. This pathway has not been further considered because it has very high energy and does not significantly contribute to H/D exchange. The four conventional pathways, as well as all energetically accessible product channels, have been used in a kinetic model of H/D exchange in  $\text{CH}_3\text{CDO}$ .

### Rate Calculations

The best known literature energies for  $\text{C}_2\text{H}_4\text{O}$ , corresponding to the stationary points shown in figures 3.6, 3.7, 3.8, 3.9 and 3.10, were used as a starting point to modelling H/D exchange in  $\text{CH}_3\text{CDO}$ . [7, 77, 86–91] These energies comprised experimental and high level *ab initio* values

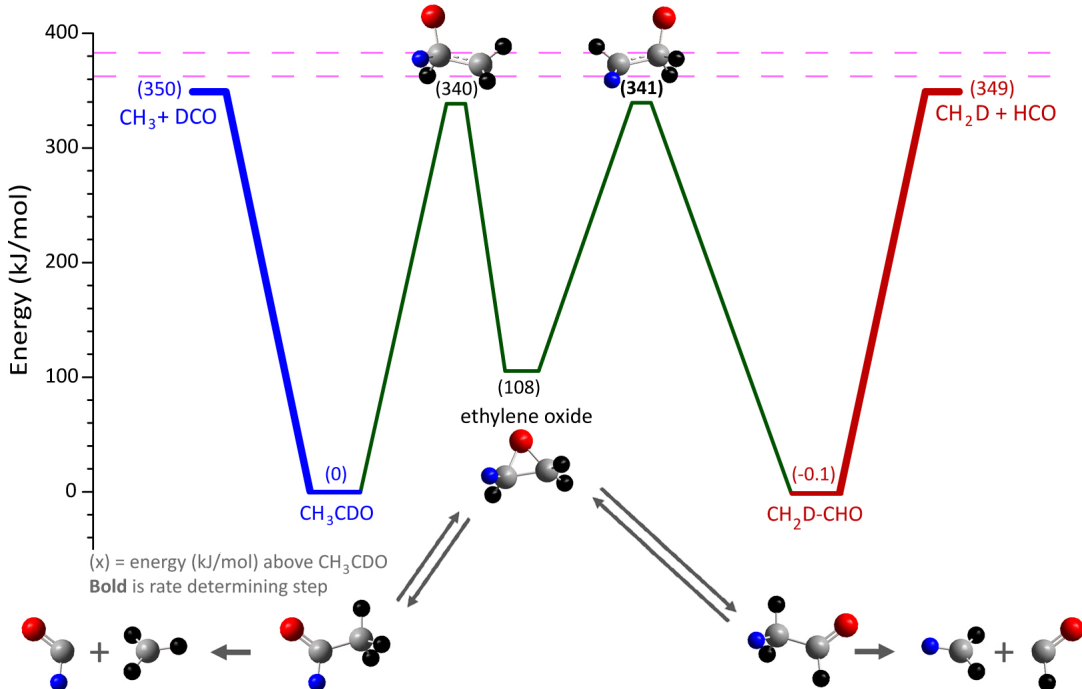


FIGURE 3.6: Two step isomerisation pathway between  $\text{CH}_3\text{CDO}$  and  $\text{CH}_2\text{DCHO}$ . Energies are ZPE corrected and based on the best available literature values for  $\text{CH}_3\text{CHO}$  as described in Appendix B.

and are tabulated... Utilising the MP2/6-311+G(d,p) electronic structure calculations of Ms Brianna Heazlewood, we calculated ZPE corrections and vibrational frequencies and rotational constants for each possible isotopologue. These data, tabulated in..., were used to calculate transition state theory (TST) and variational transition state theory (VTST) rate coefficients for the reactions shown in figure 3.10.

The UNIMOL suite of programs [92] was used to calculate microcanonical TST and VTST rate coefficients at  $10 \text{ cm}^{-1}$  increments over the experimental photolysis energy range ( $30310 - 32050 \text{ cm}^{-1}$ ). With the exception of the four radical dissociation pathways, the rate coefficients were obtained from TST as,

$$k_{TS}(E_{tot}) = \frac{\alpha \omega_{TS}(E_{tot} - E_{critical})}{h \rho_R(E_{tot})} \quad (3.2)$$

where  $\alpha$  is the reaction pathway degeneracy  $\omega_{TS}$  is the TS sum of states and  $\rho_R$  is the reactant density of states,  $h$  is Plank's constant and  $E_{critical}$  is the minimum energy required for reaction.

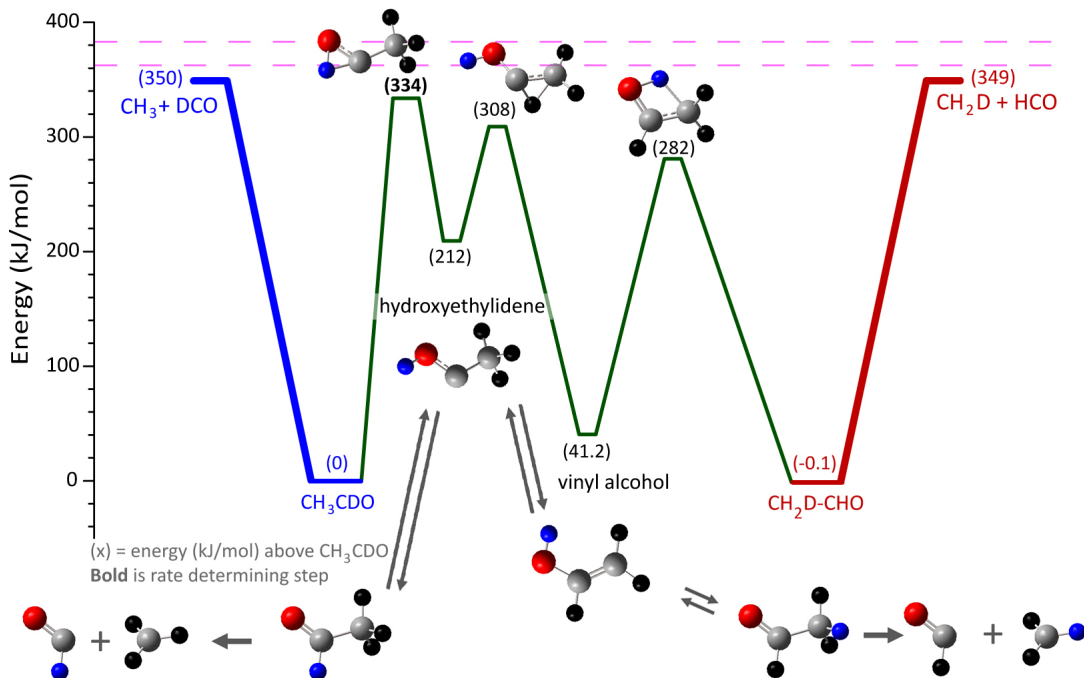


FIGURE 3.7: A three step isomerisation pathway between  $\text{CH}_3\text{CDO}$  and  $\text{CH}_2\text{D-CHO}$ . Energies are ZPE corrected and based on the best available literature values for  $\text{CH}_3\text{CHO}$  as described in Appendix B

[9] In other words,  $k_{TS}$  is roughly proportional to the number of accessible states at the TS at energy  $E_{tot}$ . [5]

VTST and the “loose” transition state model, first introduced by Gorin in 1938 [93], were used to calculate the rate coefficients for the radical dissociation channels ( $k_{rad}$ ), as a function of reaction coordinate, approximated as the length of the breaking bond. In the Gorin model it is assumed that the geometries and the vibrational frequencies of the fragments comprising the transition state are the same as those of the isolated product fragments. However the bending vibrations around the breaking bond in the reactant change drastically as the reaction proceeds. In the “loose” transition state model the two rocking motions are described as two-dimensional internal rotations that we simply assume to be unhindered until a hard-sphere interaction occurs. The torsional motion of the two fragments about the breaking bond is treated as a one dimensional free rotation.

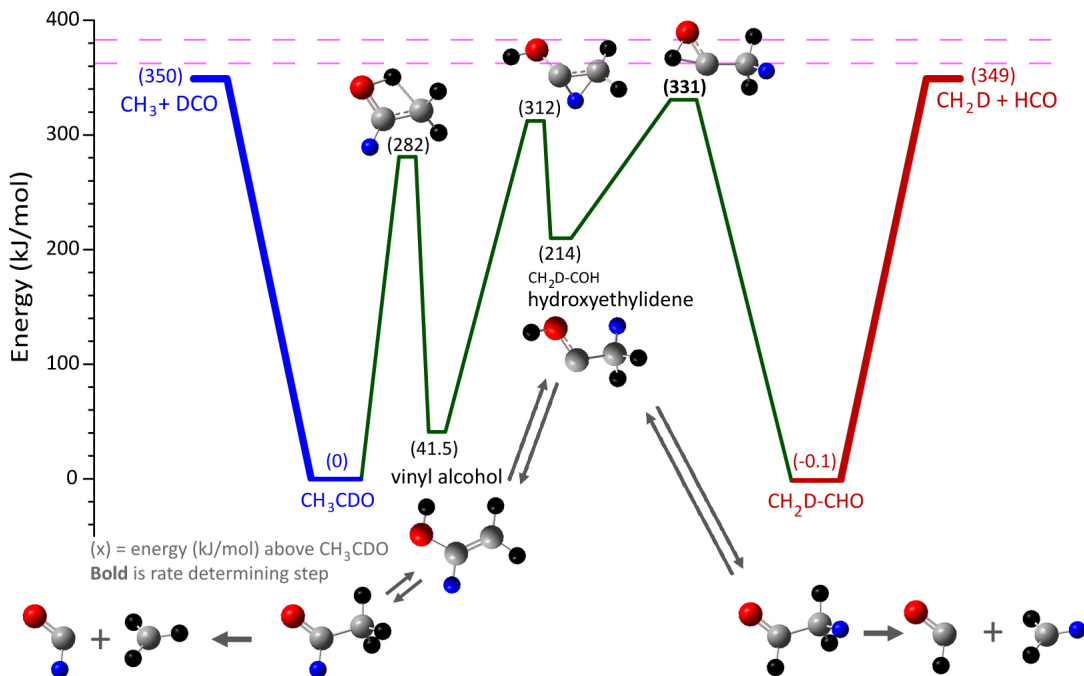


FIGURE 3.8: A three step isomerisation pathway between  $\text{CH}_3\text{CDO}$  and  $\text{CH}_2\text{DCHO}$ . Energies are ZPE corrected and based on the best available literature values for  $\text{CH}_3\text{CHO}$  as described in Appendix B

To improve the accuracy of our VTST radical channel rate coefficients, we wrote a *C++* version of the UNIMOL GEOM program that better accommodates fragments, such as formyl fragments, where the most unequal principal moment of inertia does not point along the reaction coordinate, see section E.1. However, this change makes only small differences in the rate coefficients produced (ie  $\sim 15\%$ ).

The UNIMOL suite [92] utilises standard harmonic oscillator and rigid rotor expressions, calculating the vibrational density of states using the Beyer-Swinehart algorithm. [9] We used an energy grain size of  $1 \text{ cm}^{-1}$ . This treatment is “standard” and does not conserve angular momentum, determining the rotational density of states as the inverse Laplace transform of the rotational partition function, which is calculated by integrating (rather than summing) over the angular momentum,  $\vec{J}$ . This can lead to an overestimation of the rotational density of states for both reactant and TS. The harmonic oscillator approximation, however, underestimates the true anharmonic vibrational density of states.

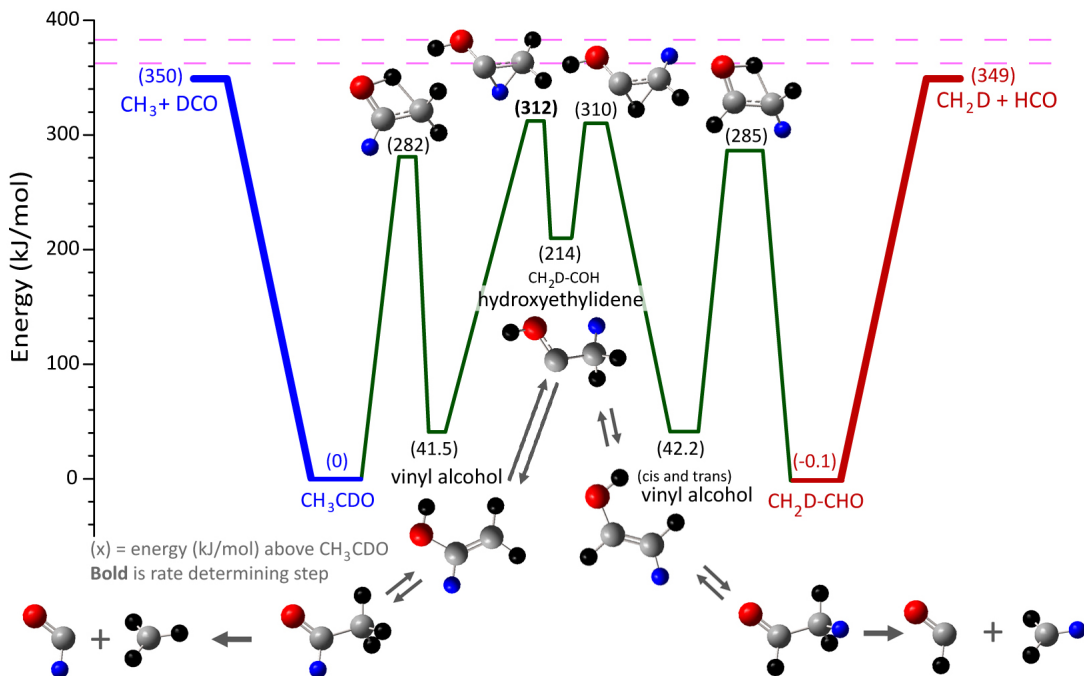


FIGURE 3.9: Four step isomerisation pathway between  $\text{CH}_3\text{CDO}$  and  $\text{CH}_2\text{DCHO}$ . Energies are ZPE corrected and based on the best available literature values for  $\text{CH}_3\text{CHO}$  as described in Appendix B

The “loose” transition state assumption can also introduce errors: the radical fragments are approximated as free rotors, rather than hindered rotors, and this can overestimate the density of states at the variational TS. Typically we expect microcanonical TST rate coefficients to be accurate to within a factor of 2. [94], VTST rate coefficients to be accurate to within an order of magnitude [95] and variable reaction coordinate TST (VRC-TST) rate coefficients to be accurate to within 15%. [13]

The calculated TST and VTST rate coefficients were compared to available literature values. [55, 86] This comparison told us that we were overestimating the rate coefficients for barrierless radical dissociation. Comparison with the VRC-TST rate coefficients of Dr Stephen Klippenstein [55], which are calculated using Monte Carlo Phase Space integration on an appropriate PES, incorporating  $\vec{J}$  conservation, anharmonicity and hindered rotation, revealed that our VTST rate coefficient for formation of methyl and formyl radicals was likely to be a significant overestimation, due to a lack of  $\vec{J}$  conservation and the inappropriate treatment of the fragments as free rotors. [11–13, 55]

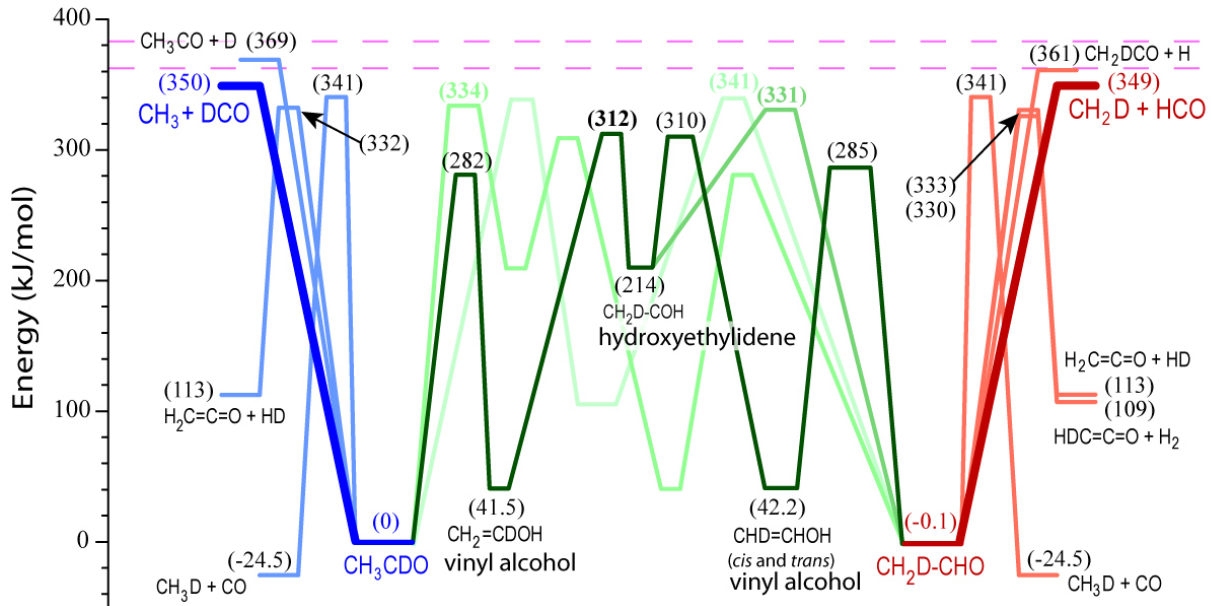


FIGURE 3.10: Schematic of the critical points on the PES for  $\text{C}_2\text{H}_3\text{DO}$ . The reactant,  $\text{CH}_3\text{CDO}$ , can react to the left forming primary products (illustrated in blue), or isomerise to the right, through a “maze” of intermediate structures (illustrated in green), which can continue to final products where H and D have been exchanged (illustrated in red). The minimum energy isomerisation pathway is illustrated in dark green and the product channels producing DCO and HCO are illustrated in dark blue and dark red respectively.

The TST treatment of the tight TS channel to methane and carbon monoxide was less severely over estimated, with respect to Dr Klippenstein’s treatment, due to the lack of  $\vec{J}$  conservation. This and our other tight TS channel rate coefficients compared well with other literature values. [86] Dr Klippenstein kindly supplied us with VRC-TST rate coefficients at appropriate energies to model our analogous  $\text{CD}_3\text{CHO}$  H/D exchange experiments [55], however we did not receive  $\text{CH}_3\text{CDO}$  rate coefficients and have had to approximate these rate coefficients for this analysis. The VRC-TST rate coefficients are not straightforward to calculate and rely on detailed knowledge of the PES, which is beyond the scope of this work.

The aims of this analysis were to determine whether any new and/or unusual dynamics, particularly roaming, are involved in H/D exchange. Therefore, if we were going to bias our results in any way, we wanted to bias against this assumption so that if our analysis could not explain the observed H/D exchange we could assume that unusual dynamics were responsible. A total

of 19 forward and 10 reverse rate coefficients were used to describe CH<sub>3</sub>CDO photodissociation, which involved 9 distinct product channels and 6 intermediates (excluding CH<sub>3</sub>CDO and CH<sub>2</sub>DCHO). These are described schematically in figure 3.10. Roaming has not been included in this analysis. Rate coefficients were calculated in this work. The VTST rate coefficients were scaled based on CD<sub>3</sub>CHO rate coefficients provided to us by Dr Klippenstein [55] and varied within their uncertainties. The DCO and HCO relative populations were modelled using a Master equation analysis.

## Master Equation Analysis

For each total energy considered, the resultant rate coefficients are combined in a simple collision-free master equation model. A brief description of Master equation analysis is given in section 2.8. The rate matrix has the form

$$\begin{array}{cccccccccccccccc}
 & a & b & c & d & e & f & g & h & i & j & k & l & m & n & o \\
 \begin{array}{l} a : \text{CH}_3\text{CDO} \\ b : \text{CH}_2\text{DCHO} \\ c : \cdot\text{CH}_3 + \text{D}\cdot\text{CO} \\ d : \cdot\text{CH}_2\text{D} + \text{H}\cdot\text{CO} \\ e : \text{CH}_3\cdot\text{CO} + \cdot\text{D} \\ f : \text{CH}_2\text{D}\cdot\text{CO} + \cdot\text{H} \\ g : \text{CDH}_3 + \text{CO} \\ h : \text{CH}_2\text{CO} + \text{HD} \\ i : \text{CHDCO} + \text{H}_2 \\ j : \text{CH}_3\text{COD} \\ k : \text{CH}_2\text{CDOH} \\ l : c\text{-CH}_2\text{OCDH} \\ m : \text{CH}_2\text{CHOD} \\ n : \text{CH}_2\text{DCOH} \\ o : \text{CHDCHOH} \end{array} & \left( \begin{array}{cccccccccccccccc} 0 & 0 & k_{ac} & 0 & k_{ae} & 0 & k_{ag} & k_{ah} & 0 & k_{aj} & k_{ak} & k_{al} & 0 & 0 & 0 & 0 \\ 0 & 0 & 0 & k_{bd} & 0 & k_{bf} & k_{bg} & k_{bh} & k_{bi} & 0 & 0 & k_{bl} & k_{bm} & k_{bn} & k_{bo} \\ 0 & 0 & 0 & 0 & 0 & 0 & 0 & 0 & 0 & 0 & 0 & 0 & 0 & 0 & 0 & 0 \\ 0 & 0 & 0 & 0 & 0 & 0 & 0 & 0 & 0 & 0 & 0 & 0 & 0 & 0 & 0 & 0 \\ 0 & 0 & 0 & 0 & 0 & 0 & 0 & 0 & 0 & 0 & 0 & 0 & 0 & 0 & 0 & 0 \\ 0 & 0 & 0 & 0 & 0 & 0 & 0 & 0 & 0 & 0 & 0 & 0 & 0 & 0 & 0 & 0 \\ 0 & 0 & 0 & 0 & 0 & 0 & 0 & 0 & 0 & 0 & 0 & 0 & 0 & 0 & 0 & 0 \\ 0 & 0 & 0 & 0 & 0 & 0 & 0 & 0 & 0 & 0 & 0 & 0 & 0 & 0 & 0 & 0 \\ 0 & 0 & 0 & 0 & 0 & 0 & 0 & 0 & 0 & 0 & 0 & 0 & 0 & 0 & 0 & 0 \\ k_{-aj} & 0 & 0 & 0 & 0 & 0 & 0 & 0 & 0 & 0 & 0 & 0 & 0 & k_{jm} & 0 & 0 \\ k_{-ak} & 0 & 0 & 0 & 0 & 0 & 0 & 0 & 0 & 0 & 0 & 0 & 0 & 0 & k_{kn} & 0 \\ k_{-al} & k_{-bl} & 0 & 0 & 0 & 0 & 0 & 0 & 0 & 0 & 0 & 0 & 0 & 0 & 0 & 0 \\ 0 & k_{-bm} & 0 & 0 & 0 & 0 & 0 & 0 & 0 & k_{-jm} & 0 & 0 & 0 & 0 & 0 & 0 \\ 0 & k_{-bn} & 0 & 0 & 0 & 0 & 0 & 0 & 0 & 0 & k_{-kn} & 0 & 0 & 0 & k_{no} & 0 \\ 0 & k_{-bo} & 0 & 0 & 0 & 0 & 0 & 0 & 0 & 0 & 0 & 0 & 0 & 0 & k_{-no} & 0 \end{array} \right) \end{array} \quad (3.3)$$

where the letters on the matrix columns correspond to the species identified at left,  $k_{ij}$  is the rate coefficient for the reaction  $i \rightarrow j$  and  $k_{-ij}$  is the rate coefficient for the reaction  $j \rightarrow i$ .

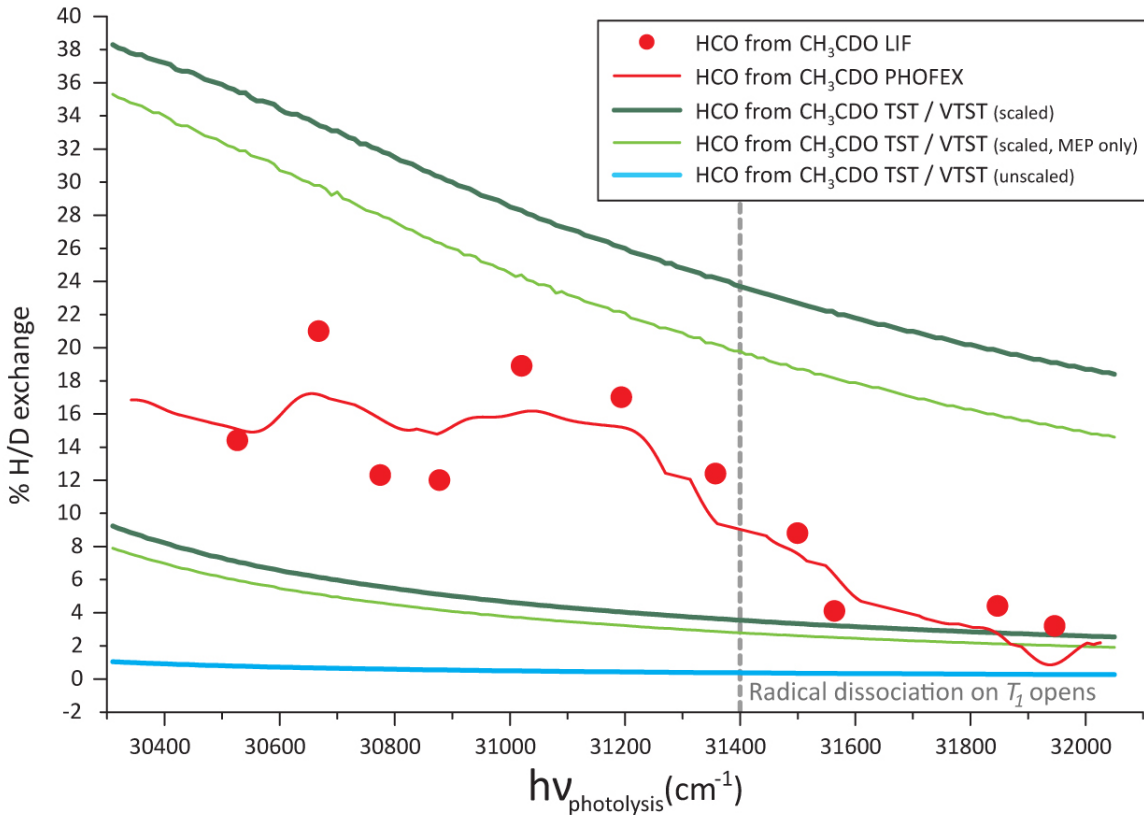


FIGURE 3.11: As a function of photolysis energy, % HCO from  $\text{CH}_3\text{CDO}$  photolysis and % DCO from  $\text{CD}_3\text{CHO}$  photolysis calculated from integration of LIF spectra (red circles for HCO and blue squares for DCO), relative intensities of PHOFEX spectra (red line for HCO and blue line for DCO) and TST prediction for % HCO from  $\text{CH}_3\text{CDO}$  photolysis including only the well known isomerisation pathways (green line).

A C++ computer code implementing this Master equation analysis was written that facilitated the calculation of DCO and HCO fragment concentrations over time, for energies within the experimental photolysis energy range. The time step size used was 1 ps and one million steps were calculated at each energy, ensuring convergence, with a total time well within the experimental time frame ( $4.6 \mu\text{s}$ ).

## Comparing Experimental And Modelled Results

Figure 3.11 re-plots the experimental data from figure 3.5, comparing it with the Master equation results. The light blue line is our theoretical prediction using VTST rate coefficients calculated using UNIMOL. The two dark green lines are upper and lower bounds obtained by dividing our VTST rates by 100 and 10, respectively. The two light green lines are the upper and lower bounds when only the MEP pathway illustrated in figure 3.9, and all product channels are included in the Master equation.

The VRC-TST methyl + formyl dissociation rate coefficients provided by Dr Klippenstein for  $\text{CD}_3\text{CHO}$  were two orders of magnitude smaller than our VTST methyl + formyl dissociation rate coefficients for  $\text{CD}_3\text{CHO}$ . [55] We expect our VTST rate coefficients to overestimate the rate and we expect VTST rates to have an uncertainty of an order of magnitude, [95] whereas VRC-TST rate coefficients are considerably more accurate. [13] We expect that the upper green line represents a more realistic description of the H/D exchange process. However, we do not presently have VRC-TST rate coefficients for the  $\text{CH}_3\text{CDO}$  system. These calculations are not trivial. We are currently calculating these rate coefficients using the VariFlex program suite developed by Klippenstein *et al.* [96]

The overall general trend towards less H/D exchange at higher energies is predicted by all of our TST / Master equation calculations. The upper and lower bounds for the relative HCO population bracket the experimental results at energies below the  $T_1$  threshold, as indicated on figure 3.11. Therefore we must conclude that the conventional reaction pathways fully explain our experimental observations. Generally, we expect the MEP to be the dominant route to products and when we include only the rate coefficients for the steps shown in figure 3.9, we predict that, on average,  $\sim 80 - 85\%$  of H/D exchange occurs via this pathway, for the lower and upper bound predictions respectively. This is notable in that all five steps in the overall mechanism occur within the  $4.6 \mu\text{s}$  between the pump and probe lasers in our experiment.

## CHAPTER 4

### Conclusions And Future Work

---

#### 4.1 Conclusions

We have produced the first Phase Space Theory (PST) model for roaming that models roaming as frustrated radical dissociation. Our PST model performs quantum state counts at fragment separations corresponding to the van der Waals region, and categorises states as roaming or radical states, based on whether they have sufficient relative translational energy to escape the attractive potential. This model requires little computational effort and input data that is easily obtainable from experimental data and/or *ab initio* calculations. The roaming to radical dissociation branching fraction has been modelled using this PST model, with results compared to experiment [5, 6] for H<sub>2</sub>CO and experiment [4] and RDT calculations [7] for CH<sub>3</sub>CHO.

In the case of formaldehyde, we assumed that all roaming states form products and varied a parameter ( $\Delta E_{roam}$ ), which describes the difference in energy between the roaming and radical thresholds. This single parameter fit matched well with the five literature experimental branching fractions [5, 6] and we obtained a physically reasonable value for  $\Delta E_{roam}$ , which sits comfortably between the experimental upper and lower bounds for the formaldehyde roaming threshold. [6] This suggested that the basic premise of our model, that roaming results from frustrated radical dissociation, is plausible. We used the formaldehyde  $\Delta E_{roam}$  value to predict roaming fractions for formaldehyde-*d*2 and found that deuteration has little affect on the fractions of roaming and radical products produced.

In the case of larger systems, like acetaldehyde, the assumption that all roaming states form products gave unrealistic results, that is, the roaming fraction was either unrealistically large,

if a physically reasonable value of  $\Delta E_{roam}$  was used, or, if  $\Delta E_{roam}$  was varied so as to match the single experimental data point [4], the fitted  $\Delta E_{roam}$  was unrealistically small. A second parameter was added to the model,  $P_{roam}$ , describing the fraction of frustrated radical dissociations that form molecular products. As molecule size increases we expect  $P_{roam}$  to decrease as reformation of the initial reactant becomes more probable. A Master equation analysis was used to obtain corrected branching fractions, incorporating  $P_{roam}$ . The value of  $\Delta E_{roam}$  was fixed at a value predicted using Lennard Jones potentials and the parameter  $P_{roam}$  was varied to fit the single CH<sub>3</sub>CHO experimental data point [4] and the RDT predictions of Klippenstein *et al.* [7] Both fits produced predictions that were within the experimental uncertainty.

This model is intended to provide an estimate of roaming fractions that is simple to implement and transferable. It is not intended to compete with other treatments, for example QCT [36,42] or RDT [7] treatments, that rely heavily on *ab initio* calculations and are likely to provide more accurate predictions. Moreover, the simplicity of this model shows us that roaming can be considered as frustrated radical dissociation.

We performed LIF and PHOFEX experiments on deuterated acetaldehyde isotopologues that revealed a facile H/D exchange process that occurs during photodissociation at near threshold energies. The CH<sub>3</sub>CDO results presented in this thesis show that the relative population of HCO produced in these experiments decreases from  $\sim 20 - 10\%$  as photolysis energy is increased from 30340 – 31400 cm<sup>-1</sup> and rapidly decreases to levels that we ascribe entirely to impurities in our sample above the  $T_1$  radical threshold.

We successfully modelled this H/D exchange using a combination of TST and VTST rate coefficients, calculated in this work, with corrections arising from VRC-TST rate coefficients for CD<sub>3</sub>CHO, provided by Dr Stephen Klippenstien. These rates were incorporated into a Master equation analysis of all energetically possible conventional reactions. Upper and lower bounds to our theoretical predictions for the relative population of HCO bracket the experimental observations. Therefore we conclude that H/D exchange occurring in the near threshold photodissociation of acetaldehyde isotopologues occurs via well known conventional reaction pathways, predominantly involving keto-enol tautomerisation between acetaldehyde and vinyl alcohol and a 1,2-hydrogen shift between vinyl alcohol and hydroxyethylidene.

These are the first H/D exchange photolysis experiments that have been performed at near threshold energies. All previous H/D exchange experiments have been performed at energies far above the threshold for H/D exchange. [70–76] The photolysis energies used in our experiment are readily available from photons in the atmosphere and therefore any isotopic labelling experiments related to atmospheric chemistry should take this H/D scrambling into account.

Roaming should be included in reaction schemes that model atmospheric and interstellar cloud chemistry and oxygenated fuel combustion. Molecular products are sinks in these schemes. The incorporation of a roaming model would help prevent the underestimation of molecular products, and thus bias, in these schemes. Our model can help predict if roaming is likely to be important in these schemes. If the model is subsequently improved, it may yield accurate roaming rate coefficients.

## 4.2 Future Work

Our overall goal is a predictive model of roaming that will describe the energy and temperature dependence, the angular momentum dependence and the pressure dependence of the roaming branching ratio. We want to improve our predictive model for  $\Delta E_{roam}$  and establish a predictive model for  $P_{roam}$ . Pressure and angular momentum dependence can be modelled by including collisions and centrifugal barriers. This would enable our model to make predictions relevant to combustion.

In the immediate future, we need to re-calculate all our  $\text{CH}_3\text{CDO}$  rate coefficients using Dr Klippenstein's VRC-TST program, "Variflex". [96] This would allow us to obtain better theoretical predictions for the H/D exchange we observed in our experiments. Our Master equation analysis for the H/D exchange experiment would also be more complete if we were to include roaming rate coefficients, that is, explicitly including our PST model in the Master equation analysis.

## References

- [1] Stroustrup, B. *The C++ Programming Language*; Addison Wesley, 1985.
- [2] Jama/c++: a translation of the java matrix library, developed by the mathworks and nist, into c++. Available from <http://math.nist.gov/tnt/download.html>, **2010**.
- [3] Pozo, R. *Int. J. High. Perform. C.* **1997**, *11*(3), 251–263.
- [4] Heazlewood, B. R.; Jordan, M. J. T.; Kable, S. H.; Selby, T. M.; Osborn, D. L.; Shepler, B. C.; Braams, B. J.; Bowman, J. M. *Proc. Nat. Acad. Sci.* **2008**, *105*(35), 12719–12724.
- [5] Suits, A. G. *Acc. Chem. Res.* **2008**, *41*(7), 873–881.
- [6] Lahankar, S. A.; Goncharov, V.; Suits, F.; Farnum, J.; Bowman, J. M.; Suits, A. G. *Chem. Phys.* **2008**, *347*, 288–299.
- [7] Harding, L. B.; Georgievskii, Y.; Klippenstein, S. J. *J. Phys. Chem. A.* **2010**, *114*(2), 765–777.
- [8] Houston, P. L.; Kable, S. H. *Proc. Nat. Acad. Sci.* **2006**, *103*(44), 16079–16082.
- [9] Gilbert, R. G.; Smith, S. C. *Theory of Unimolecular and Recombination Reactions*; Blackwell Scientific Publications, 1990.
- [10] Pilling, M. J.; Seakins, P. W. *Reaction Kinetics*; Oxford University Press, 1995.
- [11] Klippenstein, S. J. *J. Chem. Phys.* **1992**, *96*(1), 367–371.
- [12] Klippenstein, S. J. *J. Phys. Chem.* **1994**, *98*, 11459–11464.
- [13] Georgievskii, Y.; Klippenstein, S. J. *J. Chem. Phys.* **2003**, *118*(12), 5442–5455.
- [14] Townsend, D.; Lahankar, S. A.; Lee, S. K.; Chambreau, S. D.; Suits, A. G.; Zhang, X.; Rheinecker, J.; Harding, L. B.; Bowman, J. M. *Science*. **2004**, *306*, 1158–1161.
- [15] Chambreau, S. D.; Townsend, D.; Lahankar1, S. A.; Lee, S. K.; Suits, A. G. *Phys. Scr.* **2006**, *73*, C89–C93.

- [16] Heazlewood, B. R.; Rowling, S. J.; Maccarone, A. T.; Jordan, M. J. T.; Kable, S. H. *J. Chem. Phys.* **2009**, *130*, 054310.
- [17] Goncharov, V.; Herath, N.; Suits, A. G. *J. Phys. Chem. A.* **2008**, *112*, 9423–9428.
- [18] Harding, L. B., Bowman, J. M., Klippenstein, S. J., Osborn, D. L., Parker, J. K., Suits, A. G., Eds.; *Proceedings of the 1st Conference on Roaming Dynamics and Multiple Mechanisms in Chemical Reactions*, **2010**.
- [19] Harding, L. B.; Klippenstein, S. J. In Harding et al. [18].
- [20] Sivaramakrishnan, R.; Michael, J. V.; Harding, L. B.; Klippenstein, S. J. In Harding et al. [18].
- [21] North, S. W. In Harding et al. [18].
- [22] Lendvay, G. In Harding et al. [18].
- [23] Harding, L. B.; Klippenstein, S. J.; Jasper, A. W. *Phys. Chem. Chem. Phys.* **2007**, *9*, 4055–4070.
- [24] Busch, G. E.; Wilson, K. R. *J. Chem. Phys.* **1972**, *56*(7), 3626–3638.
- [25] Dugan, C. H. *J. Phys. Chem.* **1991**, *95*, 3477–3480.
- [26] Korsch, H. *Chem. Phys.* **1978**, *33*, 313–318.
- [27] Lahankar, S. A.; Chambreau, S. D.; Zhang, X.; Bowman, J. M.; Suits, A. G. *J. Chem. Phys.* **2007**, *126*, 044314.
- [28] Zhang, X.; Zou, S.; Harding, L. B.; Bowman, J. M. *J. Phys. Chem. A.* **2004**, *108*, 8980–8986.
- [29] Shepler, B. C.; Braams, B. J.; Bowman, J. M. *J. Phys. Chem. A.* **2007**, *111*(34), 8282–8285.
- [30] Sivaramakrishnan, R.; Michael, J. V.; Klippenstein, S. J. *J. Phys. Chem. A.* **2010**, *114*, 755–764.
- [31] Norton, T. S.; Dryer, F. L. *Symposium (International) on Combustion* **1991**, *23*(1), 179 – 185.
- [32] Hollis, J. M.; Lovas, F. J.; Jewell, P. R.; Coudert, L. H. *The Astrophysical Journal Letters* **2002**, *571*(1), L59.
- [33] Pope, F. D.; Smith, C. A.; Davis, P. R.; Shallcross, D. E.; Ashfold, M. N. R.; Orr-Ewing, A. J. *Faraday Discuss.* **2005**, *130*, 59–72.

- [34] Thom H. Dunning, J.; Peterson, K. A.; Woon, D. E. *Encyclopedia Of Computational Chemistry* **1998**, *1*, 87–115.
- [35] Hase, W. L. *Encyclopedia Of Computational Chemistry* **1998**, *1*, 402–407.
- [36] J.l. Rheinecker, X. Z.; Bowman, J. *Mol. Phys.* **2005**, *103*(6–8), 1067–1074.
- [37] Bolton, K.; Hase, W. L. *Encyclopedia Of Computational Chemistry* **1998**, *2*, 1357–1360.
- [38] Thompson, K. C.; Crittenden, D. L.; Kable, S. H.; Jordan, M. J. T. *J. Chem. Phys.* **2006**, *124*, 044302.
- [39] Stock, G.; MÄijller, U. *J. Chem. Phys.* **1999**, *111*(1), 65–76.
- [40] McCormack, D. A.; Lim, K. F. *Phys. Chem. Chem. Phys.* **1999**, *1*, 1–12.
- [41] Hase, W. L. *Encyclopedia Of Computational Chemistry* **1998**, *1*, 399–402.
- [42] Farnum, J. D.; Zhang, X.; Bowman, J. M. *J. Chem. Phys.* **2007**, *126*, 134305.
- [43] J.Troe. *J. Phys. Chem. A.* **2007**, *111*, 3862–3867.
- [44] J.Troe. *J. Phys. Chem. A.* **2007**, *111*, 3868–3874.
- [45] Stephen J. Klippenstein, Y. G.; Harding, L. B. In Harding et al. [18].
- [46] Lahankar, S. A.; Chambreau, S. D.; Townsend, D.; Suits, F.; Farnum, J.; Zhang, X.; Bowman, J. M.; Suits, A. G. *J. Chem. Phys.* **2006**, *125*, 044303.
- [47] Chesnavich, W. J.; Bowers, M. T. *J. Chem. Phys.* **1977**, *66*(6), 2306–2315.
- [48] Pechukas, P.; Light, J. C.; Rankin, C. *J. Chem. Phys.* **1966**, *44*(2), 794–805.
- [49] Hunter, M.; Reid, S. A.; Robie, D. C.; Reisler, H. *J. Chem. Phys.* **1993**, *99*(2), 1093–1108.
- [50] Levine, R. D.; Bernstein, R. B. *Molecular Reaction Dynamics and Chemical Reactivity*; Oxford University Press, 1987.
- [51] See comment 1 in appendix A.
- [52] Atkins, P. W.; de Paula, J. *Atkins' Physical Chemistry*; Oxford University Press, 8. ed., 2006.
- [53] Zare, R. N. *Angular Momentum Understanding Spacial Aspects In Chemistry And Physics*; John Wiley & Sons, 1988.
- [54] Kable, S. *Personal Communication*; 2010.

- [55] Klippenstein, S. J. *Personal Communication*; 2010.
- [56] Timonen, R. S.; Ratajczak, E.; Gutman, D.; Wagner, A. F. *J. Phys. Chem.* **1987**, *91*, 5325–5332.
- [57] Poling, B. E.; Prausnitz, J. M.; O'Connell, J. P. *Properties of Gases and Liquids (5th Edition)*; McGraw-Hill, 2001.
- [58] Lee, S.-H.; Chen, I.-C. *J. Chem. Phys.* **1995**, *103*(1), 104–112.
- [59] Goncharov, V.; Lahankar, S. A.; Farnum, J. D.; Bowman, J. M.; Suits, A. G. *J. Phys. Chem. A.* **2009**, *113*, 15315–15319.
- [60] Heazlewood, B. R.; Maccarone, A. T.; Andrews, D. U.; Jordan, M. J. T.; Kable, S. H.; Klippenstein, S. J. *In Preparation*. **2010**.
- [61] Urey, H.; Brickwedde, F.; Murphy, G. *Phys. Rev.* **1932**, *39*, 164.
- [62] Jefferts, K.; Penzias, A.; Wilson, R. *Astrophys. J.* **1973**, *179*, L57.
- [63] Gourier, D.; Robert, F.; Delpoux, O.; Binet, L.; Vezin, H.; Moissette, A.; Derenne, S. *Geochim. Cosmochim. Acta.* **2008**, *72*, 1914.
- [64] Feng, X.; Epstein, S. *Science*. **1994**, *265*, 1079.
- [65] Zhang, X.; Gillespie, A.; Sessions, A. *Proc. Natl. Acad. Sci. USA*. **2009**, *106*, 12580.
- [66] Kaye, J. In *Isotope Effects in Gas-Phase Chemistry*; ACS Symposium Series American Chemical Society: Washington, DC, 1992.
- [67] Konermann, L.; Tong, X.; Pan, Y. *J. Mass. Spectrom.* **2008**, *43*, 1021.
- [68] Shirota, T.; Mano, N.; Tsuge, M.; Hoshina, K. *Rapid. Comm. Mass. Spec.* **2010**, *24*, 679.
- [69] van Raalte, D.; Harrison, A. *Can. J. Chem.* **1963**, *41*, 3118.
- [70] Qadiri, R.; Feltham, E.; Nahler, N.; GarcÁś, R.; Ashfold, M. *J. Chem. Phys.* **2003**, *119*, 12842.
- [71] Ganot, Y.; Rosenwaks, S.; Bar, I. *J. Chem. Phys.* **2004**, *120*, 8600.
- [72] Robinson, J.; Sveum, N.; Goncher, S.; Neumark, D. *Mol. Phys.* **2005**, *103*, 1765.
- [73] Lin, C.-K.; Huang, C.-L.; Jiang, J.-C.; Chang, A.; Y.T. Lee, S. L.; Ni, C.-K. *J. Am. Chem. Soc.* **2002**, *124*, 4068.
- [74] Huang, C.-L.; Jiang, J.-C.; Lee, Y.; Ni, C.-K. *J. Phys. Chem. A.* **2003**, *107*, 4020.
- [75] Lee, S.-H.; Lee, Y.; Yang, X. *J. Chem. Phys.* **2004**, *120*, 10983.

- [76] Lee, S.-H.; Lee, Y.; Yang, X. *J. Chem. Phys.* **2004**, *120*, 10992.
- [77] Ruscic, B.; Boggs, J. E.; Burcat, A.; Csaszar, A. G.; Demaison, J.; Janoschek, R.; Martin, J. M. L.; Morton, M. L.; Rossi, M. J.; Stanton, J. F.; Szalay, P. G.; Westmoreland, P. R.; Zabel, F.; Berces, T. *J. Phys. Chem. Ref. Data.* **2005**, *34*(2), 573–656.
- [78] Gherman, B.; Friesner, R.; Wong, T.-H.; Min, Z.; Bersohn, R. *J. Chem. Phys.* **2001**, *114*, 6128.
- [79] Terentis, A. C.; Stone, M.; Kable, S. H. *J. Chem. Phys.* **1994**, *98*(42), 10802–10808.
- [80] Baldwin, J. E.; Fleming, R. H. *J. Am. Chem. Soc.* **1973**, *95*(16), 5249–5256.
- [81] Conroy, T. *Personal Communication*; 2010.
- [82] Luck, I. *Personal Communication*; 2010.
- [83] Noble, M.; Lee, E. K. *C. J. Chem. Phys.* **1984**, *81*(4), 1632–1642.
- [84] Amaral, G. A.; Arregui, A.; Rubio-Lago, L.; Rodríguez, J. D.; Bañares, L. *J. Chem. Phys.* **2010**, *133*, 064303.
- [85] Rowling, S. J.; Nauta, K.; Kable, S. H. *J. Molec. Spectrosc., submitted* **2010**.
- [86] Nguyen, T. L.; Vereecken, L.; Hou, X. J.; Nguyen, M. T.; Peeters, J. *J. Phys. Chem. A.* **2005**, *109*, 7489–7499.
- [87] Yang, X.; Maeda, S.; Ohno, K. *J. Phys. Chem. A.* **2007**, *111*(23), 5099–5110.
- [88] Smith, B. J.; Nguyen, M. T.; Bouma, W. J.; Radom, L. *J. Am. Chem. Soc.* **1991**, *113*, 6452–6458.
- [89] Terentis, A. C.; Kable, S. H. *Chem. Phys. Lett.* **1996**, *258*, 626–632.
- [90] Pell, A. S.; Pilcher, G. *Trans. Faraday Soc.* **1965**, *61*, 71–77.
- [91] Setser, D. W. *J. Phys. Chem.* **1966**, *70*(3), 826–840.
- [92] Unimol program suite (calculation of fall-off curves for unimolecular and recombination reactions). Gilbert, R. G.; Smith, S. C.; Jordan, M. J. T. Available from the authors: School of Chemistry, Sydney University, NSW 2006, Australia or by email to: [gilbert\\_r@summer.chem.su.oz.au](mailto:gilbert_r@summer.chem.su.oz.au), **1993**.
- [93] Gorin, E. *Acta Physicochim. URSS.* **1938**, *6*, 691.
- [94] Walker, R. B.; Light, J. C. *Ann. Rev. Phys. Chem.* **1980**, *31*, 401–433.
- [95] Sumathi, R.; Jr., W. H. G. *Theor. Chem. Acc.* **2002**, *108*, 187–213.

- [96] Variflex software, version 1.0. S.J.Klippenstein.; Wagner, A.; Robertson, S.; Dunbar, R.; Wardlaw, D. Available from the authors: Argonne National Laboratory, Argonne, IL 60439, USA: <http://glassblowing.anl.gov/chem-dyn/VariFlex/>, 1999.
- [97] Boost c++ librairies. Available from <http://www.boost.org/>, 2010.
- [98] Lee, T. J.; Taylor, P. R. *Int. J. Quantum Chem. Quant. Chem. Symp.* **1989**, s23, 199–207.
- [99] Jacox, M. E. *J. Phys. Chem. Ref. Data.* **2003**, 32(1), 1–441.
- [100] Gaussian 03, Revision C.02.p7. Frisch, M. J.; Trucks, G. W.; Schlegel, H. B.; Scuseria, G. E.; Robb, M. A.; Cheeseman, J. R.; Montgomery, Jr., J. A.; Vreven, T.; Kudin, K. N.; Burant, J. C.; Millam, J. M.; Iyengar, S. S.; Tomasi, J.; Barone, V.; Mennucci, B.; Cossi, M.; Scalmani, G.; Rega, N.; Petersson, G. A.; Nakatsuji, H.; Hada, M.; Ehara, M.; Toyota, K.; Fukuda, R.; Hasegawa, J.; Ishida, M.; Nakajima, T.; Honda, Y.; Kitao, O.; Nakai, H.; Klene, M.; Li, X.; Knox, J. E.; Hratchian, H. P.; Cross, J. B.; Bakken, V.; Adamo, C.; Jaramillo, J.; Gomperts, R.; Stratmann, R. E.; Yazyev, O.; Austin, A. J.; Cammi, R.; Pomelli, C.; Ochterski, J. W.; Ayala, P. Y.; Morokuma, K.; Voth, G. A.; Salvador, P.; Dannenberg, J. J.; Zakrzewski, V. G.; Dapprich, S.; Daniels, A. D.; Strain, M. C.; Farkas, O.; Malick, D. K.; Rabuck, A. D.; Raghavachari, K.; Foresman, J. B.; Ortiz, J. V.; Cui, Q.; Baboul, A. G.; Clifford, S.; Cioslowski, J.; Stefanov, B. B.; Liu, G.; Liashenko, A.; Piskorz, P.; Komaromi, I.; Martin, R. L.; Fox, D. J.; Keith, T.; Al-Laham, M. A.; Peng, C. Y.; Nanayakkara, A.; Challacombe, M.; Gill, P. M. W.; Johnson, B.; Chen, W.; Wong, M. W.; Gonzalez, C.; Pople, J. A.
- [101] Bouwens, R. J.; Hammerschmidt, J. A.; Grzeskowiak, M. M.; Stegink, T. A.; Yorba, P. M.; Polik, W. F. *J. Chem. Phys.* **1996**, 104(2), 460–479.
- [102] Demaison, J.; Wlodarczak, G. *Struct. Chem.* **1994**, 5(1), 57–66.
- [103] Endo, Y.; Hirota, E. *J. Mol. Spectrosc.* **1998**, 127, 540–545.
- [104] Clouthier, D. J.; Ramsay, D. A. *Ann. Rev. Phys. Chem.* **1983**, 34, 31–58.
- [105] Chuang, M.-C.; Foltz, M. F.; Moore, B. C. *J. Chem. Phys.* **1987**, 87(7), 3855–3864.
- [106] Yamada, C.; Hirota, E.; Kawaguchi, K. *J. Chem. Phys.* **1981**, 75(11), 5256–5264.
- [107] Hollenstein, H.; Günthard, H. H. *Spectrochim. Acta. A.* **1971**, 27, 2027–2060.
- [108] Stevenson, D. P.; Burnham, H. D.; Schomaker, V. *J. Am. Chem. Soc.* **1939**, 61(10), 2922–2925.
- [109] Pacansky, J.; Schrader, B. *J. Chem. Phys.* **1983**, 78(3), 1033–1038.
- [110] Makoto Yamaguchi, T. M.; Shida, T. *J. Chem. Phys.* **1990**, 93(6), 4211–4222.

- [111] Guirgis, G. A.; Drew, B.; Gounev, T.; Durig, J. *Spectrochim. Acta. A.* **1998**, *54*, 123–143.
- [112] Chen, Y.; Zhu, L. *J. Phys. Chem. A.* **2001**, *105*, 9689–9696.
- [113] Gupta, V. P. *Can. J. Chem.* **1985**, *63*, 984–987.
- [114] Chen, Y.; Zhu, L. *J. Phys. Chem. A.* **2002**, *106*, 7755–7763.
- [115] Wilson, E. B.; Decius, J. C.; Cross, P. C. *Molecular vibrations: the theory of infrared and Raman vibrational spectra*; McGraw-Hill, 1955.
- [116] Forst, W. *Phys. Chem. Chem. Phys.* **1999**, *1*, 1283–1291.
- [117] van Zee, R. D.; Foltz, M. F.; Moore, B. *J. Chem. Phys.* **1993**, *99*(3), 1664–1673.
- [118] Jordan, M. *Personal Communication*; 2010.
- [119] Friedrichs, G.; Davidson, D. F.; Hanson, R. K. *Int. J. Chem. Kinet.* **2004**, *36*(3), 157–169.
- [120] Vasudevan, V.; Davidson, D. F.; Hanson, R. K.; Bowman, C. T.; Golden, D. M. *Proc. Combust. Inst.* **2007**, *31*, 175–183.
- [121] Saxena, S.; Kiefer, J. H.; Klippenstein, S. J. *Combustion Institute Proceedings of the Combustion Institute* **2009**, *32*, 123–130.
- [122] See comment 2 in appendix A.

## APPENDIX A

### Additional Comments

---

- (1) All computer code was written in *C++* and utilised the TNT, JAMA/*C++* and Boost *C++* libraries. [1–3, 97]
- (2) We consider Bowman et al’s statement; “the CCSD(T) method properly describes dissociation to the singlet products CH<sub>4</sub> + CO; however, it does not properly describe dissociation to radical products like CH<sub>3</sub> + HCO” [29], to mean that they tested this using a T1 diagnostic. The T1 diagnostic is described in Lee, T. J.; Taylor, P. R. *Int. J. Quantum Chem. Quant. Chem. Symp.* **1989**, s23, 199-207..
- (3) This was cut from literature review - roaming TS section

However, as described above in more detail, there are difficult problems for ab initio calculations in PES regions where bonds are very long. The energies of different electronic states interact, requiring multiple determinants. Long bonds also require diffuse functions in the basis set and dynamic electron correlation. CASPT2 tries to account for multiple determinants (CAS) and the dynamic electron correlation using 2nd order perturbation theory (PT2) but the basis set is too small and a using larger basis set (has aug- so perhaps it’s the double zeta that makes it too small?) would take a very long time.

## APPENDIX B

### Data Tables

---

#### B.1 PST Roaming Model Input Data

Table B.1: Formaldehyde ( $\text{H}_2\text{CO}$ ) input values.

<b>HCO: Vibrational Levels (cm<sup>-1</sup>)</b>	<b>Energy</b>	<b>Ref</b>
1 <sub>1</sub>	2434.48	[99]
2 <sub>1</sub>	1080.76	[99]
3 <sub>1</sub>	1868.17	[99]
<b>HCO: MP2 6-31+G(2d) Vibrational Levels (cm<sup>-1</sup>)</b>	<b>Energy</b>	<b>Ref</b>
1 <sub>1</sub>	2691.4407	[100]
2 <sub>1</sub>	1127.7681	[100]
3 <sub>1</sub>	1906.9715	[100]
<b>HCO: Rotational Constants (cm<sup>-1</sup>)</b>	<b>Energy</b>	<b>Ref</b>
A	24.329602	[58]
B	1.4939571	[58]
C	1.3986631	[58]
<b>HCO: Calculated Rotational Constants (cm<sup>-1</sup>)</b>	<b>Energy</b>	<b>Ref</b>
A	19.8267	this work
B	0.739097	this work
C	0.712533	this work
<b>H<sub>2</sub>CO: Reaction Cood Freq (cm<sup>-1</sup>)</b>	<b>Energy</b>	<b>Ref</b>

Continued on Next Page...

$5_1$ antisymmetric C–H stretch	2843.0	[101]
<b>H<sub>2</sub>CO: Dissociation Energy, <math>D_0</math> (cm<sup>-1</sup>)</b>	30327.6	[6]
<b>H<sub>2</sub>CO: Alternate <math>D_0</math> (cm<sup>-1</sup>)</b>	30353.5	[89]
<b>H<sub>2</sub>CO: C–H Bond Length, <math>r_e</math> (Å)</b>	1.101	[102]
<b>H<sub>2</sub>CO: C–H Reduced Mass, <math>\mu</math> (AMU)</b>	1.1216	[100]
<b>H<sub>2</sub>CO: Morse parameter, <math>\beta</math> (Å<sup>-1</sup>)</b>	2.10457	this work
<b>H<sub>2</sub>CO: <math>\Delta E_{roam}</math>, (cm<sup>-1</sup>)</b>	161	this work
<b>H<sub>2</sub>CO: <math>\Delta E_{roam}</math>, (cm<sup>-1</sup>)</b>	178	this work

Table B.2: Formaldehyde-*d*2 (D<sub>2</sub>CO) input values.

DCO: Vibrational Levels (cm <sup>-1</sup> )	Energy	Ref
1 <sub>1</sub>	1909.77	[99]
2 <sub>1</sub>	846.5	[99]
3 <sub>1</sub>	1794.59	[99]
DCO: Rotational Constants (cm <sup>-1</sup> )	Energy	Ref
A	14.734	[103]
B	1.2815	[103]
C	1.1714	[103]
D <sub>2</sub> CO: Reaction Cood Freq (cm <sup>-1</sup> )	Energy	Ref
5 <sub>1</sub> antisymmetric C–H stretch	2159.7	[104]
D <sub>2</sub> CO: Dissociation Energy, $D_0$ (cm <sup>-1</sup> )	31020	[105]
D <sub>2</sub> CO: C–H Reduced Mass, $\mu$ (AMU)	2.4507	[100]
D <sub>2</sub> CO: Morse parameter, $\beta$ (Å <sup>-1</sup> )	2.10457	this work
D <sub>2</sub> CO: $\Delta E_{roam}$ , (cm <sup>-1</sup> )	161	this work

Table B.3: Acetaldehyde input values.

Continued on Next Page...

$\text{CH}_3$ : Vibrational Levels ( $\text{cm}^{-1}$ )	Energy	Ref
$1_1$	3004	[99]
$2_1$	606	[99]
$3_1$	3161	[99]
$4_1$	1396	[99]
$\text{CH}_3$ : Rotational Constants ( $\text{cm}^{-1}$ )	Energy	Ref
B	9.57789	[106]
C	4.74202	[106]
$\text{CH}_3$ : Calculated Rotational Constants ( $\text{cm}^{-1}$ )	Energy	Ref
B	9.57024	this work
C	4.78512	this work
$\text{CH}_3\text{CHO}$ : Reaction Cood Freq ( $\text{cm}^{-1}$ )	Energy	Ref
$8_1$ C–C stretch	1114	[107]
$\text{CH}_3\text{CHO}$ : Dissociation Energy, $D_0$ ( $\text{cm}^{-1}$ )	29257.7	[8]
$\text{CH}_3\text{CHO}$ : C–C Bond Length, $r_e$ ( $\text{\AA}$ )	1.5	[108]
$\text{CH}_3\text{CHO}$ : C–C Reduced Mass, $\mu$ (AMU)	2.2286	[100]
$\text{CH}_3\text{CHO}$ : Morse parameter, $\beta$ ( $\text{\AA}^{-1}$ )	1.18209	this work
$\text{CH}_3\text{CHO}$ : $\Delta E_{roam}$ , ( $\text{cm}^{-1}$ )	385	[7, 23]
$\text{CH}_3\text{CHO}$ : $\Delta E_{roam}$ , ( $\text{cm}^{-1}$ )	178	this work

Table B.4: Propanal input values.

$\text{C}_2\text{H}_5$ : Vibrational Levels ( $\text{cm}^{-1}$ )	Energy	Ref
$1_1$	3112	[109]
$2_1$	3033	[109]
$3_1$	2987	[109]
$4_1$	2920	[109]
$5_1$	2842	[109]

Continued on Next Page...

$6_1$	1462	[109]
$7_1$	1440	[109]
$8_1$	1427	[109]
$9_1$	1366	[109]
$10_1$	1175	[109]
$11_1$	1138	[109]
$12_1$	948	[109]
$13_1$	713	[109]
$14_1$	540	[109]
$15_1$	193	[109]
<hr/>		
CH <sub>2</sub> CHO: Vibrational Levels (cm <sup>-1</sup> )	Energy	Ref
$1_1$	3479	[110]
$2_1$	3362	[110]
$3_1$	3264	[110]
$4_1$	1674	[110]
$5_1$	1599	[110]
$6_1$	1518	[110]
$7_1$	1216	[110]
$8_1$	1030	[110]
$9_1$	532	[110]
$10_1$	1141	[110]
$11_1$	882	[110]
$12_1$	712	[110]
<hr/>		
C <sub>2</sub> H <sub>5</sub> CHO: Reaction Cood Freq (cm <sup>-1</sup> )	Energy	Ref
12 <sub>1</sub> C—C—C antisymmetric stretch	916	[111]
<hr/>		
C <sub>2</sub> H <sub>5</sub> + HCO: Dissociation Energy, $D_0$ (cm <sup>-1</sup> )	29325.5	[112]
CH <sub>3</sub> + CH <sub>2</sub> CHO: Dissociation Energy, $D_0$ (cm <sup>-1</sup> )	28985.5	[112]
<hr/>		
C <sub>2</sub> H <sub>5</sub> CHO: C—C Bond Length, $r_e$ (Å)	1.5	[113]

Continued on Next Page...

$\text{C}_2\text{H}_5\text{CHO}$ : $\Delta E_{roam}$ , ( $\text{cm}^{-1}$ )	178	this work
---	-----	-----------

Table B.5: *n*-Butanal input values.

$\text{C}_3\text{H}_7$ : Vibrational Levels ( $\text{cm}^{-1}$ )	Energy	Ref
$1_1$	3040	Scaled CCSD(T)/6-31G* NIST
$2_1$	3006	Scaled CCSD(T)/6-31G* NIST
$3_1$	2932	Scaled CCSD(T)/6-31G* NIST
$4_1$	2923	Scaled CCSD(T)/6-31G* NIST
$5_1$	1491	Scaled CCSD(T)/6-31G* NIST
$6_1$	1474	Scaled CCSD(T)/6-31G* NIST
$7_1$	1450	Scaled CCSD(T)/6-31G* NIST
$8_1$	1389	Scaled CCSD(T)/6-31G* NIST
$9_1$	1314	Scaled CCSD(T)/6-31G* NIST
$10_1$	1076	Scaled CCSD(T)/6-31G* NIST
$11_1$	1025	Scaled CCSD(T)/6-31G* NIST
$12_1$	885	Scaled CCSD(T)/6-31G* NIST
$13_1$	503	Scaled CCSD(T)/6-31G* NIST
$14_1$	324	Scaled CCSD(T)/6-31G* NIST
$15_1$	3135	Scaled CCSD(T)/6-31G* NIST
$16_1$	3012	Scaled CCSD(T)/6-31G* NIST
$17_1$	2962	Scaled CCSD(T)/6-31G* NIST
$18_1$	1481	Scaled CCSD(T)/6-31G* NIST
$19_1$	1285	Scaled CCSD(T)/6-31G* NIST
$20_1$	1182	Scaled CCSD(T)/6-31G* NIST
$21_1$	874	Scaled CCSD(T)/6-31G* NIST
$22_1$	727	Scaled CCSD(T)/6-31G* NIST
$23_1$	248	Scaled CCSD(T)/6-31G* NIST

Continued on Next Page...

$24_1$	90	Scaled CCSD(T)/6-31G* NIST
$\text{C}_3\text{H}_7\text{CHO}$ : Dissociation Energy, $D_0$ ( $\text{cm}^{-1}$ )	28653.29513	[114]
$\text{CH}_3\text{CHO}$ : $\Delta E_{roam}$ , ( $\text{cm}^{-1}$ )	178	this work

## B.2 Experimental Model Input Data

Table B.6:  $\text{CH}_3\text{CHO}$   $S_0$  Stationary Point Energies.

Label	Species	Best Energy ( $\text{kJ}\cdot\text{mol}^{-1}$ )	Source	Ref
a	$\text{CH}_3\text{CHO}$	0.0		
<b>Product Channels</b>				
b	$\cdot\text{CH}_3 + \text{H}\cdot\text{CO}$	346.9	experimental (0 K)	[77, 88, 89]
c	$\text{CH}_3\cdot\text{CO} + \cdot\text{H}$	367.4	experimental (0 K)	[77, 88, 89]
d	$\text{CH}_4 + \text{CO}$	-25.40	experimental (0 K)	[77, 88]
e	$\text{CH}_2\text{CO} + \text{H}_2$	110.5	experimental (0 K)	[77]
<b>Intermediates</b>				
f	$\text{CH}_3\text{COH}$	212.8	G3	[60, 86]
g	$\text{CH}_2\text{CHOH}$	43.00	G3	[60, 86]
h	$c\text{-CH}_2\text{OCH}_2$	115.5	experimental (0 K)	[90, 91]
j	$\cdot\text{CH}_2\text{CH}_2\text{O}\cdot$	348.9	MR-CISD+Q(8,8)/cc-pVTZ //CASSCF(8,8)/cc-pVDZ (scaled)	[86]
<b>Transition States</b>				
TS1	a - d	346.9	CCSD(T)/CBS //CCSD(T)/aug-cc-pVDZ	[7]
TS2	a - e	336.4	CCSD(T)/CBS //CCSD(T)/aug-cc-pVDZ	[7]

Continued on Next Page...

Label	Species	Best Energy (kJ·mol <sup>-1</sup> )	Source	Ref
TS3	a - f	331.2	G3	[60, 86]
TS4	a - g	282.2	G3	[60, 86]
TS5	a - h	346.9	experimental (0 K)	[90, 91]
TS6	f - g	310.2	G3	[86]

Table B.7: CH<sub>3</sub>CDO *S*<sub>0</sub> Stationary Point Energies.

(All ZPE corrections are MP2/6-311+G\*\*)

Label	Species	Energy	Source	Ref
		(kJ·mol <sup>-1</sup> )	( <i>h</i> <sub>4</sub> Energy)	
a	CH <sub>3</sub> CDO	0.0		
b	CH <sub>2</sub> DCHO	-0.1024		
<b>Product Channels</b>				
c	•CH <sub>3</sub> + D•CO	350.1	experimental (0 K)	[77, 88, 89]
d	•CH <sub>2</sub> D + H•CO	349.1	experimental (0 K)	[77, 88, 89]
e	CH <sub>3</sub> •CO + •D	368.8	experimental (0 K)	[77, 88, 89]
f	CH <sub>2</sub> D•CO + •H	360.6	experimental (0 K)	[77, 88, 89]
g	CH <sub>3</sub> D + CO	?????	experimental (0 K)	[77, 88]
h	CH <sub>2</sub> CO + HD	?????	experimental (0 K)	[77]
i	CHDCO + H <sub>2</sub>	?????	experimental (0 K)	[77]
<b>Intermediates</b>				
j	CH <sub>3</sub> COD	212.4	G3	[60, 86]
k	CH <sub>2</sub> CDOH	41.54	G3	[60, 86]
l	c-CH <sub>2</sub> OCDH	108.2	experimental (0 K)	[90, 91]
m	CH <sub>2</sub> CHOD	41.24	G3	[60, 86]
n	CH <sub>2</sub> DCOH	213.6	G3	[60, 86]
o	CHDCHOH	42.15	G3	[60, 86]

Continued on Next Page...

<b>Label</b>	<b>Species</b>	<b>Energy (kJ·mol<sup>-1</sup>)</b>	<b>Source (<i>h</i><sub>4</sub> Energy)</b>	<b>Ref</b>
<b>Transition States</b>				
TS1_ag	a - g	341.5	CCSD(T)/CBS //CCSD(T)/aug-cc-pVDZ	[7]
TS1_bg	b - g	340.6	CCSD(T)/CBS //CCSD(T)/aug-cc-pVDZ	[7]
TS2_ah	a - h	332.0	CCSD(T)/CBS //CCSD(T)/aug-cc-pVDZ	[7]
TS2_bh	b - h	333.2	CCSD(T)/CBS //CCSD(T)/aug-cc-pVDZ	[7]
TS2_bi	b - i	329.7	CCSD(T)/CBS //CCSD(T)/aug-cc-pVDZ	[7]
TS3_aj	a - j	333.8	G3	[60, 86]
TS3_bn	b - n	331.0	G3	[60, 86]
TS4_ak	a - k	281.5	G3	[60, 86]
TS4_bm	b - m	282.0	G3	[60, 86]
TS4_bo	b - o	284.7	G3	[60, 86]
TS5_al	a - l	339.9	experimental (0 K)	[90, 91]
TS5_bl	b - l	341.1	experimental (0 K)	[90, 91]
TS6_jm	j - m	308.4	G3	[86]
TS6_nk	n - k	312.0	G3	[86]
TS6_no	n - o	309.7	G3	[86]

Table B.8: CH<sub>3</sub>CDO *S*<sub>0</sub> Stationary Point Frequencies.

(All calculations are MP2/6-311+G\*\*)

<b>Species</b>	<b>Frequencies (cm<sup>-1</sup>)</b>	<b>Rot Const (GHz)</b>
CH <sub>3</sub> CDO	3203,3156,3074,2182,1760,1489,1483,	45.1, 10.1, 8.69

Continued on Next Page...

<b>Species</b>	<b>Frequencies (cm<sup>-1</sup>)</b>	<b>Rot Const (GHz)</b>
	1397,1138,1111,1071,860,689,502,142	
CH <sub>2</sub> DCHO	3197,3111,2956,2291,1772,1470,1440, 1305,1293,1129,1095,865,683,501,131	52.3, 9.35, 8.55
<b>Product Channels</b>		
•CH <sub>3</sub> + D•CO	3364,3364,3171,1451,1451,464 2077,1868,875	287, 287, 144 423, 38.3, 35.1
•CH <sub>2</sub> D + H•CO	3364,3248,2407,1446,1214,432 2743,1941,1127	287, 177, 110 704, 44.4, 41.8
CH <sub>3</sub> •CO + •D	3220,3218,3111,1975,1525,1524,1419, 1091,989,896,468,74	81.9, 9.92, 9.36
CH <sub>2</sub> D•CO + •H	3220,3165,2320,1974,1497,1337,1327, 951,932,886,430,71	66.6, 9.62, 8.87
<b>Intermediates</b>		
CH <sub>3</sub> COD	3157,3150,3049,2779,1487,1467,1376,1327, 1193,963,934,887,584,501,95	55.0, 9.76, 8.73
CH <sub>2</sub> CDOH	3859,3305,3194,2406,1671,1438,1332,1160, 1015,916,817,761,689,484,413	47.3, 10.5, 8.60
c-CH <sub>2</sub> OCDH	3256,3209,3154,2356,1547,1419,1297,1185, 1175,1117,1074,924,863,847,723	24.3, 19.9, 13.3
CH <sub>2</sub> CHOD	3306,3247,3193,2809,1693,1448,1346,1226, 1010,984,898,762,704,463,321	52.8, 10.3, 8.60
CH <sub>2</sub> DCOH	3817,3150,3106,2274,1436,1382,1327,1280, 1278,971,970,892,715,469,91	47.4, 10.2, 8.84
CHDCHOH	3860,3279,3244,2379,1674,1397,1348,1256, 1087,957,889,736,612,442,405	50.5, 10.1, 8.44
<b>Transition States</b>		
TS1_ag	3200,3178,3049,2466,1733,1442,1433,1088, 752,744,505,501,280,146	42.1, 7.95, 6.10

Continued on Next Page...

<b>Species</b>	<b>Frequencies (cm<sup>-1</sup>)</b>	<b>Rot Const (GHz)</b>
TS1_bg	3231,3184,3096,2304,1842,1413,1227,1019, 933,740,534,444,266,134	42.5, 7.64, 6.90
TS2_ah	3286,3165,1938,1780,1480,1370,1176,1149, 1068,863,781,673,541,454	49.3, 10.1, 8.64
TS2_bh	3286,3165,2035,1915,1478,1308,1152,1127, 1079,863,855,660,553,444	52.4, 9.98, 8.71
TS2_bi	3245,2364,2128,1914,1584,1374,1271,1127, 1028,911,722,672,532,465	54.3, 9.69, 8.44
TS3_aj	3163,3161,3049,1966,1479,1465,1375,1364, 1133,931,911,487,441,130	54.0, 9.68, 8.65
TS3_bn	3163,3114,2682,2270,1449,1385,1313,1273, 1013,908,887,569,437,124	50.0, 9.74, 8.58
TS4_ak	3245,3146,2354,1912,1523,1469,1247,1183, 1077,919,855,781,618,575	38.8, 12.3, 9.70
TS4_bm	3223,3171,2327,1923,1547,1393,1281,1158, 1128,1055,954,775,577,475	42.9, 11.6, 9.73,
TS4_bo	3246,3173,3144,1550,1498,1394,1277,1211, 1071,980,909,780,652,554	43.8, 12.3, 10.0
TS5_al	3244,3118,2599,2219,1504,1408,1263,1136, 1104,988,942,834,736,543	33.1, 12.2, 9.74
TS5_bl	3906,3264,3097,1667,1502,1404,1273,1155, 1100,1016,969,648,582,485	35.1, 12.0, 10.0
TS6_jm	3264,3097,2845,2252,1524,1384,1338,1203, 1029,975,929,711,477,437	59.2, 10.0, 8.90
TS6_nk	3906,3264,3097,1667,1502,1404,1273,1155, 1100,1016,969,648,582,485	52.2, 10.4, 9.29
TS6_no	3906,3247,2312,2232,1488,1360,1309,1265, 1097,915,868,677,575,437	50.3, 10.4, 8.94



Table B.9: CH<sub>3</sub>CD<sub>2</sub>O rate coefficients near the experimental photolysis energies.

Product or Label	Transition State	Rate Coefficient (s <sup>-1</sup> ) at the photolysis energies listed in the header below in cm <sup>-1</sup>
$k_{ac}$	CH <sub>3</sub> + DCO	6.32 × 10 <sup>8</sup>
$k_{bd}$	CH <sub>2</sub> D + HCO	1.04 × 10 <sup>9</sup>
$k_{ae}$	CH <sub>3</sub> CO + D	0.00 × 10 <sup>0</sup>
$k_{bf}$	CH <sub>2</sub> DCO + H	7.59 × 10 <sup>6</sup>
$k_{ag}$	TS1_ag	6.01 × 10 <sup>5</sup>
$k_{bg}$	TS1_bg	8.04 × 10 <sup>5</sup>
$k_{ah}$	TS2_ah	8.84 × 10 <sup>5</sup>
$k_{bh}$	TS2_bh	2.42 × 10 <sup>5</sup>
$k_{bi}$	TS2_bi	7.68 × 10 <sup>5</sup>
$k_{aj}$	TS3_aj	6.59 × 10 <sup>5</sup>
$k_{-aj}$	TS3_aj	1.12 × 10 <sup>9</sup>
$k_{bn}$	TS3_bn	1.86 × 10 <sup>9</sup>
$k_{-bm}$	TS3_bn	1.05 × 10 <sup>6</sup>
$k_{ak}$	TS4_ak	8.21 × 10 <sup>7</sup>
$k_{-ak}$	TS4_ak	1.34 × 10 <sup>8</sup>
$k_{bm}$	TS4_bm	1.85 × 10 <sup>7</sup>
$k_{-bm}$	TS4_bm	9.03 × 10 <sup>7</sup>
$k_{bo}$	TS4_bo	5.35 × 10 <sup>7</sup>
$k_{-bo}$	TS4_bo	1.32 × 10 <sup>8</sup>
$k_{al}$	TS5_al	1.28 × 10 <sup>5</sup>
$k_{-al}$	TS5_al	1.31 × 10 <sup>7</sup>
$k_{bl}$	TS5_bl	1.01 × 10 <sup>7</sup>
$k_{-bl}$	TS5_bl	3.41 × 10 <sup>4</sup>
$k_{jm}$	TS6_jm	1.59 × 10 <sup>7</sup>
$k_{-jm}$	TS6_jm	1.67 × 10 <sup>10</sup>
	30530	30670
	30770	30880
	31020	31190
	31360	31560
	31850	31950

Continued on Next Page...

		Rate Coefficient ( $s^{-1}$ ) at the photolysis energies listed in the header below in $\text{cm}^{-1}$									
Label	Product or Transition State	30530	30670	30770	30880	31020	31190	31360	31560	31850	31950
$k_{nk}$	TS6_nk	$9.80 \times 10^6$	$1.11 \times 10^7$	$1.20 \times 10^7$	$1.31 \times 10^7$	$1.47 \times 10^7$	$1.68 \times 10^7$	$1.90 \times 10^7$	$2.21 \times 10^7$	$2.71 \times 10^7$	$2.91 \times 10^7$
$k_{-nk}$	TS6_nk	$3.53 \times 10^9$	$3.84 \times 10^9$	$4.05 \times 10^9$	$4.30 \times 10^9$	$4.63 \times 10^9$	$5.08 \times 10^9$	$5.52 \times 10^9$	$6.09 \times 10^9$	$6.98 \times 10^9$	$7.32 \times 10^9$
$k_{no}$	TS6_no	$1.03 \times 10^{10}$	$1.11 \times 10^{10}$	$1.17 \times 10^{10}$	$1.24 \times 10^{10}$	$1.34 \times 10^{10}$	$1.45 \times 10^{10}$	$1.58 \times 10^{10}$	$1.73 \times 10^{10}$	$1.98 \times 10^{10}$	$2.06 \times 10^{10}$
$k_{-no}$	TS6_no	$1.44 \times 10^7$	$1.60 \times 10^7$	$1.73 \times 10^7$	$1.89 \times 10^7$	$2.11 \times 10^7$	$2.39 \times 10^7$	$2.72 \times 10^7$	$3.13 \times 10^7$	$3.85 \times 10^7$	$4.10 \times 10^7$

## APPENDIX C

### Additional Figures And Previously Recorded Spectra

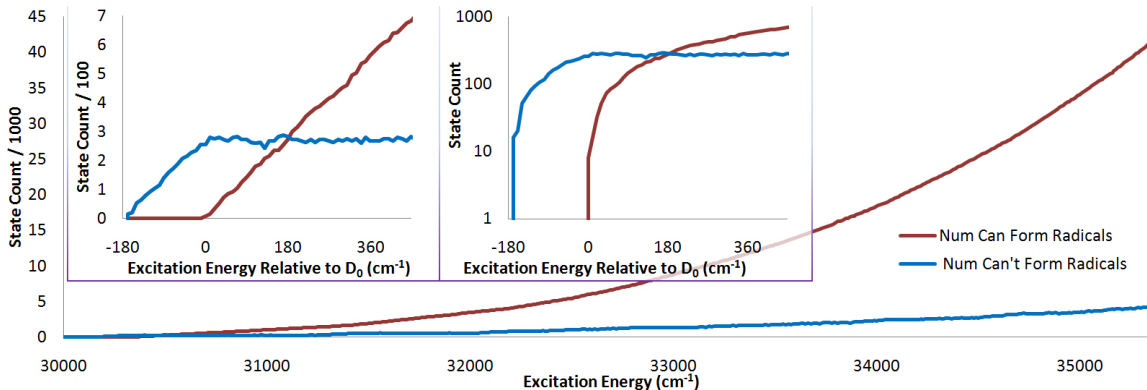


FIGURE C.1: For formaldehyde,  $\omega_{roam}(E_A)$  and  $\omega_{rad}(E_A)$  in the range ( $E_{tot} = 29000 - 34000 \text{ cm}^{-1}$ ) where  $\Delta E_{roam} = 178 \text{ cm}^{-1}$  and  $P_{roam} = 1$ . Inset, close up of a range starting at  $E_{tot} = 29100 \text{ cm}^{-1}$  with the energy scale relative to  $D_0$  ( $29274.5 \text{ cm}^{-1}$ ).

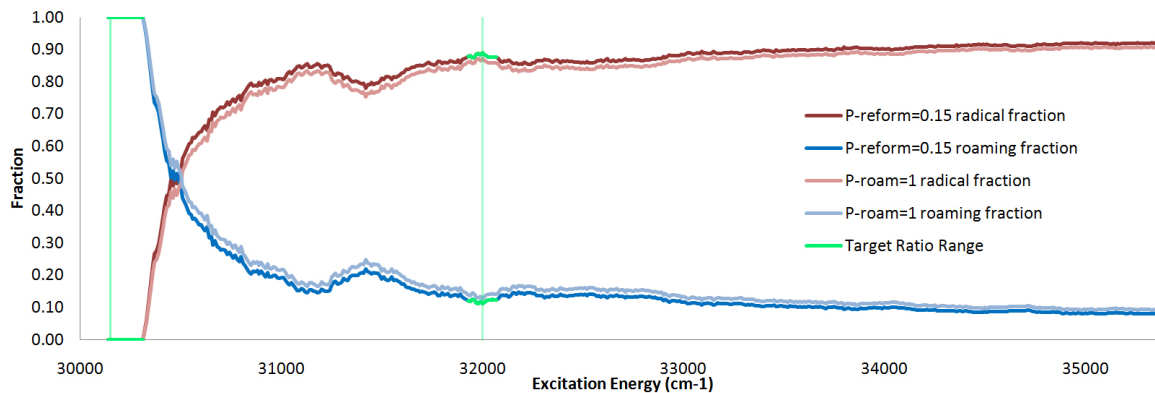


FIGURE C.2: For formaldehyde, In red and dark blue, the radical and roaming fractions in the range ( $E_{tot} = 29000 - 34000 \text{ cm}^{-1}$ ) where  $\Delta E_{roam} = 178 \text{ cm}^{-1}$  and  $P_{reform} = 0.15$ . In pink and light blue, the equivalent radical and roaming fractions where  $P_{roam} = 1$  ( $P_{reform} = 0$ ).

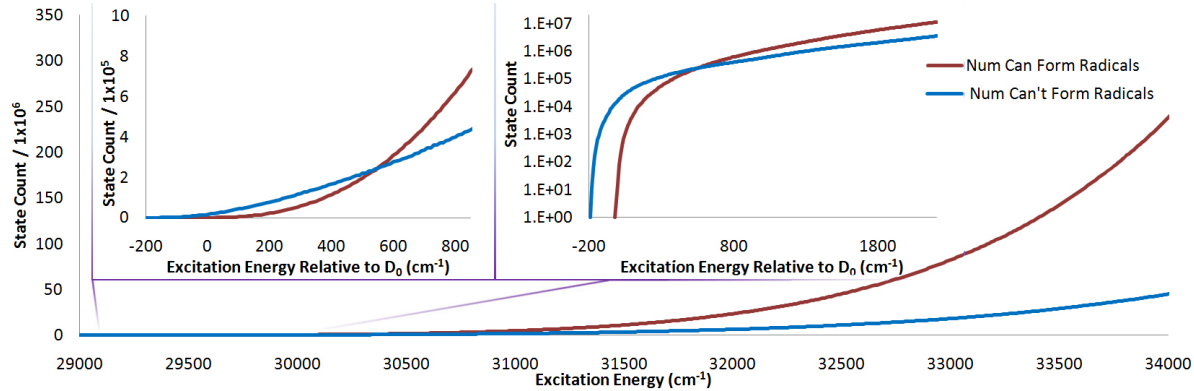


FIGURE C.3: For acetaldehyde,  $\omega_{roam}(E_A)$  and  $\omega_{rad}(E_A)$  in the range ( $E_{tot} = 29000 - 34000 \text{ cm}^{-1}$ ) where  $\Delta E_{roam} = 178 \text{ cm}^{-1}$  and  $P_{roam} = 1$ . Inset, close up of a range starting at  $E_{tot} = 29100 \text{ cm}^{-1}$  with the energy scale relative to  $D_0$  ( $29274.5 \text{ cm}^{-1}$ ).

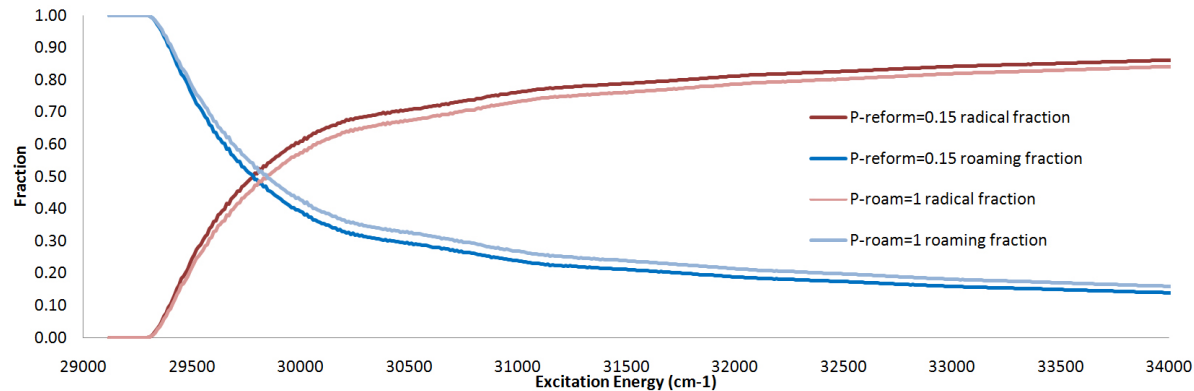


FIGURE C.4: For acetaldehyde, In red and dark blue, the radical and roaming fractions in the range ( $E_{tot} = 29000 - 34000 \text{ cm}^{-1}$ ) where  $\Delta E_{roam} = 178 \text{ cm}^{-1}$  and  $P_{reform} = 0.15$ . In pink and light blue, the equivalent radical and roaming fractions where  $P_{roam} = 1$  ( $P_{reform} = 0$ ).

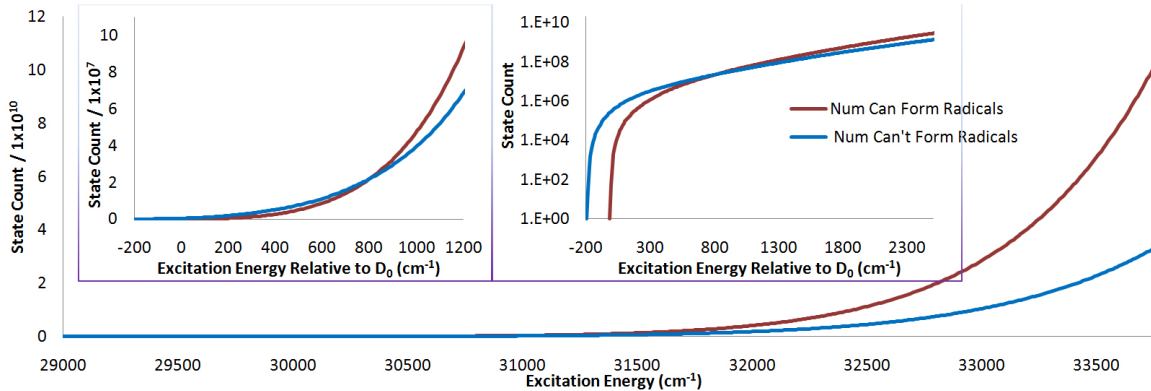


FIGURE C.5: For propanal,  $\omega_{roam}(E_A)$  and  $\omega_{rad}(E_A)$  in the range ( $E_{tot} = 29000 - 34000 \text{ cm}^{-1}$ ) where  $\Delta E_{roam} = 178 \text{ cm}^{-1}$  and  $P_{roam} = 1$ . Inset, close up of a range starting at  $E_{tot} = 29100 \text{ cm}^{-1}$  with the energy scale relative to  $D_0$  ( $29274.5 \text{ cm}^{-1}$ ).

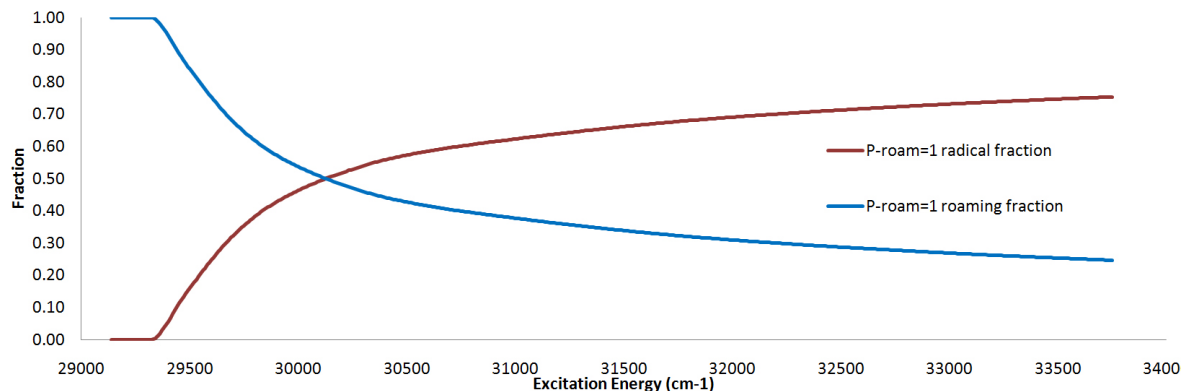


FIGURE C.6: For propanal, In red and dark blue, the radical and roaming fractions in the range ( $E_{tot} = 29000 - 34000 \text{ cm}^{-1}$ ) where  $\Delta E_{roam} = 178 \text{ cm}^{-1}$  and  $P_{reform} = 0.15$ . In pink and light blue, the equivalent radical and roaming fractions where  $P_{roam} = 1$  ( $P_{reform} = 0$ ).

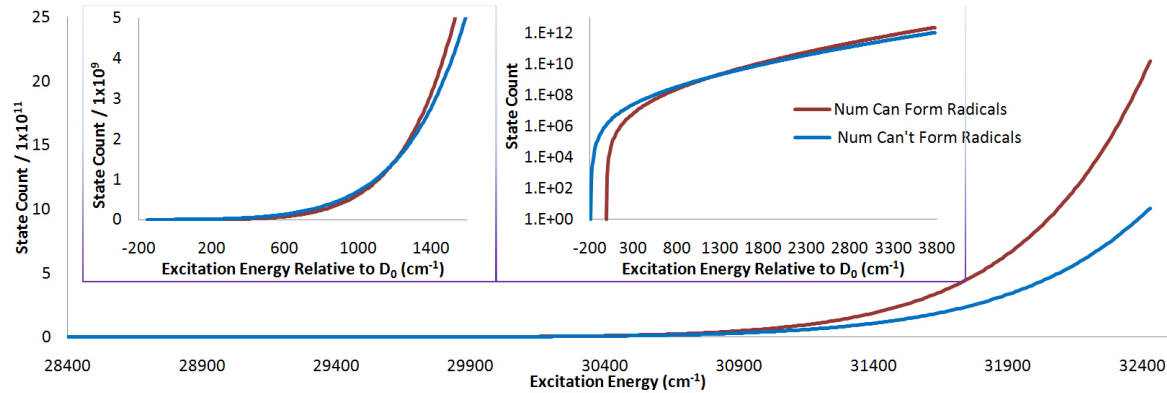


FIGURE C.7: For butanal,  $\omega_{roam}(E_A)$  and  $\omega_{rad}(E_A)$  in the range ( $E_{tot} = 29000 - 34000 \text{ cm}^{-1}$ ) where  $\Delta E_{roam} = 178 \text{ cm}^{-1}$  and  $P_{roam} = 1$ . Inset, close up of a range starting at  $E_{tot} = 29100 \text{ cm}^{-1}$  with the energy scale relative to  $D_0$  ( $29274.5 \text{ cm}^{-1}$ ).

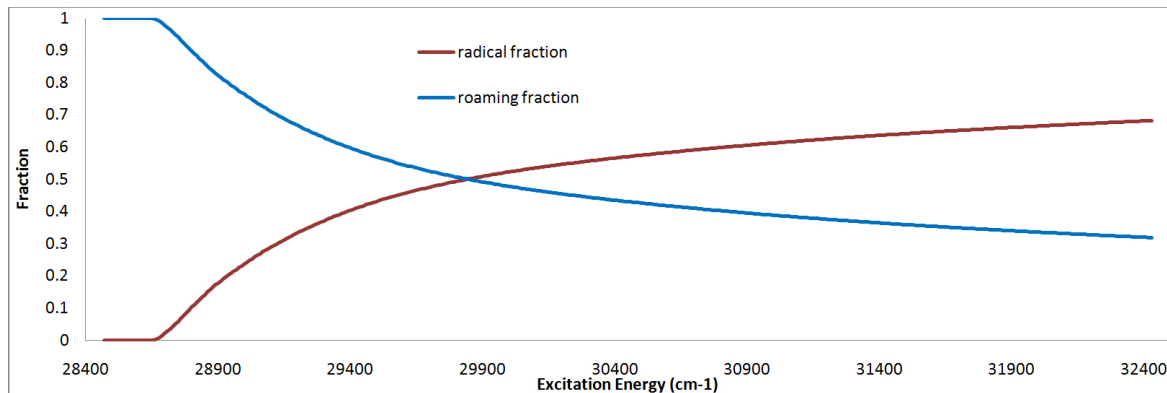


FIGURE C.8: For butanal, In red and dark blue, the radical and roaming fractions in the range ( $E_{tot} = 29000 - 34000 \text{ cm}^{-1}$ ) where  $\Delta E_{roam} = 178 \text{ cm}^{-1}$  and  $P_{reform} = 0.15$ . In pink and light blue, the equivalent radical and roaming fractions where  $P_{roam} = 1$  ( $P_{reform} = 0$ ).

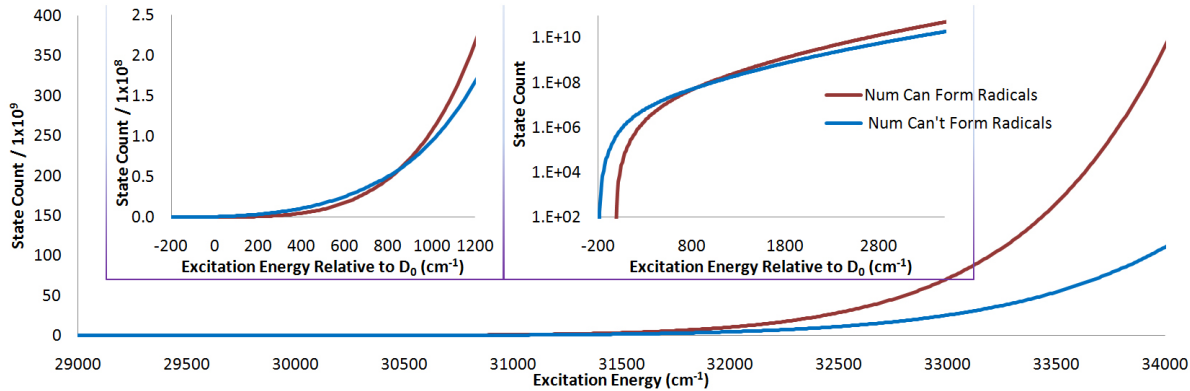


FIGURE C.9: For  $(\text{CH}_3)_2\text{CO}$ ,  $\omega_{roam}(E_A)$  and  $\omega_{rad}(E_A)$  in the range ( $E_{tot} = 29000 - 34000 \text{ cm}^{-1}$ ) where  $\Delta E_{roam} = 178 \text{ cm}^{-1}$  and  $P_{roam} = 1$ . Inset, close up of a range starting at  $E_{tot} = 29100 \text{ cm}^{-1}$  with the energy scale relative to  $D_0$  ( $29274.5 \text{ cm}^{-1}$ ).

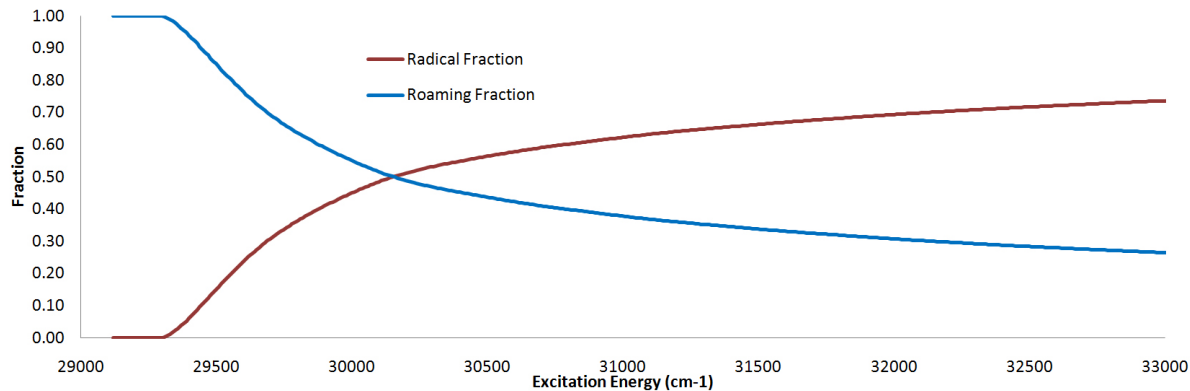


FIGURE C.10: For  $(\text{CH}_3)_2\text{CO}$ , In red and dark blue, the radical and roaming fractions in the range ( $E_{tot} = 29000 - 34000 \text{ cm}^{-1}$ ) where  $\Delta E_{roam} = 178 \text{ cm}^{-1}$  and  $P_{reform} = 0.15$ . In pink and light blue, the equivalent radical and roaming fractions where  $P_{roam} = 1$  ( $P_{reform} = 0$ ).

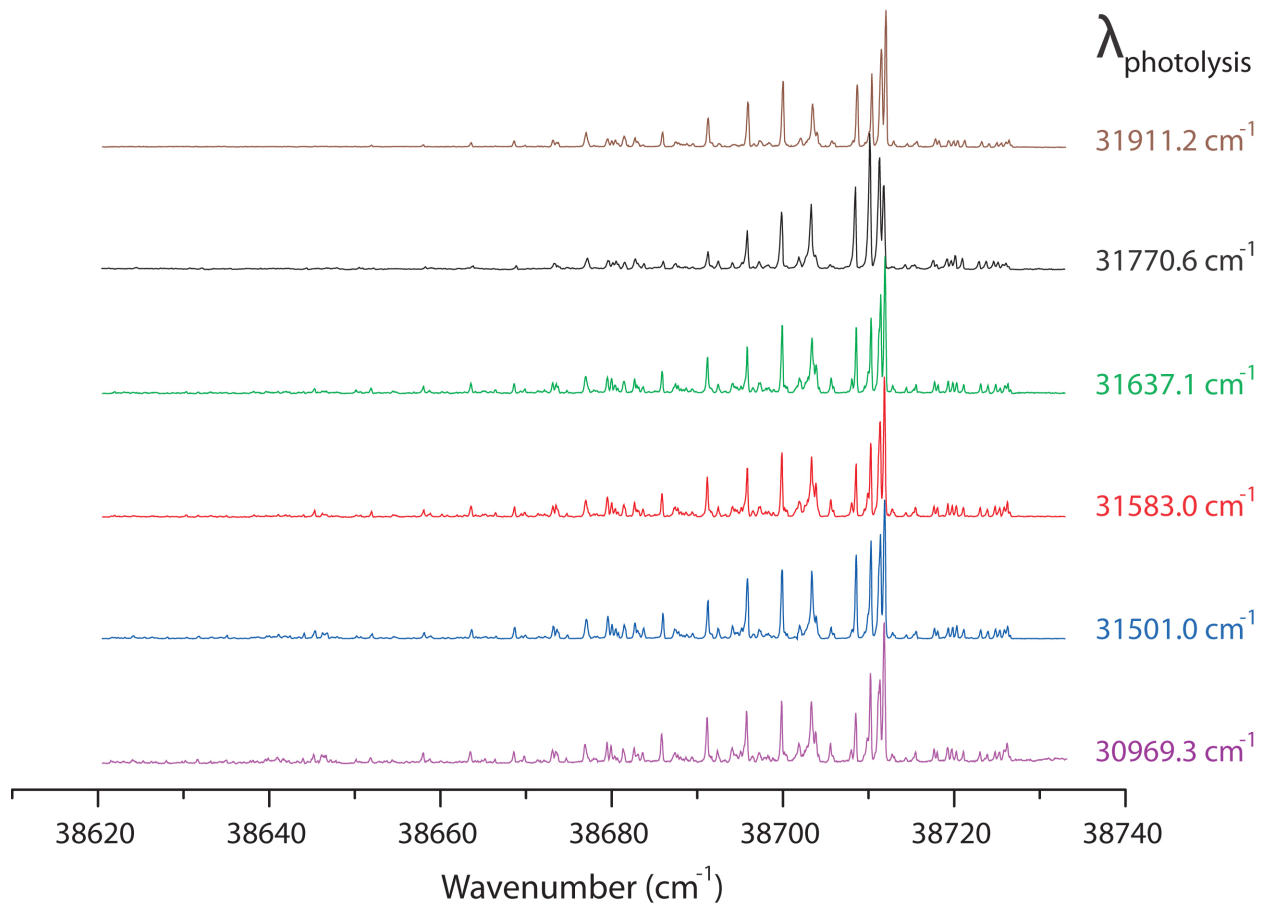


FIGURE C.11: Previously recorded LIF spectra of formyl fragments produced by photolysis of a  $\text{CD}_3\text{CHO}$  parent molecule, with various pump laser energies and the probe laser scanned in the range ( $\lambda = 258.2 - 259.4 \text{ nm}$ ).

## APPENDIX D

### PST State Count Algorithm Description and Pseudocode

---

#### D.1 Accommodating Generic Cases

## APPENDIX E

### Variational Transition State Theory Implementation

---

## E.1 Addressing Problems With The Original UNIMOL GEOM Program

For all species (so far) investigated in this work, there are several problems with the original UNIMOL GEOM program as it relates to calculating variational RRKM rates for the barrierless  $S_0$  two-body radical dissociation channel (2). We have written a *C++* version of GEOM that better accommodates fragments, such as formyl fragments, where the most unequal principal moment of inertia does not point along the reaction coordinate. This calculation is required to obtain rates required in the master equation analyses of isotope exchange accompanying the CD<sub>3</sub>CHO and CH<sub>3</sub>CDO LIF experiments, and for predicting radical and roaming branching fractions where flux from the tight TS channel is included.

In the original UNIMOL GEOM Fortran code (probably need to explain how the rotational constants are used to get rates etc too), the principal rotational constants of each fragment are obtained as the eigenvalues of the moment of inertia tensor. An assumption is made; that the most different moment of inertia (symmetric top approximation) is always pointing along the reaction coordinate and is therefore the torsional moment of inertia for the fragment.

This assumption is only valid if the fragment has its oblate or prolate axis of symmetry pointing along the reaction coordinate. In the CH<sub>3</sub>CHO → CH<sub>3</sub> + HCO reaction, the oblate axis of the methyl fragment does point along the reaction coordinate. However the formyl fragment does not have its approximate prolate axis of symmetry pointing along the reaction coordinate. This is caused both, by the orientation of the fragment relative to the reaction coordinate, and the

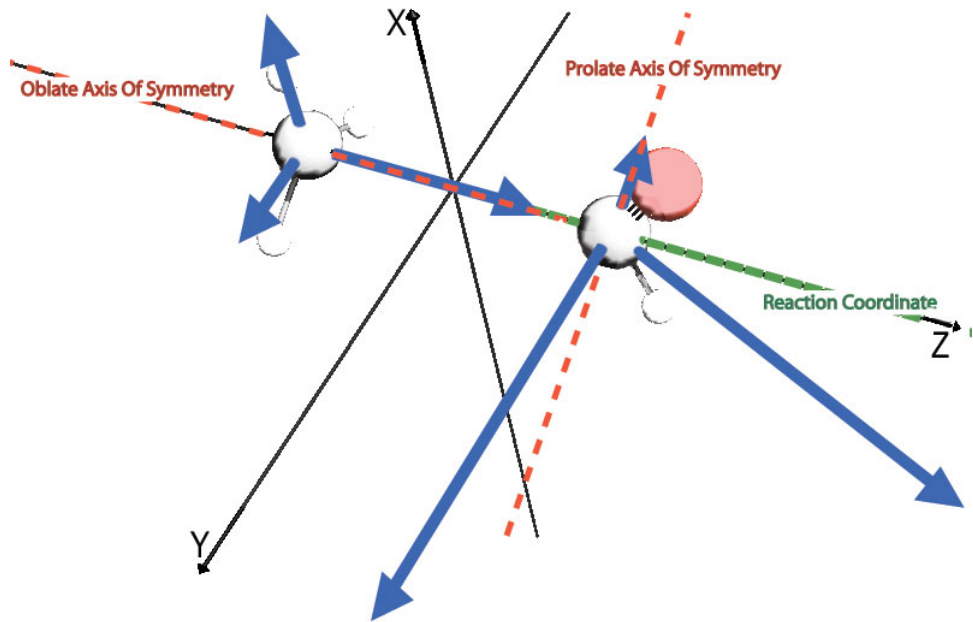


FIGURE E.1: The methyl principal moments of inertia point along the  $x$ ,  $y$ ,  $z$  axes and the most unequal moment points along the reaction coordinate, which is on the  $z$  axis in this diagram. The formyl principal moments of inertia do not point along the  $x$ ,  $y$ ,  $z$  axes and the most unequal moment is closest to  $x$  axis which is perpendicular to the reaction coordinate.

fragment pivot atom being far from the fragment centre of mass. Moreover, the most unique moment of inertia of the formyl fragment does not lie along the reaction coordinate if the principal moments of inertia are projected onto the  $x$ ,  $y$  or  $z$  axis that maximises their value, see figure 2.1.

To correctly estimate the torsional moment of inertia, we must calculate the moment of inertia with its axis explicitly along the reaction coordinate, rather than simply assuming the principal eigenvalues of the inertia tensor point in the required directions. Programmatically, this corresponds to the moment of inertia along the  $z$  axis because GEOM rotates the molecule such that the reaction coordinate is on the  $z$  axis. This is obtained as

$$I_z = \sum_{i=0}^{n_{atoms}} m_i(y_i^2 + x_i^2) \quad (\text{E.1})$$

where  $n_{atoms}$  is the number of atoms in the fragment,  $m_i$  is the mass of atom  $i$  and  $y_i$  and  $x_i$  are the  $y$  and  $x$  coordinates of atom  $i$  relative to the pivot atom respectively. The 2d rotor is then

obtained as an average of the moments of inertia in the  $y$  and  $x$  directions, obtained as

$$I_y = \sum_{i=0}^{n_{atoms}} m_i(z_i^2 + x_i^2) \quad (\text{E.2})$$

and

$$I_x = \sum_{i=0}^{n_{atoms}} m_i(y_i^2 + z_i^2) \quad (\text{E.3})$$

respectively, where  $z_i$  is the  $z$  coordinate of atom  $i$  relative to the pivot atom.

Having changed the way the moments of inertia are obtained for fragments, we must ensure that the averages, used for both the 2d rotor of fragments and the overall average moment of inertia for the molecule, are equivalent to each other when calculated using both methods (principal vs  $x, y, z$  explicitly). Since the symmetry assumptions about the formyl fragment are incorrect, this comparison can only be made for the methyl fragment and the overall molecule. The results for the methyl fragment are identical for both methods. This is expected since the original symmetry assumptions are correct for the methyl fragment, thus the  $x, y, z$  moments of inertia *are* the principal moments of inertia. For the overall molecule, the geometric average used in the original UNIMOL GEOM code is *not* consistent using both methods for calculating the moments of inertia. However the arithmetic mean *is* identical for the methyl fragment *and* the overall molecule using both methods. This leads us to conclude that it is the arithmetic mean we should be using in our calculations. Furthermore, Zare uses the arithmetic mean in his derivation [53]. Since the arithmetic mean is the same using either method, we are confident that using the arithmetic mean of the  $x$  and  $y$  moments of inertia for the 2d rotor approximation is correct. Moreover, this is equivalent to treating them as two separate one dimensional rotors.

It should however be noted that for the PST state count, the fragments are treated as “completely unhindered and freely rotating”. Therefore, in this case, the principal moments of inertia for the fragments should be used to obtain the fragment rotational constants. Using  $x, y, z$  moments of inertia for the PST state count may cause errors when identifying whether a fragment is oblate or prolate. For example, a freely rotating formyl fragment is prolate, however if the  $x, y, z$  moments of inertia are used, our program evaluates the formyl fragment as oblate. This is because our PST program treats fragments with a 2d rotor rotational constant that is smaller than the

most unique rotational constant as prolate (*prolate* = ( $\vec{A} > \vec{B}$ )), and all other fragments as oblate. If principal axes system moments of inertia are used, the 2d rotor rotational constant is correctly calculated as the arithmetic average of the 2 similar rotational constants. However if  $x, y, z$  rotational constants are used, the 2d rotor is incorrectly calculated as the arithmetic average of the  $y$  and  $x$  moments of inertia, which is smaller than the  $z$  moment of inertia. Therefore  $\vec{A} < \vec{B}$  and formyl is incorrectly evaluated as oblate. An incorrect evaluation of symmetry type results in the wrong formula being used to calculate the maximum possible angular momentum for the fragment.

## APPENDIX F

### **Additional Considerations For Modelling Pyrolysis Experiments**

---

#### **F.1 Morse Curve And $\Delta E_{roam}$**

Recall that figure 2.1 illustrates the relationship between  $\Delta E_{roam}$ ,  $r_{roam}$  and the PES. In principle we need an *ab initio* PES to derive an accurate value for  $r_{roam}$  from  $\Delta E_{roam}$ . However, if we can model the PES in a transferable way, we can make predictions for  $r_{roam}$  for systems where no *ab initio* PES is available. Note that the only reason we are using a PES model at all is to get  $r_{roam}$  so we can compare it to the  $r_{sep}$  for Harding *et al.*'s roaming TSs.

For simplicity and transferability, the attractive potential of the radical channel is approximated using a ZPE corrected Morse curve, given by

$$V(r) = D_0 \left(1 - e^{-\beta(r-r_e)}\right)^2 \quad (\text{F.1})$$

The asymptote at infinite separation is defined by the experimental dissociation energy ( $D_0$ ) and the minimum is defined by the experimental equilibrium reaction coordinate bond length ( $r_e$ ). The Morse parameter ( $\beta$ ) is given by

$$\beta = 2\pi\omega_{RC} \sqrt{\frac{\mu_{RC}}{2D_0}} \quad (\text{F.2})$$

where  $\mu_{RC}$  is the reduced mass of the reaction coordinate, obtained as the appropriate Wilson G matrix element, and  $\omega$  is the experimental reaction coordinate harmonic frequency. [115, 116] Table B.1 lists values for  $D_0$ ,  $r_e$ ,  $\beta$ ,  $\mu_{RC}$  and  $\omega$  (5<sub>1</sub>, the asymmetric C–H stretch), used to model formaldehyde.

An estimate of the roaming threshold bond length ( $r_{roam}$ ) can be obtained from this PES approximation, by rearranging equation F.1 and substituting  $V(r_{roam}) = D_0 - \Delta E_{roam}$ , that is,

$$r_{roam} = -\ln \left( 1 - \sqrt{\frac{D_0 - \Delta E_{roam}}{D_0}} \right) \beta^{-1} + r_e \quad (\text{F.3})$$

For formaldehyde, with  $\Delta E_{roam} = 149 \text{ cm}^{-1}$  and using the simple Morse approximation described above,  $r_{roam}$  is found to be  $4.0 \text{ \AA}$ . This is longer than the  $3.5 \text{ \AA}$  C–H bond length predicted by the CASPT2/aug-cc-pvdz *ab initio* formaldehyde roaming transition state of Harding *et al.* [23]. This roaming TS lies  $\sim 40 - 80 \text{ cm}^{-1}$  below the radical threshold, which results in  $r_{roam} > 4 \text{ \AA}$  using our simple Morse approximation. [6] For acetaldehyde, using the simple Morse approximation,  $r_{roam} = 5.7 \text{ \AA}$  and  $r_{roam} = 6.7 \text{ \AA}$  with  $\Delta E_{roam} = 385$  and  $122 \text{ cm}^{-1}$  respectively, which are both much longer than the  $3.4 \text{ \AA}$  predicted by the acetaldehyde roaming TS of Harding *et al.* [23]. While the suitability of CASPT2 method for modelling this PES region is debatable, there is no question that the accuracy our Morse curve approximation is relatively poor in this region. The advantage being that a Morse curve approximation is simple to implement and only requires readily available experimental values or calculations as inputs, making it generally transferable. However there appears to be a problem with using this simple model to predict  $r_{roam}$  for larger molecules, as for propanal the simple Morse approximation gives  $r_{roam} = 6.9 \text{ \AA}$  and for *n*-butanal it gives  $r_{roam} = 8.0 \text{ \AA}$ . This trend to longer  $r_{roam}$  is supported by the LJ potential, which shows the LJ potential minimum moving to longer separations ( $r_{LJmin}$ ) with increasing fragment size, see table 2.3. However the opposite trend appears to be predicted by the roaming TS of Harding *et al.*, and whatever direction  $r_{roam}$  does change in, the magnitude of the change indicated by our simple Morse approximation is too large.

We speculate that a PES approximation may be useful for estimating the roaming threshold, and thus  $\Delta E_{roam}$ , for molecules for which there is no experimental data. The roaming threshold bondlength ( $r_{roam}$ ), however, will depend on the van der Waals interactions between the dissociating fragments, which is not modelled in a Morse potential. A more accurate description of  $r_{roam}$  would require additional information about this region of the PES.

## F.2 Centrifugal Barriers

Eventually, in addition to modelling low  $\vec{J}_{parent}$  photodissociation experiments, we intend to apply this model to pyrolysis, requiring averaging over a large  $\vec{J}_{parent}$  range. High  $\vec{J}_{parent}$  will require an additional restriction on  $\vec{L}$  such that all counted states possess at least the minimum translational energy ( $E_t$ ) along the reaction coordinate, required to escape the centrifugal barrier imposed by  $\vec{L}$ . The energy due to  $\vec{L}$  is given by

$$E_{orb}(r) = \frac{\vec{L}(\vec{L} + 1)\hbar^2}{2\mu r^2} \quad (\text{F.4})$$

where  $\mu$  is the reduced mass of the orbiting fragments, orbiting at centre of mass separation  $r$ .  $E_{orb}$  decreases monotonically with  $r$ . At the large values of  $r$  implicated in roaming  $E_{orb}$  is expected to be small. The effective potential due to  $E_{orb}$  is given by

$$V_{eff}(r) = V(r) + E_{orb}(r) \quad (\text{F.5})$$

At high  $\vec{L}$ , a centrifugal barrier arises at  $V_{eff}(r^*)$ , where  $r^*$  is the bond length where the effective potential is maximum, illustrated in figure F.1. In figure F.1, the minimum separation at which roaming may occur ( $r_{roam}$ ) is greater than  $r^*$ , which is an assumption that requires further investigation ( $r^*$  gets smaller as  $\vec{L}$  increases, so if  $\vec{L}$  is low  $r_{roam} < r^*$ ). A centrifugal barrier impedes roaming when  $r_{roam} > r^*$ . In this case,  $V_{eff}(r^*) > V(r^*)$  and  $V_{eff}(r_{roam}) \approx V(r_{roam})$ . Energy is conserved, so the  $E_{orb}$  lost between  $r^*$  and  $r_{roam}$  is transferred to  $E_t$ . Therefore states are only valid at  $r_{roam}$ , if  $E_t$  is large enough to account for this energy transfer. That is  $E_t \geq E_{tmin}$  where  $E_{tmin} = V_{eff}(r^*) - V_{eff}(r_{roam})$  is the minimum translational energy required for a state to have escaped the centrifugal barrier, see figure F.1.

An analytic implementation of this  $\vec{L}$  restriction that uses the Lennard-Jones potential is given by

$$\vec{L}(\vec{L} + 1)\hbar^2 \leq 6\mu C_6^{1/3} (E_{tot}/2)^{2/3} \quad (\text{F.6})$$

where the constant  $C_6$  is the spherically averaged sum of dipole-induced-dipole and dispersion contributions [48, 49]. However, simply setting a maximum allowable value for  $\vec{L}$  ( $\vec{L}_{max}$ ) will

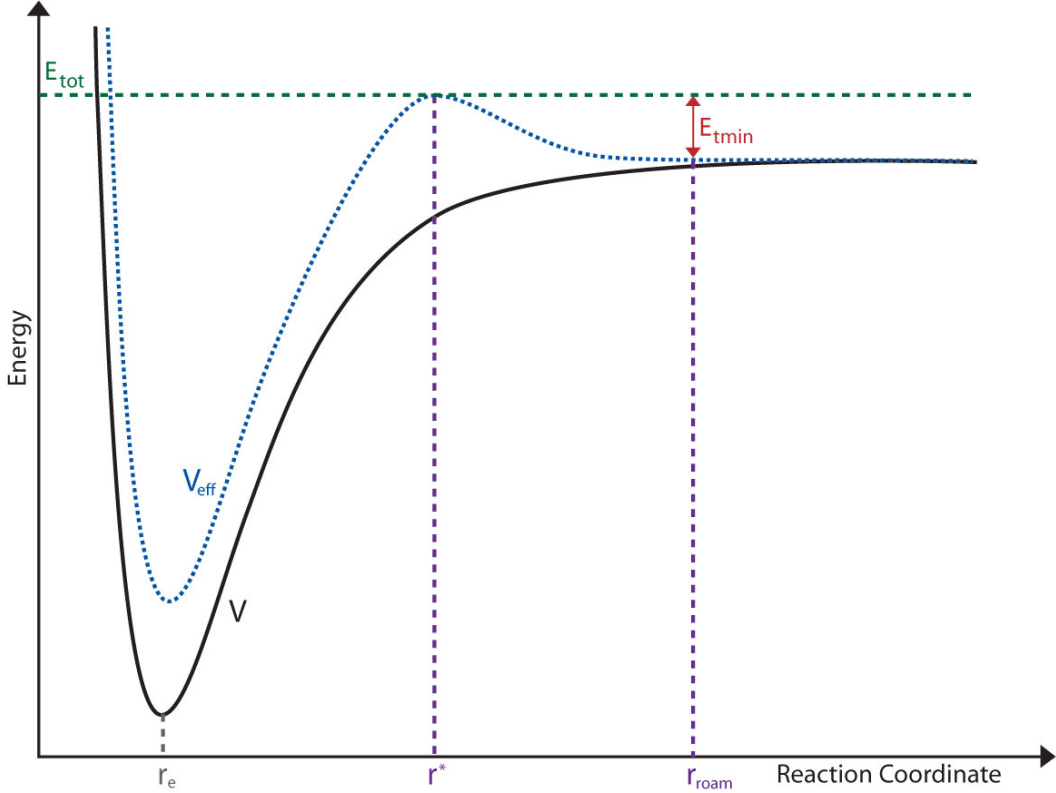


FIGURE F.1: At high  $\vec{L}$ , a centrifugal barrier arises at  $V_{eff}(r^*)$ , where  $r^*$  is the bond length where the effective potential is maximum. Therefore states are only valid at  $r_{roam}$ , if  $E_t$  is large enough to account for this energy transfer. That is  $E_t \geq E_{tmin}$  where  $E_{tmin} = V_{eff}(r^*) - V_{eff}(r_{roam})$ .

allow states with  $\vec{L} = \vec{L}_{max}$  and  $E_t < E_{tmin}$ . Such states can only exist if the system is ergodic at  $r_{roam}$ . Our picture of roaming as due to frustrated radical dissociation relies on the loss of ergodicity at  $r_{roam}$ . We therefore explicitly treat centrifugal barriers in terms of  $E_t$  by requiring

$$E_t \geq V_{eff}(r^*) - V_{eff}(r_{roam}) \quad (F.7)$$

This implicitly constrains  $\vec{L} \leq \vec{L}_{max}$  due to the conservation of energy constraint, requiring  $E_{tmin} \leq E_t < E_A$ . Our intention is to use a Morse approximation of the PES, described below, to model the long range interactions involved. In this case,  $r^*$  must be obtained numerically at runtime.

## F.3 Collisions And Pressure Dependence

Pyrolysis modelling will also require consideration of collisions and the affect pressure has on the roaming channel. When considering pressure dependence, collisions and energy transfer probabilities must be taken into account...

## F.4 Rotational Switching

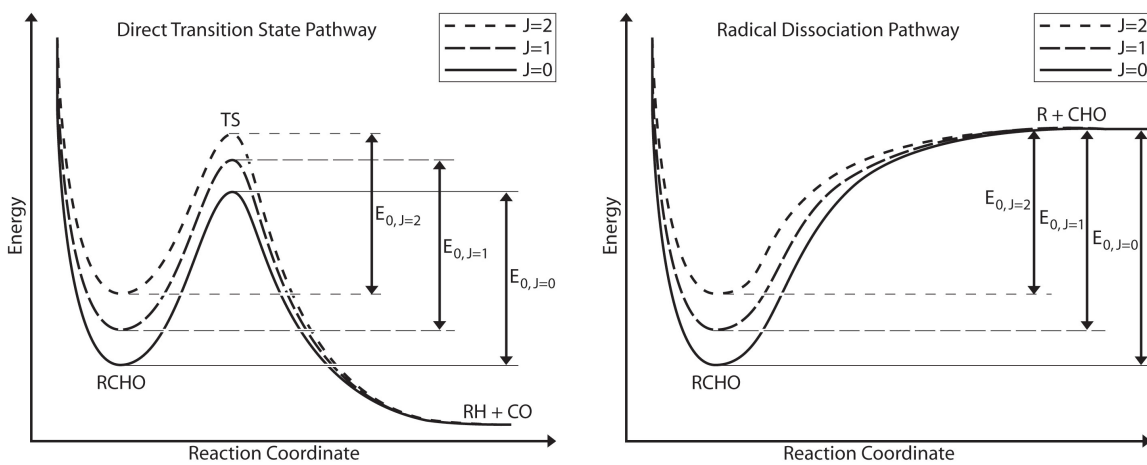


FIGURE F.2: Potential energy diagrams illustrating the effect of  $J$  on the energy barrier to molecular products via a classic TS (left), and to radical dissociation (right). Note that for the direct TS channel the energy of both reactants and the TS are raised at higher  $J$ , while for dissociation to radical products the absence of an energy barrier results in higher  $J$  reactants requiring less additional energy to dissociate. This effect can lead to rotational switching, where at low  $J$  the classic TS channel (1) is favoured while at high  $J$  the radical channel (2) is favoured.

When considering non-zero  $J$ , care must be taken to consider rotational switching. Rotational switching arises because channel (1) has an energy barrier, while channel (2) has no energy barrier. Using the rigid rotor approximation, rotational energy is given by,

$$E_{rot} = BJ(J + 1) \quad (\text{F.8})$$

where  $B$  is the rotational constant. As the dissociation products separate, the moment of inertia ( $I$ ) becomes very large and hence the rotational constant, which is inversely proportional to  $I$ , approaches 0. Because  $J$  is conserved,  $E$  of reactants is therefore raised by  $E_{rot}$  relative

to  $E$  of dissociated products. However for channel (1),  $E_{rot}$  of the “tight” transition state is also raised at high  $J$ , because  $I$  remains small. Therefore at high  $J$  values,  $k_2$  increases while  $k_1$  is relatively unaffected. One approximation is by using the threshold energy of the more favourable channel as  $E_0$  [43].

## APPENDIX G

### Experimental Evidence For Roaming

---

The majority of experimental research into roaming mechanisms is done in conjunction with theoretical modelling. Theoretical modelling is required to both aid the analysis of experimental results and validate any conclusions drawn. Most of the experimental studies discussed in the experimental section of this review are accompanied by quasiclassical trajectory (QCT) calculations on *ab initio* potential energy surfaces (PES). However, for the sake of clarity, the theoretical calculations and experiments will be described separately.

### G.1 Evidence for roaming in photolysis experiments

The hypothesis that two dynamically distinct pathways to molecular products ( $\text{H}_2$  and CO) exist for the dissociation of formaldehyde ( $\text{H}_2\text{CO}$ ), was based on the observation of bimodal CO quantum state distributions. In 1993 the Moore group first observed bimodal populations with high and low angular momentum CO fragments ( $\vec{J}_{\text{CO}}$ ), in laser-induced fluorescence (LIF) experiments on  $\text{H}_2\text{CO}$  [117]. The photolysis energy was tuned to the strongest absorbing regions of the  $2^14^1$  and  $2^34^1$  bands ( $29495 \text{ cm}^{-1}$  and  $31803 \text{ cm}^{-1}$  respectively). The high  $\vec{J}_{\text{CO}}$  fragments could be rationalised as products of an impulsive reaction over a tight TS [117]. However rationalising the low  $\vec{J}_{\text{CO}}$  fragments was problematic without data on the quantum state of the corresponding  $\text{H}_2$  fragments.

Impulsive models apply to reactions where products are formed while falling down a steep potential energy hill, from a tight TS. Impulsive models make “the impulse assumption”, that the

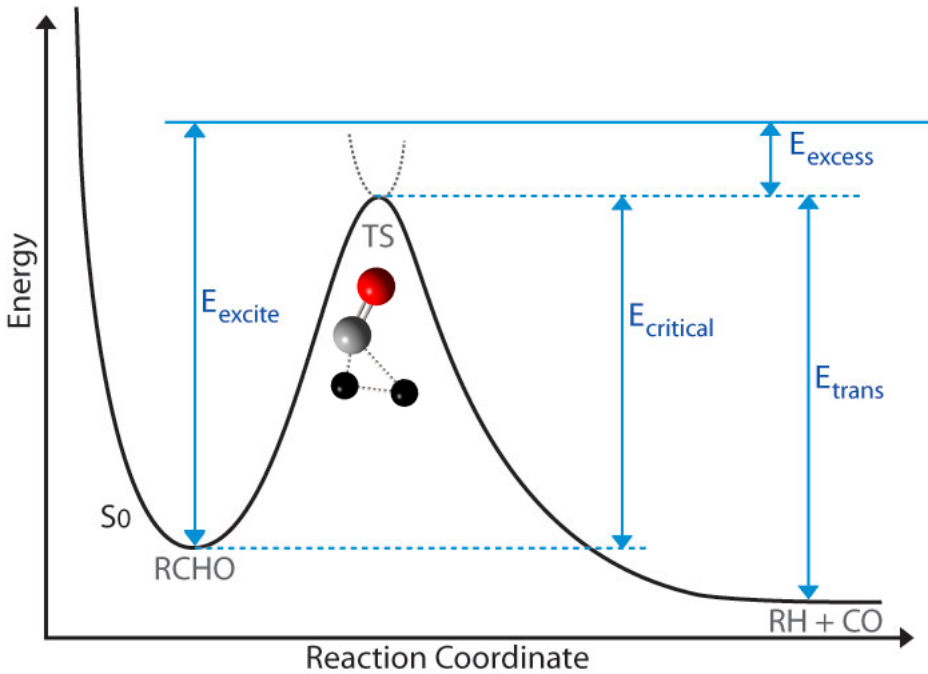


FIGURE G.1: Potential energy diagram for an impulsive reaction, where  $E_{\text{excess}}$  is the energy that will be distributed statistically and  $E_t$  is the energy that must become relative translational energy.

sudden release of the reaction exoergicity manifests itself as an impulse  $I_{TS}$  ( $\text{N.s}$  or  $\text{kg.m.s}^{-1}$ ),

$$I_{TS} = \sqrt{2\mu_{TS}\Delta E_{TS}} \quad (\text{G.1})$$

where  $\mu_{TS}$  is the effective mass of the TS and  $\Delta E_{TS}$  is the reaction exoergicity released [26]. Impulsive reactions are characterised by high relative translational energies of the separating fragments, with the fragments having relatively low vibrational energies [24]. Short-range forces act between the fragments as they dissociate, thus dissociation occurs suddenly, on a time-scale short with respect to bending motions [25]. The products separate so rapidly that the energy released during dissociation is converted to kinetic and internal energies of the fragments, before the fragments have moved away from their tight TS configuration, see figure G.1 [25]. The fragment rotation produced in the impulsive limit is obtained by requiring angular momentum and energy be conserved and fragment kinetic energies be imparted entirely while the fragments are in the TS configuration [25]. The skewed H<sub>2</sub>CO TS leads to high  $\vec{J}_{CO}$  because the impulse vector does not point along the C=O bond, producing a torque.

In order to prove that a mechanism other than the well known tight TS channel, (1), causes the second  $\vec{J}_{CO}$  population observed by the Moore group, information on the quantum state of the corresponding H<sub>2</sub> fragments is required. If it can be shown that the H<sub>2</sub> corresponding to low  $\vec{J}_{CO}$  fragments have high internal energy, then an impulsive model cannot explain their existence. Therefore by a process of elimination, such an observation is strong evidence that the low  $\vec{J}_{CO}$  fragments are the product of a different, non-impulsive type of mechanism. Such a mechanism was proposed by van Zee *et al.* to explain their results [117].

Proving the second  $\vec{J}_{CO}$  population is produced via a mechanism other than the well known tight TS channel, (1), requires information about the quantum state of the corresponding H<sub>2</sub> fragments [118]. Unless Doppler broadening in each individual  $\vec{J}_{CO}$  peak can be observed, LIF can only reveal that a bimodal  $\vec{J}_{CO}$  distribution exists, without simultaneously revealing the relative translational energy of the H<sub>2</sub> and CO fragments.

A new experimental technique, called DC slice imaging, was utilised by Suits *et al.* in 2004 to determine recoil velocity distributions corresponding to specific values of  $\vec{J}_{CO}$  in formaldehyde dissociation [14]. Because the total energy is fixed by the laser, and energy is conserved, the internal energy of the H<sub>2</sub> fragment can be inferred from the CO recoil velocity. For high angular momentum,  $\vec{J}_{CO} = 40$ , a high recoil velocity was observed for the CO fragments, corresponding to cold H<sub>2</sub> (peak  $v_{H_2} = 2$ ). This was consistent with the tight TS channel, reaction (1). For an intermediate value,  $\vec{J}_{CO} = 28$ , a bimodal recoil velocity was observed, indicating that both hot (peak  $v_{H_2} = 7$ ) and cold (peak  $v_{H_2} = 2$ ) H<sub>2</sub> were formed. Finally a low value,  $\vec{J}_{CO} = 15$ , produced only low velocity CO, corresponding to the production of hot H<sub>2</sub> (peak  $v_{H_2} = 7$ ). The presence of hot H<sub>2</sub> was strong evidence for a different mechanism. Suits *et al.* proposed the roaming mechanism, reaction (3), which was supported by concurrent QCT calculations, as described below [14]. In concluding, Suits *et al.* posed two questions; can polyatomic products be formed by roaming, and can an atom other than H be the abstraction target.

In 2006 Suits *et al.* measured an 18 % roaming contribution to molecular products for H<sub>2</sub>CO photodissociation from the 2<sup>1</sup>4<sup>3</sup> band (30340 cm<sup>-1</sup>) [46]. Isotropic angular distributions in

the DC slice images of formaldehyde indicated that the lifetime to dissociation was significantly longer than one molecular rotational period [15]. Photofragment excitation spectroscopy (PHOFEX) was used to estimate the photolysis energy dependence of the roaming channel, showing roaming occurred well above the radical energy threshold [15].

In 2007 the energy dependence of the roaming fraction in formaldehyde photodissociation was calculated using PHOFEX data in the range ( $30150 - 32000 \text{ cm}^{-1}$ ) [27]. These results showed that as energy increases over this range, the branching fraction to channel (1) decreases from 0.82 to 0.15, channel (2) increases from 0.0 to 0.75, and channel (3) decreases from 0.18 to 0.10 [27].

In 2008 formaldehyde photolysis in the range ( $30000 - 35400 \text{ cm}^{-1}$ ) was carried out and DC slice images and PHOFEX spectra were obtained. The roaming threshold was found to be between the  $4^5$  band ( $30123 \text{ cm}^{-1}$ ) and the  $2^16^1$  band ( $30241 \text{ cm}^{-1}$ ), which is approximately  $100 \text{ cm}^{-1}$  below the  $S_0$  two-body radical threshold (2) ( $30327.6 \text{ cm}^{-1}$ ) [6]. Roaming was also observed at energies up to the threshold of three-body dissociation ?? ( $35217 \text{ cm}^{-1}$ ), which is above the threshold for radical dissociation on the triplet surface ( $\approx 32000 \text{ cm}^{-1}$ ), channel ???. At the highest energies studied more than half the molecular products were formed by roaming [5]. However, as excitation energy increases, channel ?? becomes dominant [6]. Nuclear spin was observed to be largely conserved during roaming [6]. Figure G.2 summarises these observations.

Roaming observations were made for  $\text{D}_2\text{CO}$  photodissociation via DC slice imaging experiments by Suits *et al.* in 2009 [59]. The energy partitioning in the  $\text{D}_2$  and CO products was similar to that observed in the  $\text{H}_2\text{CO}$  roaming experiments. Indeed the  $\text{D}_2\text{CO}$  experiments were purposefully conducted at excitation energies giving the closest matching energy excess above the radical threshold for both  $\text{D}_2\text{CO}$  and  $\text{H}_2\text{CO}$  [59]. The vibrational frequency of  $\text{H}_2$  is  $\approx 1.4$  times that of  $\text{D}_2$ . This produced an expected shift to higher vibrational quanta in the  $\text{D}_2$  fragments with respect to  $\text{H}_2$  when measured at the same  $\vec{J}_{\text{CO}}$ . The total internal energy of the  $\text{D}_2$  and  $\text{H}_2$  were the same. Background interference problems reduced the accuracy of the  $\text{D}_2\text{CO}$  roaming fraction estimate. However the minimum of 15% branching for  $\text{D}_2\text{CO}$  from the  $2^24^3$  band was similar to the 18% branching for  $\text{H}_2\text{CO}$  from the  $2^14^3$  band [46, 59]

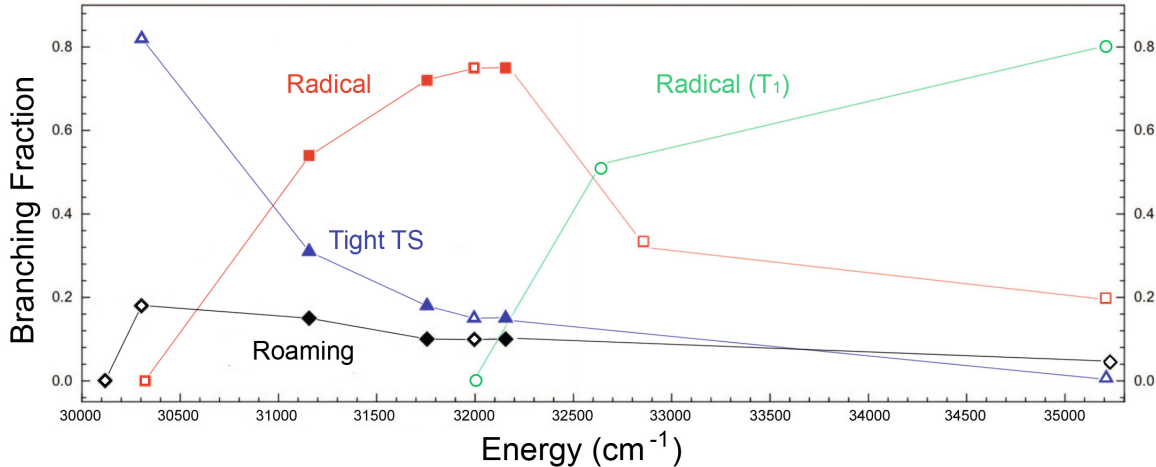


FIGURE G.2: Experimental branching fractions for formaldehyde ( $E_{tot} = 30000 - 32500 \text{ cm}^{-1}$ ). Adapted from Figure 8 in Ref [5], with points added to reflect observations in [6]. Solid points from original figure, hollow points from [6].

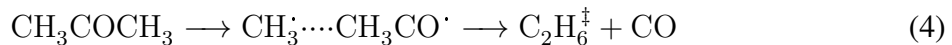
Roaming was first observed in acetaldehyde ( $\text{CH}_3\text{CHO}$ ) in the LIF experiments of Houston and Kable (HK) in 2006 [8]. Similarly to  $\text{H}_2\text{CO}$ , bimodal  $\vec{J}_{\text{CO}}$  populations were detected, where the high  $\vec{J}_{\text{CO}}$  distribution corresponded to channel (1) products and the low  $\vec{J}_{\text{CO}}$  distribution was assigned to roaming products. Doppler broadening indicated that high  $\vec{J}_{\text{CO}}$  fragments had more translational energy than low  $\vec{J}_{\text{CO}}$  fragments, suggesting that hot  $\text{CH}_4$  fragments corresponded to the low  $\vec{J}_{\text{CO}}$  fragments. HK compared Doppler profiles of low  $\vec{J}_{\text{CO}}$ , measured with the probe laser polarization aligned both horizontally and vertically, observing no difference. This meant there was no significant anisotropy in the reaction, indicating that the time scale of the roaming reaction was longer than the rotational period of the molecule [8]. HK hypothesised that the roaming fragment was likely methyl; the  $\text{CH}_3 + \text{CHO}$  dissociation pathway is lower in energy than the  $\text{CH}_3\text{CO} + \text{H}$  pathway and the methyl and formyl groups can both tie up excess energy increasing the odds of dissociation frustration. Moreover, the planar  $sp^2$  hybridized methyl radical would readily abstract the exposed H-atom [8]. This evidence answered Suits' first question by confirming that a polyatomic product can be formed by a roaming mechanism [14].

Heazlewood *et al.* (2008) used time-resolved Fourier transform infrared (FTIR) emission spectroscopy to probe the vibrational states of  $\text{CH}_4$  fragment products of  $\text{CH}_3\text{CHO}$  photodissociation [4]. They observed broad emission in the C–H stretch region ( $2400 - 3100 \text{ cm}^{-1}$ ),

indicating highly vibrationally excited CH<sub>4</sub>, with an average of 75% of the available energy distributed into CH<sub>4</sub> vibration, with a sharp peak in the distribution at  $\approx 95\%$  [4]. These results, interpreted using QCT calculations, showed that a CH<sub>3</sub> roaming mechanism, (3), is the dominant channel to molecular products ( $84 \pm 10\%$  of total flux) for CH<sub>3</sub>CHO photodissociation, and that roaming fragments are not limited to H atoms [4]. Heazlewood *et al.* use entropic arguments (larger A factor) to conclude that the dominance of the roaming channel is related to the almost isoenergetic radical asymptote and tight TS barrier, predicting roaming channels in other systems with close threshold energies to radical and molecular products [4].

\*\*DCO stuff may go here\*\*\*

DC slice imaging experiments of Suits *et al.* in 2008 have also shown evidence for roaming in acetone photodissociation, however this evidence was not as clear cut [17]. This observation was analogous to the H<sub>2</sub>CO and CH<sub>3</sub>CHO roaming observations, in that a bimodal  $\vec{J}_{CO}$  distribution was observed, where high  $\vec{J}_{CO}$  corresponded to the well known tight TS channel and low  $\vec{J}_{CO}$  fragments indicated the presence of roaming [8, 14]. Suits *et al.* estimated the roaming fraction to be  $\approx 15\%$ . Like acetaldehyde, methyl was expected to be the roaming fragment. However unlike acetaldehyde, rather than abstracting H, the roaming fragment abstracted an entire methyl fragment,



Confirmation of this would answer Suits' second question: can atoms other than H, and in fact polyatomic fragments, can be the abstraction target in a roaming mechanism [14].

## G.2 Evidence for roaming in pyrolysis experiments

There is a wealth of experimental data on formaldehyde, acetaldehyde and acetone pyrolysis in general [?, ?, ?, 119, 120]. To date, no evidence has been found for roaming in formaldehyde pyrolysis. Saxena *et al.* looked, unsuccessfully, for evidence of roaming in acetone pyrolysis in 2009 [121]. However, Michael *et al.* observed evidence for roaming in acetaldehyde pyrolysis in 2010, using the reflected shock tube technique with H(D)-atom atomic resonance absorption

spectroscopy (ARAS) detection [30]. They estimated the roaming fraction of the total thermal dissociation as  $0.23 \pm 0.09$  in the temperature range 1346 – 1888 K, at a few hundred Torr [30]. Little temperature and/or pressure dependence of this branching ratio was observed under these conditions [30].

## APPENDIX H

### Quasiclassical Trajectory Calculations Of The Bowman Group

---

In 2004 Bowman *et al.* ran quasiclassical trajectory (QCT) calculations on an *ab initio* ground state potential energy surface (PES) of formaldehyde. Their simulation yielded bimodal  $\bar{J}_{CO}$  and  $v_{H_2}$  distributions, in good agreement with the experimental distributions [14, 46]. The experiments and QCT calculations established roaming as a credible reaction path [14, 46]. Bowman *et al.* used a similar approach to create a full-dimensional ground state potential energy surface for acetaldehyde in 2007 [29]. The QCT calculations, from the equilibrium geometry of acetaldehyde, were also in good agreement with the acetaldehyde roaming observations of Houston and Kable (HK) [8]. Furthermore, QCT calculations from the tight acetaldehyde TS did not agree with HK's experimental results, further supporting their roaming hypothesis.

The generation of such PES requires large amounts of computation. In developing these PES, Bowman et al had to first calculate  $\approx 80000$  and  $\approx 135000$  ab initio energy points for formaldehyde and acetaldehyde respectively [28, 29]. Choosing the level of theory and the appropriate basis sets for these calculations is problematic because regions where bonds are breaking are harder to model. There are several reasons for this, all related to the breaking bond becoming very long.

Long bonds require a very large basis set and this greatly increases the number of possible orbital combinations, increasing computational requirements. Without additional diffuse functions in the basis set, the energy of the breaking bond orbital will be overestimated because the electrons in that orbital will not be allowed to separate as far as possible and dynamic electron correlation will not work effectively. Finally, as the two fragments move further apart toward radical products, the energies of a number of the possible electronic states of the molecule converge towards the ground state energy of the dissociation products. This means calculations

in these regions of space require multiple determinants, one for each electronic state. [34, 118] This multi-determinant character of the wavefunction is often termed static electron correlation.

In other regions of the surface single reference (single determinant) methods will work well. [34, 118] This means a high level of theory can be used, without requiring static electron correlation or having to deal with multiple determinants. Therefore a very large amount of computation can be avoided and higher accuracy can be obtained in the single reference regions. For formaldehyde, Bowman *et al* calculated ab initio energies using the aug-cc-pVTZ basis set, a medium basis set (for this system) with diffuse functions. They used the coupled cluster singles and doubles method with a perturbative treatment of triple excitations (CCSD(T)) where single reference methods work well ( $\text{H}_2\text{CO}$ ,  $\text{HCOH}$  and  $\text{H}_2 + \text{CO}$ ), and a multireference configuration interaction (MR-CI) approach in the inherently multi-reference regions of the radical channels ( $\text{H} + \text{HCO}$  and  $\text{H} + \text{H} + \text{CO}$ ) [28].

Once the energy points have been calculated and scaled they need to be converted into a functional form, so that trajectories can be calculated on them. Unfortunately, there is no functional form for systems with four or more atoms, so an approximation has to be made. In producing their functional form, Bowman *et al*. do local fits to symmetry invariant polynomial expansions in Morse coordinates, using a multidimensional linear regression. A consequence of using high order polynomials to fit ab initio data points is the potential for introducing non-physical “wiggles” into the surface. [118] Additionally, for any of the methods described above, there may be significant error between the ab initio values and the resultant functional form.

Using different ab initio levels of theory and/or basis sets in different regions produces another problem, joining those regions. This difficult process inevitably requires scaling and smoothing to make the energies match where regions overlap, which in practice introduces non-physical “wiggles” into the PES, contributing uncertainty. For the formaldehyde PES, six regions were least squares fit and joined smoothly by five switching functions [28, 42].

For acetaldehyde, ab initio energies were computed by CCSD(T) using the correlation consistent cc-pVDZ, cc-pVTZ and aug-cc-pVTZ basis sets. It has been shown that the CCSD(T) method properly describes dissociation via channel (1) but not via channel (2) [29, 122]. Rather

than use the MR-CI approach for the multireference regions on the acetaldehyde radical channel, Bowman et al did CCSD(T) calculations for the noninteracting radical fragments and let their fit fill in the gaps. MR-CI calculations were then used to check the validity of the resulting functional form [29].

Once the PES has been generated, classical trajectories are run by solving Newton's equations of motion over very short time steps. There are a variety of ways to achieve this, the simplest considering only the first derivative of the current point on the PES. The size of the time steps is important because the PES is not linear. This non-linearity implies an inherent error in calculating where in phase space the molecule ends up based only on the derivative at the current point and Newton's equations. Smaller steps are therefore preferable, especially in regions where the PES is steep. This error accumulates over time, and roaming trajectories can be very long (several picoseconds) [36, 37, 118]. This is one of several sources of uncertainty with QCT.

Uncertainty also arises because approximations must be made when selecting initial quantum conditions for the trajectories. [35] The photodissociation of formaldehyde and acetaldehyde begins with internal conversion from  $S_1$  to  $S_0$ , so the distribution of vibrational energy as the molecules enter the  $S_0$  PES may be influenced by the nature of conical intersection between  $S_1$  and  $S_0$ . However statistical approaches are typically used. An accurate approach would be microcanonical sampling using a Markov walk (weighted Monte Carlo sampling) in phase space to find the most likely energy distributions. A simpler, less accurate method, used by Bowman et al, is to randomly distribute energy into harmonic normal modes, without considering the relative energies of each mode. [36] The initial distribution of energy effects the trajectory over the surface and therefore an inaccurate or unrealistic distribution may bias results. [9, 35, 37] Furthermore, this approach requires Bowman et al project to the  $\vec{J} = 0$  state [28]. The same technique is used to project specific  $\vec{J}$  values in later analyses where non-zero  $\vec{J}$  is considered [42].

The uncertainty related to the treatment of zero point energy (ZPE), is perhaps the biggest problem in QCT simulations. This is a general problem in comparing quantum and classical dynamics and, although a number of solutions have been proposed, there is no accepted way to

account for ZPE in classical simulations [38–40]. Bowman *et al.* put ZPE into each classical vibrational mode, but ZPE is a quantum property and does not occur in classical mechanics. In classical mechanics this ZPE can leak out, giving the molecule more energy in the reaction coordinate than should exist quantum mechanically for the given excitation energy [40, 41]. This can lead to unphysically large flux across the TS surface. This is particularly problematic for modelling CH<sub>3</sub>CHO dissociation, because when ZPE is included, the three-body radical dissociation channel ?? is open, whereas it is closed if ZPE constraints are included. Because there are 3 fragments, this channel has enormous entropy and therefore high probability. These trajectories are discarded by Bowman *et al.*, as are any trajectories where the products have less energy than the ZPE [42]. This, again, introduces a potential source of bias in interpreting results.

Despite all the sources of uncertainty and bias in the QCT approach, the results of these calculations agreed very well with the experimental observations. This indicates that, even with all the approximations and assumptions involved, QCT does a good job modelling the dynamics of formaldehyde and acetaldehyde photodissociation. In fact, QCT generally performs well despite these issues. [35, 37, 41]